RSC Advances

ROYAL SOCIETY OF CHEMISTRY

REVIEW

View Article Online
View Journal | View Issue

Check for updates

Cite this: *RSC Adv.*, 2025, **15**, 50270

# Zinc selenide engineered nanostructures: insights into modification strategies, and multifunctional applications in environmental remediation, gas sensing, energy storage, and antimicrobial activity

Ruhit Kumar Paul, Saptarshi Roy and Md Ahmaruzzaman *

Received 9th October 2025
Accepted 28th November 2025

DOI: 10.1039/d5ra07718d

rsc.li/rsc-advances

Zinc selenide (ZnSe), an outstanding and admirable photocatalytic material from the II–VI group, exhibits a direct energy band gap of 2.67 eV. This rising contender has sparked considerable attention owing to its distinctive physicochemical characteristics and extensive multifunctional potential. This article commences with a comprehensive and systematic exploration of the intrinsic novel attributes of ZnSe nanostructures, encompassing their structural, optical, and electronic novelties. It further summarizes the various fabrication methodologies which have been instrumental in tailoring parameters like particle size, morphology, and crystallinity to optimize functional performance across a breadth of applications. Key modification strategies, including elemental doping and heterojunction engineering, are highlighted to underscore their indispensable roles in mitigating the recombination rate while enhancing the efficiency of photoinduced charge carrier separation and migration. The discourse progresses to delineate the evolution from conventional composite architectures to advanced Z-scheme configurations, offering profound insights into their revolutionary implications. Additionally, essential characterization techniques are surveyed, elucidating the intricate correlations between structural, morphological, optical, and electronic properties and their resultant influence on functional efficacy. Furthermore, the study spotlights the recent advancements in multifaceted applications in utilizing ZnSe-based composites as potential tools for environmental applications, including the removal of hazardous heavy metals, pharmaceuticals, phenolic compounds, and other persistent organic contaminants, as well as their role in $CO_2$ mitigation, Cr(VI) remediation, gas sensing, advanced electrode materials in lithium-ion (LIBs), sodium-ion (SIBs), and potassium-ion batteries (PIBs), alongside antimicrobial activities. Mechanistic insights into these remediation pathways are thoroughly outlined. Subsequently, the article sketches the inherent challenges and delineates future research developments and potential avenues for material optimization, which is anticipated to facilitate further exploration and innovation in this dynamic field in the days to come.

## 1. Introduction

Over the past few decades, semiconductor photocatalysts have become a central point within the field of photochemistry due to their exceptional catalytic performance and vast potential in addressing complex environmental challenges.[1] Wastewater from industrial processes contain a diverse array of hazardous organic and inorganic contaminants, significantly compromising the quality of water.[2] The majority of wastewater pollutants are substances with a high resistance to biological breakdown, such as pharmaceuticals, heavy metals, dyes, cosmetics, and pesticides.[3–5] A number of physicochemical procedures, such as adsorption, microfiltration, ultrafiltration, reverse osmosis, and advanced oxidation processes, have been proposed as means of wastewater purification.[6] One such method that has recently come up as an eco-friendly solution to the issue of wastewater treatment is the advanced oxidation process.[7,8] Over the past few years, nanostructured semiconductors have been the topic of meticulous research, not only to gain a better understanding of their underlying properties, but also to create practical applications in electrical and optoelectronic devices.[9] Additionally, their photocatalytic capabilities hold enormous promise, especially for solar fuel generation and environmental pollution control.[10,11] The photocatalytic process, employing semiconductors as photocatalysts, is designed to generate reactive species responsible for the breakdown of organic pollutants into non-hazardous by-products. At its core, photocatalysis entails the excitation of electron–hole pairs upon appropriate light irradiation. These

---

*Department of Chemistry, National Institute of Technology Silchar, 788010, Assam, India. E-mail: mda2002@gmail.com*

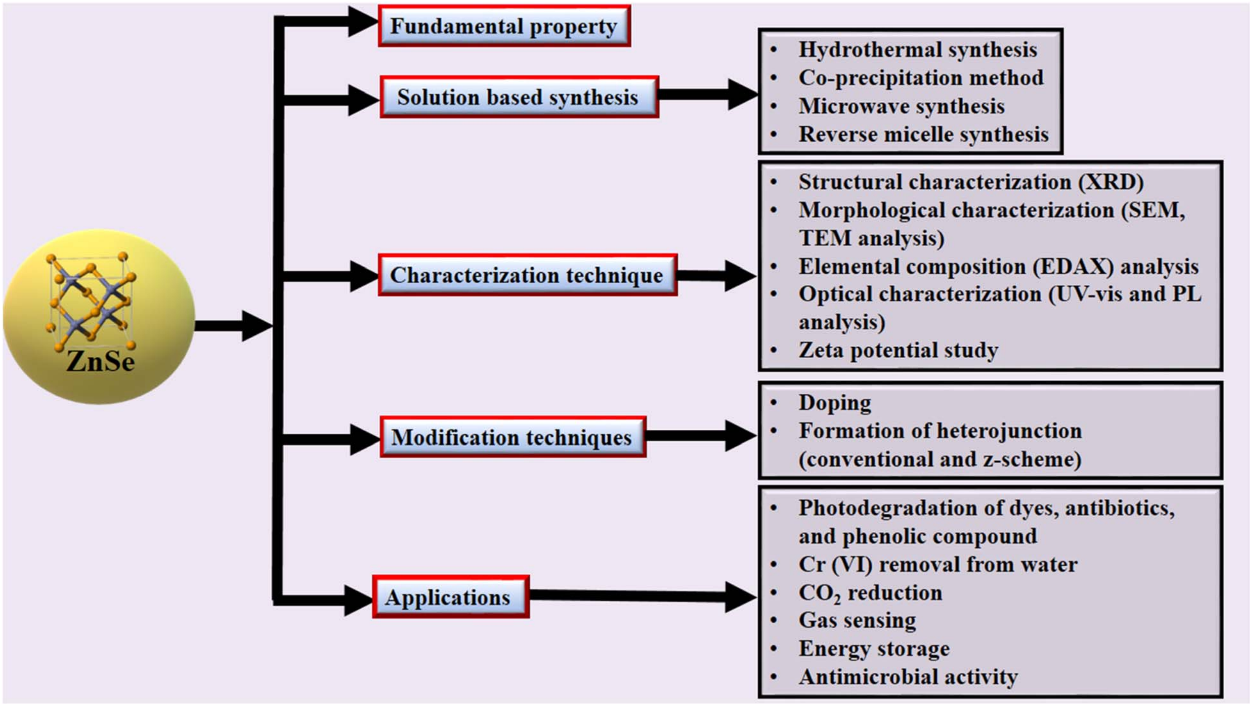

Fig. 1 Overview and summary of the review (self-produced).

charge carriers subsequently move toward the semiconductor surface, driving redox reactions critical for the origination of reactive oxygen species (ROS), such as $^{\bullet}OH$, $^{\bullet}O_2$, and $^{\bullet}OOH$, which play a pivotal role in the pollutant breakdown process into simpler molecules such as $CO_2$ and $H_2O$.[9,12]

Numerous semiconductors and earth-abundant photocatalysts have been reported over the years. However, limitations, including a wide bandgap (3.2 eV), absorption of ultraviolet light, and weak photocatalytic response in visible light, reduce their effectiveness.[13,14] It has been reported that the high band gap of nanoscale $TiO_2$ (3.2 eV) and ZnO (3.37 eV) powder allows them to absorb light in the ultraviolet region, which accounts for 3–5% of the total electromagnetic spectrum.[15–17] Nevertheless, because of their high rate of electron–hole recombination and low doping content, their visible-light catalytic efficiency is relatively poor. Recently, catalysts based on $Ag_3PO_4$,[18,19] $BiVO_4$,[20,21] and semiconductor heterostructures have been developed for the visible-light degradation of organic contaminants with exceptional photocatalytic efficacy.[22] Unfortunately, their substantial cost and possible heavy metal contamination still hinder their practical usage in field applications. Graphitic carbon nitride (g-$C_3N_4$), a metal-free material, has recently garnered much attention in the realm of visible-light photocatalysis.[23,24] However, to boost its catalytic performance, it is still necessary to couple it with other photoactive materials. Thus, it is imperative to create novel visible-light photocatalysts of the aforementioned properties to address the growing demand for environmental remediation.

Recently ZnSe has gained significant attraction due to its tunable optical and electronic behavior, chemical stability and potential for recyclability.[25–28] Additionally, it absorb light in the visible-light region, making them a promising visible-light photocatalyst.[29] Zinc selenide, featuring a direct band gap of 2.70 eV (460 nm) at room temperature, stands as a pivotal II–VI semiconductor, opening the door to advancements in short-wavelength photoelectronics, including cutting-edge photodetectors,[30,31] biomedical sensors,[32] blue laser diodes,[33] LEDs,[34] solar cells,[28] and photocatalysts.[29,35] Additionally, it can also serve as electrodes in lithium ion batteries,[36] sodium ion batteries,[37] potassium ion batteries,[38] and toxic gas sensors.[39]

ZnSe nanocage structures have demonstrated strong interaction energies with $CO_2$ molecules, making them suitable candidates for the development of sensitive gas sensors capable of detecting hazardous gases such as $CO_2$ and $SO_2$.[40] While a wide range of materials have been investigated for $CO_2$ photoreduction,[41–43] zinc chalcogenides, especially ZnSe stand out due to their suitable bandgap and strong visible-light absorption, which enable efficient charge generation and utilization.[44] Also, ZnSe is considered a very promising anode material because of its strong electrochemical activity and reliable performance across different energy storage systems.[45] It is also chemically stable, non-hygroscopic, remains highly pure, and has a dense structure, which further contribute to its ease of processing and applicability.[46] In LIBs, ZnSe undergoes a conversion process where reduced Zn reacts with $Li^+$ to form LiZn, supplying additional capacity to the battery.[45] Additionally, bacterial infections represent a significant and growing threat to human health, compelling researchers to explore cutting-edge strategies and materials to address diseases caused by pathogenic strains, antibiotic resistance, and genetic mutations. The formation of bacterial biofilms further complicates this issue, leading to critical implications in both medical and industrial sectors. Selenide materials, with their ability to release ions at the surface, exhibit potent antibacterial properties by inducing cell wall disruption, making them a promising candidate for mitigating these challenges.[47,48]

This review article offers a detailed and systematic exploration of the recent advancements, spotlighting the distinctive structural, optical, and electronic attributes of ZnSe nanostructures. It summarizes the fabrication methodologies that have been instrumental in precisely tailoring critical parameters-such as particle size, morphology, and crystallinity, to optimize performance across diverse functional domains. The discussion accentuates pivotal modification strategies, notably elemental doping and heterojunction engineering, which are indispensable for suppressing charge carrier recombination and enhancing the efficiency of photoinduced charge separation and migration. Furthermore, the article surveys essential characterization techniques, elucidating the intricate correlations between structural, morphological, optical, and electronic properties and their influence on functional efficacy. Despite the escalating interest in photocatalytic materials, there remains a noticeable paucity of comprehensive studies dedicated specifically to ZnSe photocatalysts, as evidenced by Scopus analyses and earlier reports.[44,49] Addressing this critical gap, the review assembles the compelling advantages of ZnSe across a spectrum of multifaceted applications, encompassing not only the degradation of textile dyes but also the comparatively underexplored breakdown of antibiotics and phenolic contaminants, removal of Cr(VI), and $CO_2$ mitigation. Additionally, it highlights the burgeoning roles of ZnSe in gas sensing, particularly for $NO_2$, $NH_3$, and acetone, and as an anode material in $Li^+$, $Na^+$, and $K^+$ ion batteries, thereby highlighting its expanding significance within environmental and energy technology landscapes (Fig. 1). By seamlessly integrating discussions on photocatalysis, sensing, and energy storage, this review offers a timely and holistic perspective on ZnSe as a versatile platform for sustainable technological solutions. Mechanistic insights into these remediation pathways are comprehensively outlined. The article concludes by delineating inherent challenges and mapping out future research directions and strategic avenues for material optimization, anticipated to drive continued innovation and deeper exploration within this dynamic field.

## 2. Fundamental properties of ZnSe

ZnSe is a binary octet semiconductor. Fig. 2(a and b) displays two allotropes of ZnSe: the hexagonal wurtzite (W) and the cubic zinc blende (ZB) structures.[44] The dihedral configuration of the fourth interatomic bond determines the variation among them. In contrast to W's ABABAB arrangement, ZB's coordination number is 4, and Zn and Se are aligned in an ABCABC fashion. W structure's lattice parameters are $a = b = 3.98$ Å, $c = 6.53$ Å (space group = $P6_3mc$), while the experimental calculated parameters of ZB are $a = b = c = 5.68$ Å (space group = $F\bar{4}3m$).[49] The lattice parameters of the W structure, as computed by Dai *et al.*,[50] are $a = b = 4:005$, $c = 6:657$, which slightly exceeds the experimental result. ZnSe shows the so-called W-ZB polytypism due to an insignificant variation in total energy between the ZB and the W structure (5.3 meV per atom) despite ZB being the low-temperature ground state structure.[51] At ambient temperature, the bulk band gap $E_g$ of cubic ZnSe is 2.7 eV (460 nm).[44]

ZnSe exhibits large-scale property variations owing to minute variations in atom configurations. Acharya *et al.* discovered that a distinct shift in the ZnSe nanorods' polarization-dependent optical characteristics coincided with the lattice configuration transition from W to ZB. Unlike the random rods, the aligned rods display polarization at a right angle to their long axis.[53]

An essential part of understanding the optoelectronic properties of nanoscale optoelectronics is nanostructures rather than differences in atomic patterns. Reiss unveiled that a significant relationship exists as a function of the ZnSe bandgap and its radius ($r$) (Fig. 2(c))[52] through the application of the Brus formula. Their research also highlighted the remarkable size-induced optoelectronic behavior of ZnSe nanocrystals.[52,54] Moreover, their findings suggested that the optical behavior of ZnSe thin sheets is strongly influenced by thickness variations, which are determined by the deposition method.[55]

In a study by Yu *et al.*, first-principles calculations grounded in density functional theory (DFT) were carried out to explore the electronic and optical characteristics of zinc blende (ZB)

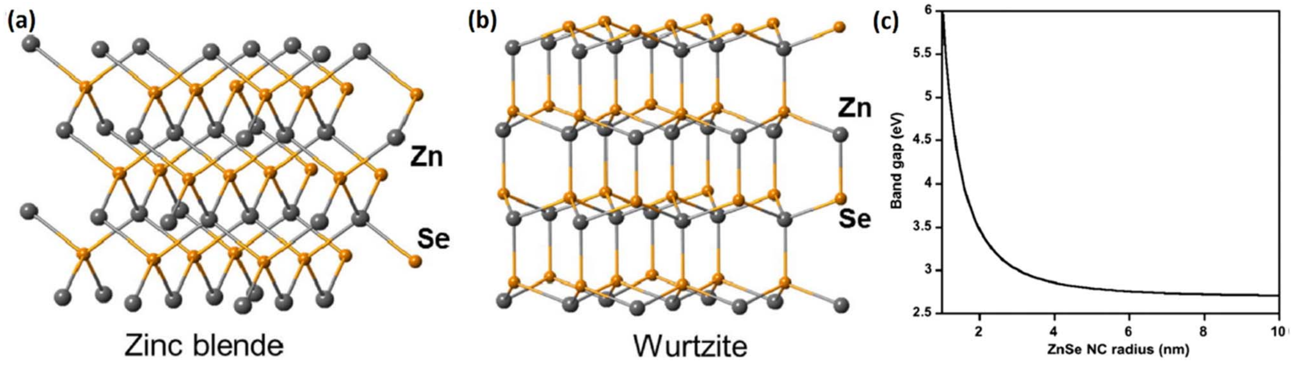

Fig. 2 Schematic representation of (a) zinc blende, (b) wurtzite crystal structures (reproduced from ref. 44); and (c) ZnSe NCs' band gap and size are correlated (reproduced from ref. 52). "This figure has been reproduced from ref. 44 with permission from Elsevier, copyright 2016". "This figure has been reproduced from ref. 52 with permission from Royal Society of Chemistry, copyright 2007".

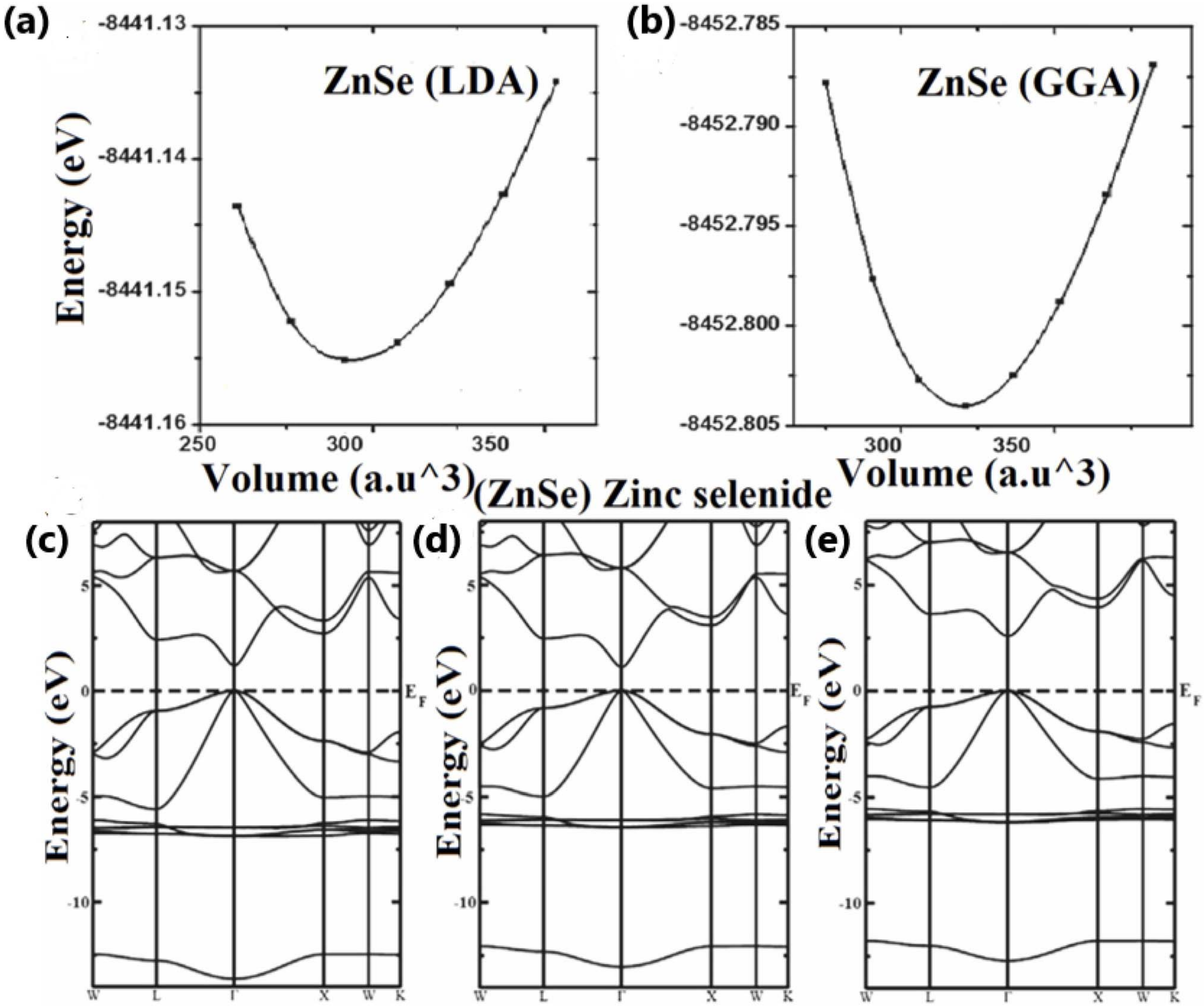

Fig. 3 Energy *versus* volume curve for ZnSe by utilizing (a) LDA and (b) GGA; band illustration of ZnSe by utilizing (c) LDA, (d) GGA, and (e) mBJ-GGA (reproduced from ref. 57). "This figure has been reproduced from ref. 57 with permission from Springer Nature, copyright 2017".

ZnSe.[56] Similarly, Kabita and Sharma investigated the structural and electronic properties of ZnSe using generalized gradient approximation (GGA), local density approximation (LDA), and the modified Becke–Johnson potential (mBJ-GGA) (Fig. 3).[57] The resulting structural parameters from these calculations aligned well with earlier literature, validating their use for subsequent electronic structure analysis.[57] Across all three computational methods, the valence band maximum (VBM) and conduction band minimum (CBM) were consistently located inside the Brillouin zone, Γ point, clearly indicating the direct bandgap nature of ZnSe. Notably, two key observations emerged: the upward shift of the conduction band (CB) and the corresponding broadening of the bandgap. The calculated bandgaps were 1.12 eV and 1.05 eV using the GGA and LDA methods, respectively. In contrast, the mBJ-GGA approach yielded a significantly improved bandgap of 2.5 eV, closely aligning with the experimental value of 2.7 eV. The slight discrepancy between the mBJ-GGA and experimental results can be attributed to the fact that the DFT calculations were conducted at absolute zero, whereas the experimental measurements were performed at room temperature. As shown in Fig. 3, the lower energy bands in the LDA calculations are primarily influenced by the Se atom's s-states around 3.12 eV, with this contribution shifting to higher energies in the GGA and further in the mBJ-GGA results, following the trend LDA < GGA < mBJ-GGA. In the valence band region, the Zn d-orbitals exhibit a strong presence in LDA, contributing approximately 34.94 eV, which decreases under GGA and increases again with the mBJ-GGA approach. These variations underscore the superior capability of the mBJ-GGA functional in accurately representing the electronic states, thus offering a more reliable depiction of ZnSe's band structure compared to GGA and LDA.[57]

## 3. Solution-based synthesis of ZnSe

The synthesis of ZnSe nanomaterials can be achieved through hydrothermal, co-precipitation, microwave-assisted, and reverse osmosis methods, each with distinct advantages and

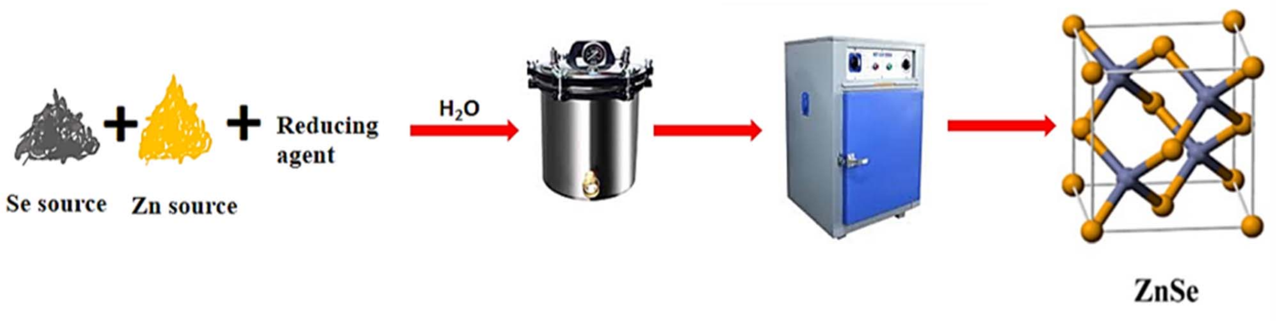

Fig. 4 Schematic representation of a hydrothermal method for the synthesis of zinc selenides (reproduced from ref. 60).

limitations. The hydrothermal method utilizes high temperature and pressure in an autoclave, producing highly crystalline ZnSe with precise control over size and morphology, though it requires expensive equipment and significant energy input. In contrast, the co-precipitation method is simpler and more economical, involving the reaction of zinc and selenium precursors at room or mild temperatures, albeit with potentially lower crystallinity. The microwave-assisted method offers rapid and uniform heating, significantly reducing reaction times while enhancing energy efficiency, often resulting in ZnSe with superior purity and uniformity. Although less commonly used for ZnSe synthesis, the reverse osmosis method serves primarily for purification or separation rather than direct production, limiting its applicability. The selection of the synthesis method is governed by factors such as cost, scalability, and the desired material properties.

### 3.1. Hydrothermal synthesis

When it comes to synthesizing nanomaterials, the hydrothermal approach reigns supreme. The hydrothermal method provides several advantages for nanomaterial synthesis, yielding particles with uniform size distribution, ultra-fine dimensions, and high crystallinity. Additionally, it generates relatively low waste, making it an environmentally friendly approach.[58] However, the method has limitations, such as the inability to monitor crystal growth in real-time and the high cost of the required equipment.[59] The process usually begins with dissolving the metal and selenide salts in water and then moving the mixture to a sealed autoclave. Here, the nanocrystals are grown under high temperatures and pressure. Fig. 4 shows a hydrothermal procedure used to synthesize transition metal selenides.[60]

Reports of ZnSe synthesis by hydrothermal methods date back to the 1970s. The initial hydrothermal synthesis of ZnSe crystals from $OH^-$ solutions with or without $Li^+$ was accomplished in 1970 by Kolb and Laudise.[61] Prior to 2008, a limited number of studies had been conducted on the synthesis of ZnSe. In 2008, Cao *et al.* explored the photocatalytic activity of 3D flower-like ZnSe nanostructures under UV light that were synthesized by hydrothermal treatment.[29] Compared to P25 and ZnSe microspheres, the ZnSe nanostructures synthesized by Cao demonstrated superior photocatalytic activity. Subsequently, ZnSe/Cu nanocrystals were fabricated at a temperature of 160 °C for 50 min utilizing NaHSe, $Zn(NO_3)_2$, and $Cu(NO_3)_2$.[62] The pH was maintained using NaOH, and the solution was stabilized with 3-mercapto propionic acid.

Later, the influence of temperature on the synthesis of ZnSe microspheres was demonstrated by Duan.[63] It was observed that the crystallinity of the material improved with the rise in the reaction temperature, and the intensity of the diffraction peaks increased. According to the study, 180 °C was found to be the ideal temperature of achieving highly crystalline ZnSe nanostructures, fabricated using zinc nitrate and sodium selenite, together with hydrazine and NaOH for 4 hours. In contrast to this study, higher temperatures were employed by Sobhani *et al.* to synthesize ZnSe nanospheres using the metal salt, $SeCl_4$, and $N_2H_4$.[62–64]

Additionally, Bu *et al.* investigated the mechanism of the fabrication of ZnSe micrograsses and microspheres that involved 36 hours at 190 °C (eqn (1)–(4)).[65] The microspheres were grown on graphene oxide sheets, and their various morphologies were created by varying the NaOH and EDTA concentrations.

$$Zn^{2+} + 2OH^- \rightarrow Zn(OH)_2\downarrow \tag{1}$$

$$Zn(OH)_2 + 2OH^- \rightarrow [Zn(OH)_2]^{2-} \tag{2}$$

$$[Zn(OH)_2]^{2-} + Se^{2-} \rightarrow ZnSe\downarrow + 4OH^- \; Zn^{2+}(EDTA)^+ \tag{3}$$

$$Se^{2-} + Zn^{2+} \rightarrow ZnSe\downarrow \tag{4}$$

Interestingly, utilization of a fresh Se source enabled reactions to proceed at reduced temperatures and in shorter timescales than those reported earlier.[66] ZnSe was fabricated using $ZnCl_2$ and $Na_2SeSO_3$ at 150 °C for 6 hours. Additionally, a nanohybrid comprising zinc selenide and smectites was developed. The round-shaped nanoparticles with diameters less than 5 nm in this nanohybrid developed in the interlayer gap of smectites.

### 3.2. Co-precipitation method

Zinc selenide (ZnSe) nanoparticles are commonly synthesized using the co-precipitation approach. The co-precipitation method is recognised for its simplicity, low cost, and rapid

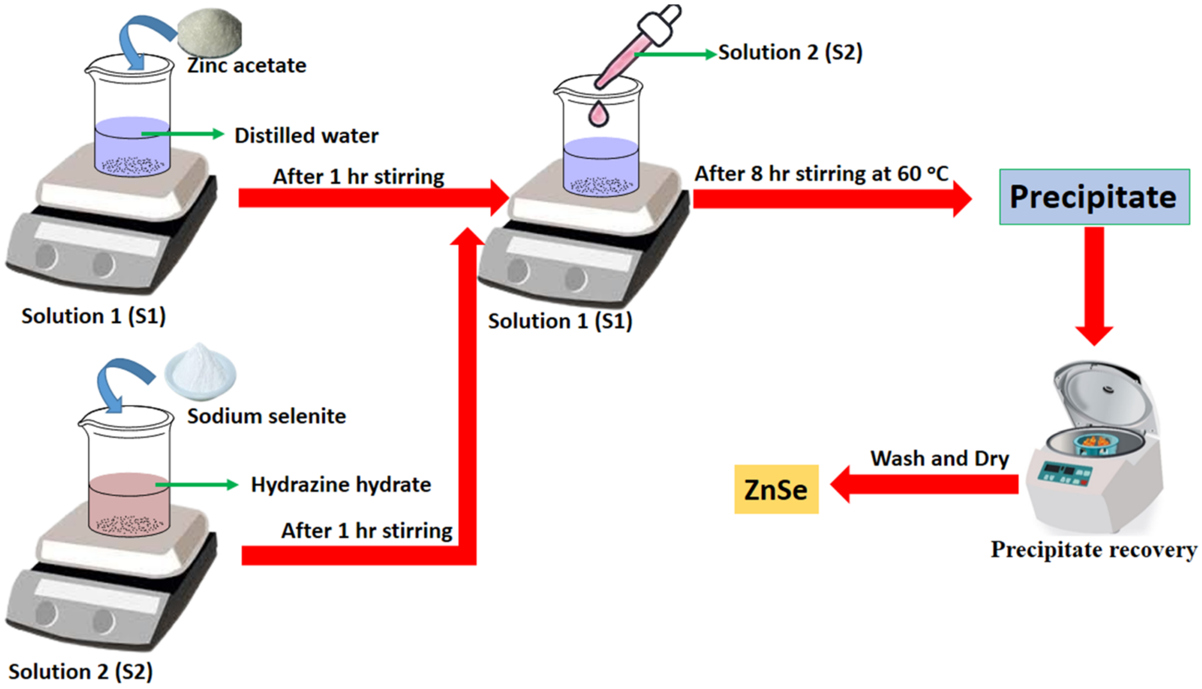

Fig. 5 Schematic representation of co-precipitation method for the synthesis of ZnSe (self-produced).

synthesis, making it suitable for large-scale industrial production. It enables the formation of high-purity nanomaterials through an environmentally friendly route, avoiding hazardous solvents and extreme conditions.[67] Nevertheless, this method provides limited control over nanoparticle size and uniformity, and the crystallinity of the products is generally lower than that achieved *via* hydrothermal synthesis.[68] The underlying principle of co-precipitation involves the simultaneous precipitation of two or more ionic species from a solution to form a compound, which allows the straightforward fabrication of nanomaterials. ZnSe nanoparticles were produced by co-precipitating zinc ions ($Zn^{2+}$) and selenium ions ($Se^{2-}$) as outlined in Fig. 5.

Table 1 Summary of the synthesis of ZnSe using different approaches

| Catalyst | Synthetic approach | Morphology | Ref. |
|---|---|---|---|
| ZnSe | Hydrothermal | Hollow-sphere | 95 |
| | | Nano sphere | 96 |
| | | Spherical | 97 |
| | | Hollow microspheres | 98 |
| | | Rose-like nanoflowers and microspheres | 99 |
| | | Zinc-blende crystalline structure | 100 |
| | | Grass-like | 101 |
| | | Sphere | 102 |
| ZnSe | Coprecipitation | Spherical | 71 |
| | | Nanorods | 103 |
| | | Single-phase nanocrystal | 104 |
| | | Quasi-spherical | 72 |
| | | Spherical | 73 |
| | | Nanorods | 105 |
| | | Nanorods | 106 |
| ZnSe | Microwave | Spherical shape | 78 |
| | | QDs | 79 |
| ZnSe | Reverse micelle | Cubic | 93 |
| | | QDs | 94 |

ZnSe nanoparticles were synthesized by Ahamad and his team by utilizing polyvinylpyrrolidone (PVP) as a capping agent in a straightforward, affordable co-precipitation method using zinc chloride and sodium selenide.[69] Studies have demonstrated the effect of Zn/Se molar ratios on the shape and photocatalytic potential of ZnSe nanostructures through a series of controlled tests with varying concentrations of selenium anions.[70] It was observed that the sample having a 1 : 0.6 Zn/Se ratio displayed nanobelts (NBs) as its morphology. Similarly, other sources such as $Zn(CH_3COO)_2 \cdot 2H_2O$ and selenium powders, with thiourea ($CH_4N_2S$) as the surfactant agent was employed by Sanchez-Martinez *et al.*[71] During the same period, Beena *et al.* synthesized ZnSe nanoparticles *via* a two-step procedure.[72] Step one involved dissolving zinc acetate in deionized water with constant magnetic agitation and adding 2-mercaptoethanol. In contrast, sodium borohydride ($NaBH_4$), selenium powder, and deionized water were used to prepare sodium hydrogen selenide (NaSeH), which was continuously stirred. The solutions of zinc and selenium were then mixed, stirred, and heated to 100 °C while keeping a pH of 10 using NaOH solution. The second phase reactions were conducted at 100 °C for over 24 hours, yielding a white-yellowish precipitate, which was washed and heated in a vacuum at 80 °C for 48 hours. Finally, the collected sample was heated using several temperature ranges, including 200 °C, 400 °C, 600 °C, and 800 °C.[72] A modified co-precipitation approach was reported by Gupta *et al.* by employing zinc sulphate and selenium powder as sources of zinc and selenium, respectively, at 60 °C for 8 hours with the use of hydrazine hydrate and ethylenediamine as reacting agent.[73] The resulting black precipitate was cleaned and dried in an open environment for 5 hours at 100 °C.

### 3.3. Microwave synthesis

Microwave synthesis is a fast and energy-efficient method for producing versatile semiconductor material. It offers rapid and uniform heating, high reaction efficiency, and the ability to control particle size and morphology by adjusting reaction conditions. The homogeneous heating minimizes thermal gradients, facilitating consistent nucleation and growth and producing nanomaterials with uniform size distribution.[74] However, this method has limitations, including safety concerns, and low reproducibility of the synthesis procedures.[75] In this process, zinc precursors, such as zinc salts, react with selenium sources, like selenium powder or selenides, in an appropriate solvent. The reaction mixture is subjected to microwave irradiation, which heats the system rapidly and evenly, facilitating the formation of ZnSe in a significantly shorter time compared to conventional heating methods.[76,77] This rapid heating accelerates the nucleation and growth of ZnSe crystals, resulting in high-purity products with controlled particle size and morphology. The advantages of microwave synthesis include reduced reaction times (often minutes instead of hours), improved energy efficiency, and better reproducibility, making it an ideal technique for producing ZnSe for applications in optoelectronics, solar cells, and infrared devices.

Shakir and co-workers were the first to synthesize ZnSe nanoparticles using a microwave heating method.[78] Water-soluble glutathione-capped ZnSe quantum dots were synthesized through microwave irradiation by dissolving $Zn(NO_3)_2 \cdot 6H_2O$ and glutathione (GSH) in 50 mL of deionized water, with the addition of $Na_2SeO_3$ and excess $NaBH_4$ while stirring continuously.[79] After a few minutes, the pH of the solution was carefully elevated to 10 using NaOH. The mixture was then exposed to microwave irradiation (300 W) and refluxed at 100 °C for 60 min. After the solution was cooled to ambient temperature, the quantum dots (QDs) were precipitated with 2-propanol and re-dissolved in deionized water. This purification process was carried out for three cycles, and the final ZnSe QDs were dried under vacuum.

### 3.4. Reverse micelle synthesis

When a surface active substance is added in a mixture of aqueous and organic phases, reverse micelles are formed.[80] Drug delivery,[81,82] micro-reactors,[83] and general detergents[84] are just a few of the possible and practical uses for these micelle systems. The preparation of nanoparticles to create hybrid materials comprising polymers and inorganic components is an additional advancement in the approaches.[85] Particles with regulated morphology and structure have been created using various techniques; however, the employment of reverse micelles appears to be particularly well-suited for nanoscale particle size customization.[86,87] It is also well known that the composition of the reverse micelles significantly influences the final size and shape of the nanocrystals.[88] Reverse micelle synthesis provides control over particle size and ensure uniformity in both concentration and morphology.[89] However, one of the major drawbacks of this methods is the requirements of costly chemicals or specifically designed surfactants.[90–92] It has been utilized to fabricate semiconductor nanostructures, and several copolymer reverse micelles serving as models for the preparation of inorganic nanoparticles.[90–92]

ZnSe nanoparticles, synthesized by reverse micelle approach, was first reported by Quinlan *et al.* utilizing an ion exchange process.[93] The method begins with the addition of sodium di-octyl sulfosuccinate salt (AOT) to heptane in a reaction vessel, forming reverse micelles while being continuously stirred. After forming reverse micelles, $Zn(ClO_4)_2$ was injected into the reaction vessel, followed by the addition of $Na_2Se$ solution to the mixture initiating the reaction of ZnSe. Furthermore, a gas-contacting method for synthesizing ZnSe nanocrystals was described by Karanikolos *et al.*[94] The hydrogen selenide gas was bubbled into a microemulsion of formamide/poly(ethylene oxide)–poly(propylene oxide)–poly(ethylene oxide)/*n*-heptane using this method. The gas then diffused into the center of the reverse micelles and reacted with the diethylzinc to produce ZnSe.[94] Table 1 summarizes the synthesis of ZnSe using different synthetic approaches.

## 4. Characterization of ZnSe

The characterization of ZnSe nanomaterials is vital for gaining insights into their structural, compositional, surface, and optical characteristics. This section explores the essential analytical methods such as XRD, SEM, TEM, EDAX, UV-visible (UV-vis) Spectroscopy, and Photoluminescence (PL) Spectroscopy, each providing valuable insights into the unique attributes of ZnSe nanomaterials.

### 4.1. Structural characterization

**4.1.1. X-ray diffraction (XRD) analysis.** X-ray diffraction (XRD) serves as a vital tool for characterizing ZnSe nanomaterials, offering detailed information about their crystalline structure, phase composition, and crystallite size. ZnSe typically crystallizes in cubic (zinc blende) or hexagonal (wurtzite) forms, each displaying unique diffraction patterns. The XRD patterns of ZnSe nanoparticles synthesized *via* the chemical bath deposition technique exhibited distinct peaks at 27.8°, 45.7°, and 54.3°, which corresponded to the (111), (220), and (311) planes of the cubic ZnSe phase (Fig. 6(a)).[107] The samples were labeled as A for 0.2 M, B for 0.5 M, and C for 1 M concentration of zinc acetate, respectively. These peaks proved the formation of single-phase cubic ZnSe, with no additional phases or impurities present. The broadening of the (111), (220), and (311) diffraction peaks is evidence of nanoparticle formation. On the other hand, the ZnSe NPs synthesized using a straightforward co-precipitation method, followed by annealing at different temperatures, revealed a cubic (face-centered) crystal structure consistent with JCPDS file No. 88-2345.[108] The XRD pattern in Fig. 6(b) displayed peaks at 27°, 45°, 53°, 65°, and 72°

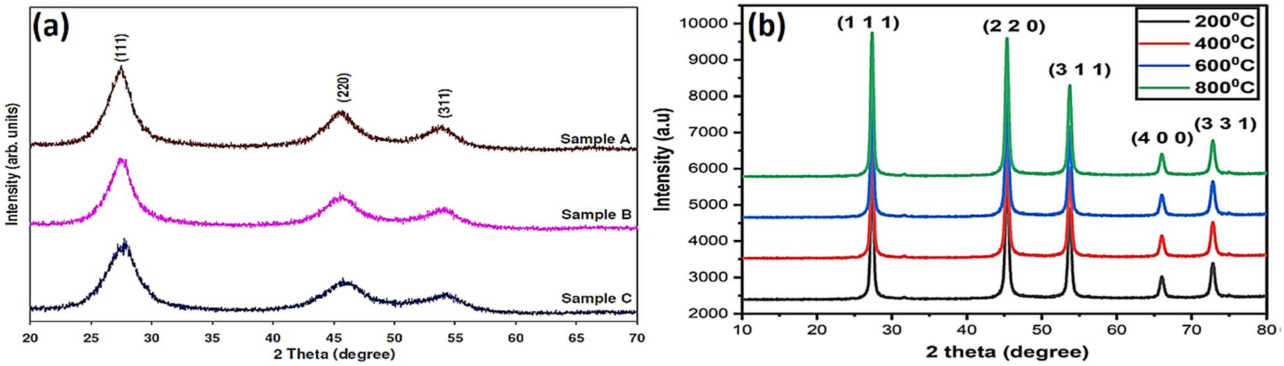

Fig. 6 XRD patterns of the synthesized ZnSe nanoparticles synthesized *via* (a) chemical bath deposition method (reproduced from ref. 107) and (b) co-precipitation method followed by calcination at various temperatures (reproduced from ref. 108). "This figure has been reproduced from ref. 107 with permission from AIP Publishing, copyright 2014". "This figure has been reproduced from ref. 108 with permission from Springer Nature, copyright 2021".

corresponding to the (111), (220), (311), (400), and (331) lattice planes. As the annealing temperature rises, the intensity of the peaks progressively intensifies, and the particle size increases, suggesting enhanced crystallinity and structural ordering of the ZnSe NPs.

### 4.2. Morphological characterization

**4.2.1. Scanning electron microscopy (SEM).** SEM is highly effective for studying ZnSe nanomaterials, as it generates high-resolution images that reveal detailed surface characteristics. SEM enables precise surface morphology analysis, capturing the texture, shape, and structure of particles, along with their size, which is crucial for predicting the efficacy of the material in different applications. The interaction of the electron beam with the atoms on the ZnSe surface produces signals, forming a detailed image of the material's topography, essentially mapping the "landscape" down to minute features. For instance, the SEM micrograph of ZnSe NPs, synthesized by Sharma *et al.*, highlights a combination of nanorods and spherical particles (Fig. 7(a)).[107] The nanorods measured between 400 nm and 3 μm in length, with diameters ranging from 50 to 100 nm. At higher magnification, it is evident that the larger spherical particles consist of agglomerated nanoparticles, each measuring under 10 nm (Fig. 7(b)). Similarly, Fig. 7(c) and (d) depict the SEM images of ZnSe microdisks at

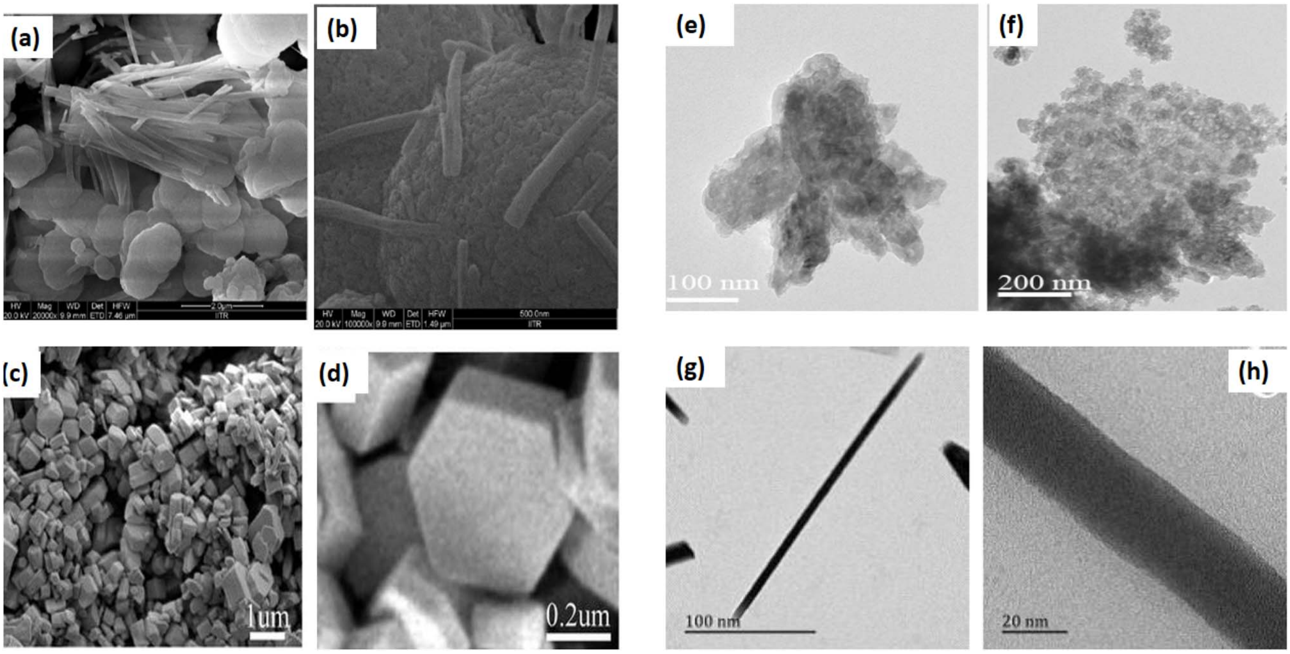

Fig. 7 (a and b) SEM image of the as-synthesized ZnSe nanoparticles (reproduced from ref. 107); (c and d) SEM images of ZnSe microdisks (reproduced from ref. 109); (e and f) HRTEM images of the sample calcined at 800 °C (reproduced from ref. 108); (g) TEM, and (h) HRTEM images of the as-synthesized ZnSe nanoflowers (reproduced from ref. 110). "This figure has been reproduced from ref. 108 with permission from Springer Nature, copyright 2021". "This figure has been reproduced from ref. 109 with permission from Springer Nature, copyright 2016". "This figure has been reproduced from ref. 110 with permission from Elsevier, copyright 2016".

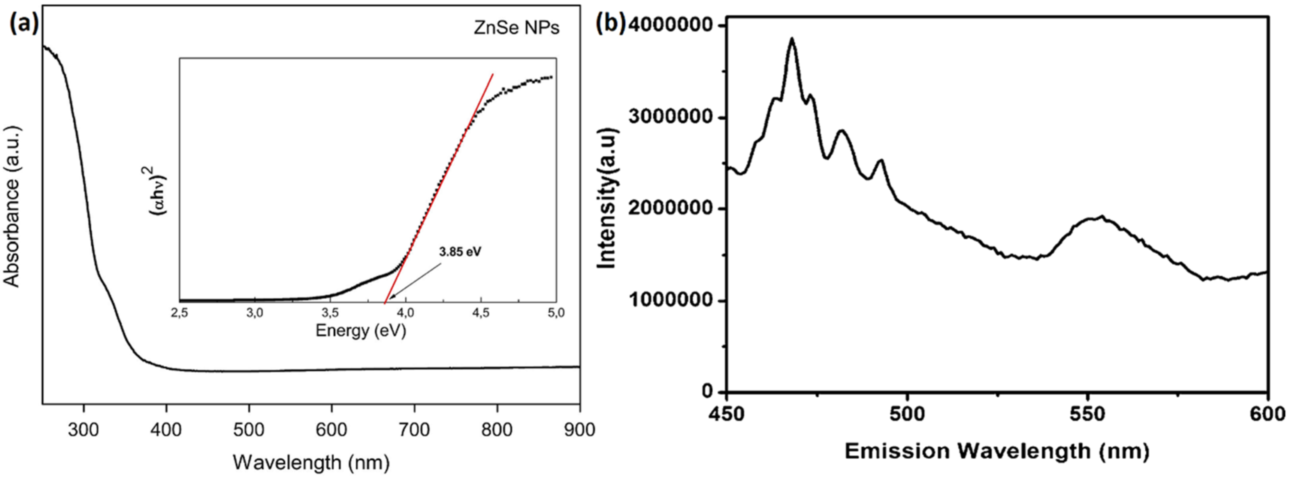

Fig. 8 (a) Absorbance spectrum and the band gap energy plot (inset) (reproduced from ref. 111), and (b) PL spectrum of the as-synthesized ZnSe NPs (reproduced from ref. 110). "This figure has been reproduced from ref. 111 with permission from Elsevier, copyright 2017". "This figure has been reproduced from ref. 110 with permission from Elsevier, copyright 2016".

low and high magnifications, respectively, as reported by Li *et al.*[109] The microdisks, synthesized through a solvothermal approach followed by annealing in an argon atmosphere, exhibit uniform morphology with diameters ranging from 0.4 to 0.6 μm and thicknesses between 0.1 and 0.4 μm.

**4.2.2. Transmission electron microscopy (TEM).** TEM provides a comprehensive analysis of the morphology and size distribution of ZnSe nanoparticles, allowing the observation of their overall shape, surface characteristics, and particle dimensions. On the other hand, high-resolution TEM (HRTEM) offers a more detailed view by revealing the lattice fringes within the nanoparticles, which gives valuable insights into their atomic-level structure, including the arrangement and spacing of atoms in the crystal lattice. For instance, the TEM images, displayed in Fig. 7(e) and (f), of ZnSe NPs synthesized at 800 °C were captured at two different magnifications.[108] The nanoparticles exhibit a predominantly quasi-spherical shape with some variations, suggesting a large surface area that could enhance their catalytic and biological properties. The particle size observed is approximately 30 nm, consistent with the calculated crystallite size, further confirming the synthesis conditions. Meanwhile, ZnSe nanoflowers consisted of radially aligned ZnSe nanorods with smooth surfaces, as shown in the TEM images (Fig. 7(g) and (h)).[110] These nanorods were straight, long, and smooth. The HRTEM image revealed a *d*-spacing of approximately 3.3 Å, which matches the interplanar spacing of the cubic ZnSe (111) planes.

### 4.3. Elemental composition

**4.3.1. Energy dispersive X-ray analysis (EDAX).** EDAX is a vital tool for analyzing ZnSe nanomaterials, primarily used to confirm their elemental composition and purity. It detects the presence of zinc (Zn) and selenium (Se), ensuring their correct stoichiometric ratio, which is crucial for maintaining the desired properties of ZnSe. Additionally, EDAX helps identify any impurities or contaminants introduced during synthesis and provides insights into the uniformity of elemental distribution across the sample. By complementing structural and morphological analyses, EDAX ensures the chemical accuracy and quality of ZnSe nanomaterials, making it an indispensable technique in material characterization. For instance, the EDAX analysis of the ZnSe NPs synthesized by Sharma *et al.* reveals that both the nanorods and spherical nanoparticles consist of approximately 49 atomic percent zinc and 51 atomic percent selenium, demonstrating their nearly ideal stoichiometry and high chemical purity.[107]

### 4.4. Optical characterization

**4.4.1. UV-visible spectroscopy.** UV-vis spectroscopy is widely used to study the optical properties of ZnSe NPs, particularly for determining their band gap energy by analyzing the absorption edge. It also reveals size-dependent effects like quantum confinement and provides data on absorbance and transmittance, making it valuable for applications in optoelectronics. For instance, ZnSe NPs synthesized by Mosquera *et al.* using a top-down approach involving ultrasound at low temperatures displays an optical absorption edge around 320 nm (3.87 eV), attributed to the first exciton absorption caused by the $1S^{e}{-}1S^{h}_{2/3}$ transition (Fig. 8(a)).[111] Compared to the bulk ZnSe with band edge at 2.7 eV, the absorption edge exhibits a blue shift ($\Delta E_g = 1.17$ eV). The direct band gap ($E_g$) was calculated using the relationship between the absorption coefficient ($\alpha$) and photon energy ($h\nu$). By extrapolating the linear section of the $(\alpha h\nu)^2$ *versus* $h\nu$ plot to $\alpha = 0$, the band gap was found to be 3.87 eV, further confirming the blue shift. This shift towards higher energy is attributed to the quantum size effect of the ZnSe nanocrystals.

**4.4.2. Photoluminescence (PL) spectroscopy.** PL spectroscopy is used to analyze the optical properties of ZnSe NPs, helping to determine their band gap and identify defects or impurities. It reveals size-dependent changes in emission, such as quantum confinement effects, and assesses material quality by the sharpness of the emission peaks. For instance, the PL spectrum of ZnSe nanoflowers in Fig. 8(b) exhibited strong light emission at ambient temperature when excited at 211 nm.[110] Four peaks were observed at 468 nm (2.65 eV), 484 nm (2.56 eV), 494 nm (2.51 eV), and 554 nm (2.24 eV). The 468 nm peak was attributed to bulk band emission, while the others were associated with self-activated luminescence due to defects such as zinc vacancies or surface emission.[110]

### 4.5. Zeta potential analysis

Zeta potential studies are conducted in order to determine the charge stability of nanoparticles, predict their interactions with surfaces, and quantify the charges present in a material.[112] It represents the electrical charge on the surface of nanoparticles in a dispersion, which originates from the adsorption of ions from the surrounding medium.[113,114] Zeta potential can be positive or negative and plays a key role in determining the stability of nanofluids and colloidal systems.[115,116] A higher absolute value indicates better dispersion and stability, while a lower value suggests a higher likelihood of particle clumping or settling.[117] Zeta potential measurement is especially valuable for studying nanoparticle dispersions. ZnSe nanoparticles usually have a negative zeta potential, often falling between −30 mV and −57 mV. For example, ZnSe nanocrystals synthesized by Mir *et al.* using an aqueous method exhibited a zeta potential of −30 mV.[118] Similarly, Atef *et al.* reported that ZnSe nanoparticles coated with green seaweed (*Ulva fasciata*, ZnSe-Uf) against *Leishmania major* (*L. major*) had zeta potentials ranging from −35.6 mV to −57.9 mV.[119]

## 5. Surface modification techniques

ZnSe is a dual metal–semiconductor that possesses remarkable photo-electronic capabilities and a direct bandgap of 2.67 eV. It also has an excitation binding energy of 21 meV.[120,121] Considering its favorable photocatalytic capabilities, it has been considered as a potential photocatalyst demonstrating extensive usability in photocatalysis, including the removal of heavy metal ions, the generation of hydrogen, the reduction of $CO_2$, and the degradation of contaminants.[49,122] Despite these benefits, ZnSe has an unstable structure, and due to its narrow $E_g$ (2.7 eV), it possesses a high rate of charge carrier recombination during photocatalysis.[70] However, to overcome these constraints it requires some improvements. Certain modifications can be made to its structure to maximize its photocatalytic potential and broaden the range of applications for photocatalytic processes. The creation of heterojunctions and doping are two features of ZnSe enhancement techniques. These modification strategies minimize the band gap by incorporating dopant materials and significantly reduce the electron–hole pair recombination rate. This can be achieved by promoting charge carrier separation and improving migration efficiency through the development of heterojunctions. In the following

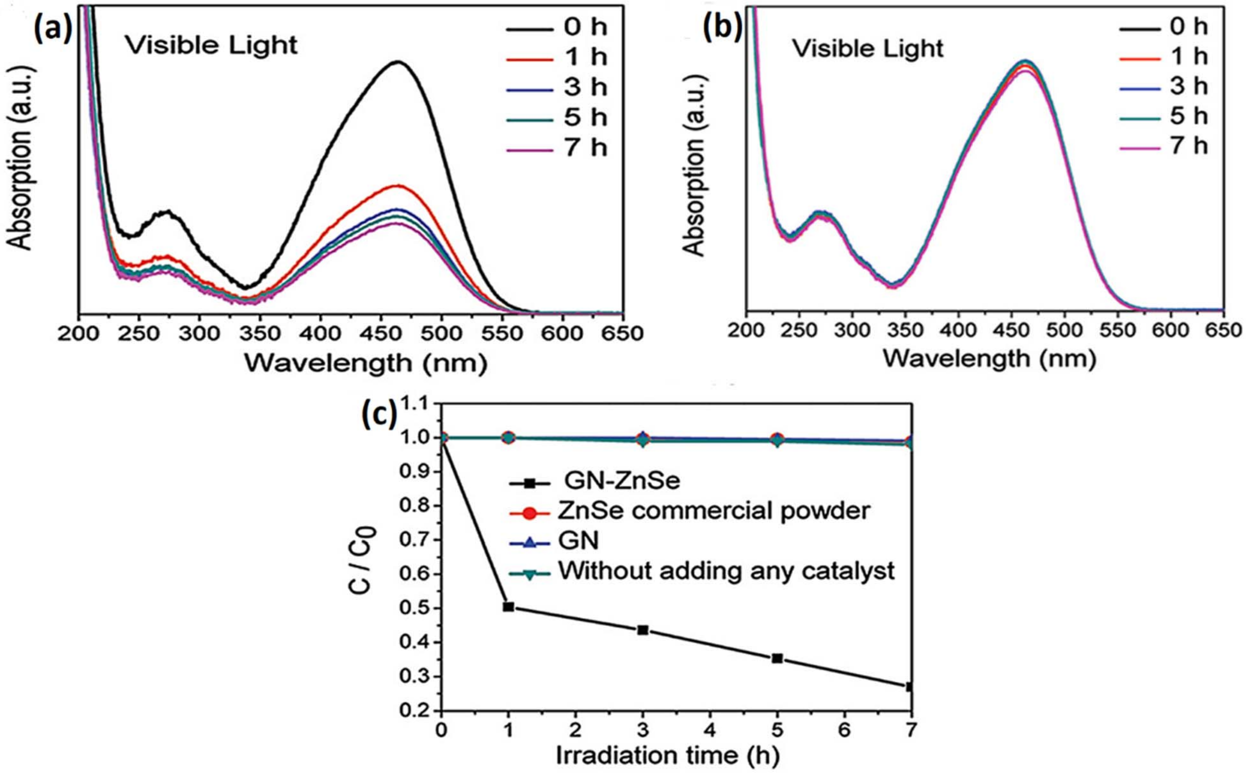

Fig. 9 UV-visible spectra for methyl orange solution in the presence of (a) GN-ZnSe composite, and (b) commercial ZnSe powder under visible light, and (c) Photobleaching curves of methyl orange under visible light in water using photocatalysts (reproduced from ref. 124). "This figure has been reproduced from ref. 124 with permission from American Chemical Society, copyright 2012".

section, doping and various heterojunctions, as well as their photocatalytic enhancements, are described.

### 5.1. Doping

The process of doping is a method that enhances charge carrier separations and minimizes the rate of photoinduced charge carrier recombination. This is accomplished by increasing the number of vacancies that are generated. Doping in semiconductors is an effective way of improving the efficiency of photocatalysts.[123] To narrow the bandgap and boost light absorption efficiency of ZnSe, various dopants are introduced into its lattice structure. This has sparked significant interest among researchers in exploring the doping of ZnSe photocatalysts with transition and non-transition metal ions, aiming to extend their light absorption into the visible spectrum. For instance, Chen *et al.* utilized a catalyst-free technique for the fabrication of N-doped graphene/ZnSe (GN-ZnSe) hybrid.[124] They found that these composites displayed remarkable photocatalytic efficiency in degrading methyl orange (MO) dye alongside optimized electrochemical behavior for oxygen reduction. Specifically, the GN-ZnSe hybrid bleached 71.50% of MO dye in 7 hours of UV-vis irradiation, as shown in Fig. 9(a). On the other hand, commercial ZnSe did not demonstrate any MO bleaching results Fig. 9(b). After 8 hours on GN-ZnSe composite, 30.72% of the dye had been consumed, but on commercial ZnSe, just 7.84% had been used.

Also, Kim and colleagues investigated the photocatalytic efficiency of Er and Yb doped ZnSe microspheres to degrade MO.[125] Similarly, Cu-doped ZnSe NPs were investigated for the photodegradation of MO and found it to be 87%.[126] Table 2 summarizes the various previous reported doped ZnSe nanoparticles along with their synthetic method.

Studies have described the use of a first-principle study to scientifically investigate the effects of metal and non-metal doping on ZnSe monolayer.[127] The electromagnetic characteristics of doped ultrathin tetragonal ZnSe monolayers were

Table 2 Summary of ZnSe nanoparticles doped with various dopants

| Catalyst | Dopant(s) | Synthesis method | Ref. |
|---|---|---|---|
| ZnSe | Nd | Hydrothermal | 129 |
| | Fe | Microemulsion-mediated hydrothermal | 130 |
| | Cu | Hydrothermal | 131 |
| | Ag | Hydrothermal | 132 |
| | $Co^{2+}$ | Hydrothermal | 133 |
| | La | Hydrothermal | 134 |
| | Ni, Cr, Co, and Ti | Co-precipitation | 135 |
| | Fe | Co-precipitation | 136 |
| | Sr | Co-precipitation | 137 |
| | Ni | Co-precipitation | 138 |
| | $Cr^{3+}$ | Co-precipitation | 139 |

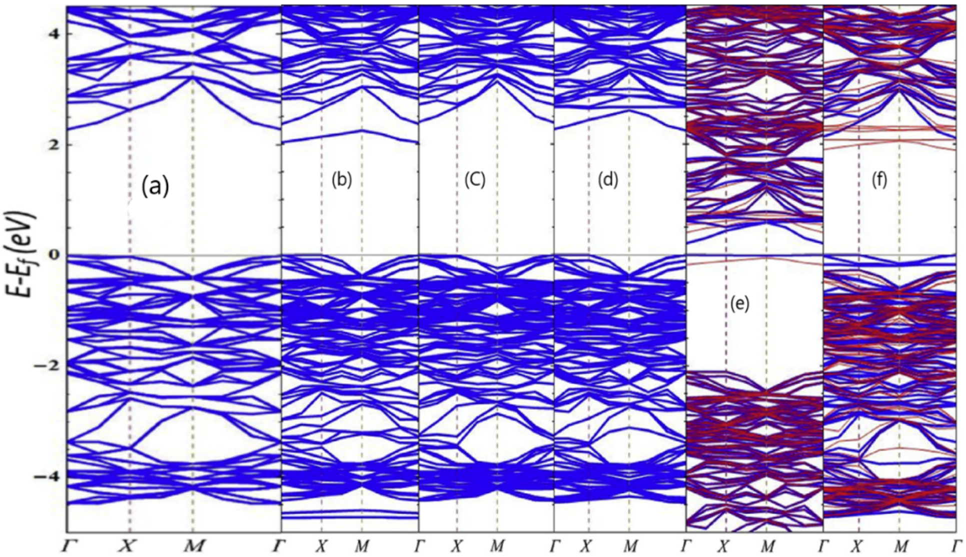

Fig. 10 (a) Band structure of undoped ZnSe monolayer, band alignments of (b) F-, (c) Ca-, (d) Sc-, (e) Ti-, and (f) Mn-doped monolayer of ZnSe. The spin-up and spin-down channels are donated by the blue and red lines, respectively, for spin-polarized calculations (reproduced from ref. 127). "This figure has been reproduced from ref. 127 with permission from Elsevier, copyright 2017".

explored by utilizing atoms of various metals and metalloids (K to As). It was observed that only the F atom was thermodynamically advantageous in replacing the Se site in both Se-rich and Zn-rich environments. In contrast, the Ca and Sc atoms were more beneficial in replacing the Zn site. Additionally, only in a Se-rich environment, atoms of Ti and Mn replaced only zinc sites. It was also observed that the pristine tetragonal ZnSe monolayer had a straight $E_g$ of 2.28 eV from Γ to Γ at the PBE level (Fig. 10(a)).[127] This discovery was in agreement with the other estimated value, which was 2.22 eV.[128] Furthermore, in conditions with excess Zn and/or Se, F, Ca, Sc, Ti, and Mn atoms were the only ones thermodynamically favoured to replace Se or Zn sites (Fig. 10(b–f)).

### 5.2. Formation of heterojunctions

When semiconductors with different band structures come together, a heterojunction forms, opening up a world of possibilities for band alignments. Conventional, p–n and Z-scheme heterojunction photocatalysts are the three main varieties of semiconductor-based heterojunctions.[140,141]

**5.2.1. Conventional heterojunction photocatalysts.** The heterojunction photocatalysts belonging to these classes can be broadly classified into type-I, type-II, and type-III. Compared to semiconductor B, semiconductor A has a higher CB and a lower VB for a type-I heterojunction photocatalyst (Fig. 11(a)).[142,143] Thus, in semiconductor B, holes and electrons collect at the VB and CB levels under light exposure, respectively. Therefore, in a type-I heterojunction photocatalyst, the decoupling of electron–hole pairs is significantly restricted, as both charge carriers are confined within the same semiconductor.[144] Furthermore, a redox reaction occurs mostly on the semiconductor, which has a decreased redox potential. This leads to a considerable decline in the heterojunction photocatalyst's overall redox performance.[145] On the other hand, the CB and VB values of semiconductor A are higher than those of semiconductor B in the type-II heterojunction photocatalyst (Fig. 11(b)).[143] Consequently, photoinduced electrons will go to semiconductor B, while photoinduced holes will migrate to semiconductor A when the semiconductor is exposed to light. This will result in the decoupling of electron–hole pairs.[146,147] As shown in Fig. 11(c),[143] the arrangement of the type-III heterojunction photocatalyst closely resembles that of the type-II heterojunction. However, the enhanced staggered gap prevents bandgap overlap, limiting electron–hole migration in the type-III heterojunction and diminishing its efficiency under visible light.[148,149] Therefore, of the heterojunctions discussed, the type-II heterojunction is evidently the most practical for boosting photocatalytic performance, as its structure enables effective spatial separation of electron–hole pairs.

In 2011, three unique type II three-dimensional ZnO/ZnSe heterostructures (H1, H2, and H3) were fabricated by Cho *et al.* using a process of solution-based surface modification method and employed them for the degradation of orange-II dye by the illumination of visible light.[150] The feasible fabrication mechanism can be outlined as follows (eqn (5)–(8)):

$$\mathrm{ZnO_{surface} + H_2O + 2OH^- \rightarrow Zn(OH)_4{}^{2-}} \tag{5}$$

$$\mathrm{SeO_3{}^{2-} + N_2H_4 \rightarrow Se + N_2 + H_2O + 2OH^-} \tag{6}$$

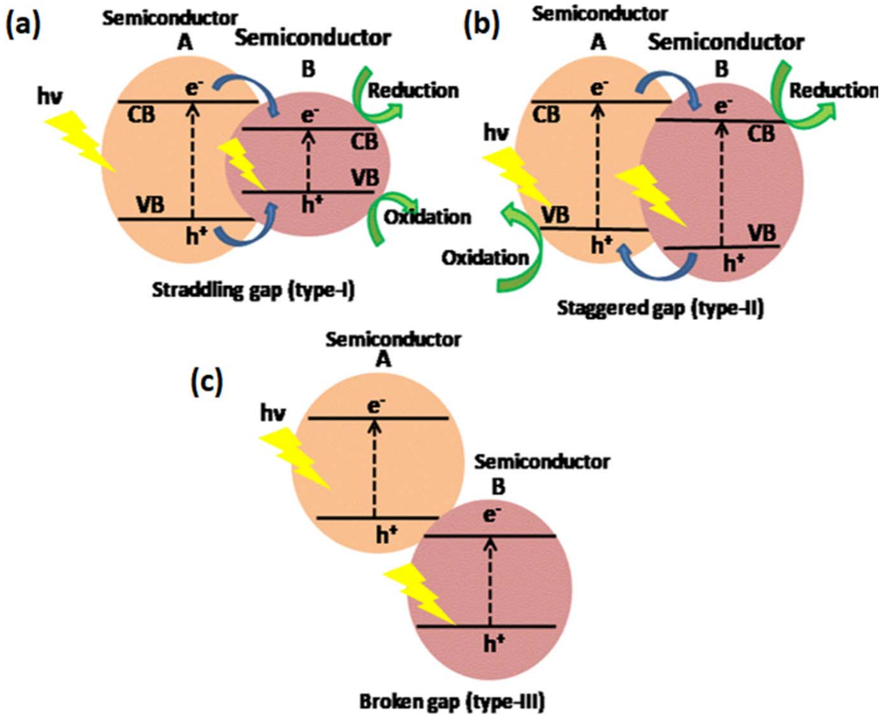

Fig. 11 Diagram showing the separation of electron–hole pair in three types of conventional heterojunction photocatalysts: (a) Type-I, (b) Type-II, and (c) Type-III (reproduced from ref. 143).

$$3Se + 6OH^- \rightarrow 2Se^{2-} + SeO_3^{2-} + 3H_2O \tag{7}$$

$$Se^{2-} + Zn(OH)_4^{2-} \rightarrow ZnSe + 4OH^- \tag{8}$$

Fig. 12(a) depicts the UV-vis absorption spectra of three-dimensional ZnO nanostructures (S1, S2, and S3) that were utilized as reaction substrates, as well as 3D ZnO/ZnSe heterostructures (H1, H2, and H3) that were produced as a result of surface modification reactions.[150] The 3D ZnO/ZnSe heterostructures and 3D ZnO nanostructures showed markedly different optical absorption characteristics, according to the spectra. The 3D ZnO nanostructures (S1, S2, S3) demonstrated strong UV absorption in the vicinity of the visible range, typical of ZnO with a broad bandgap. In contrast, the 3D ZnO/ZnSe heterostructures (H1, H2, H3) shows absorption peak in both the UV and visible regions. Again, type-II ZnSe/g-$C_3N_4$ heterojunctions were synthesized through ultrasonication and evaluated for PEC water splitting.[151] When compared to 0.5 ZG, 1 ZG photocatalyst, and pristine g-$C_3N_4$, the absorption spectra of the as-prepared 0.05 ZG photocatalyst exhibited a greater degree of visible light absorption (400–500 nm), which is indicated in Fig. 12(b). Further, the Tauc plot demonstrated that the $E_g$ was reduced from 2.76 eV to 2.60 eV for the 0.05 ZG photocatalyst in

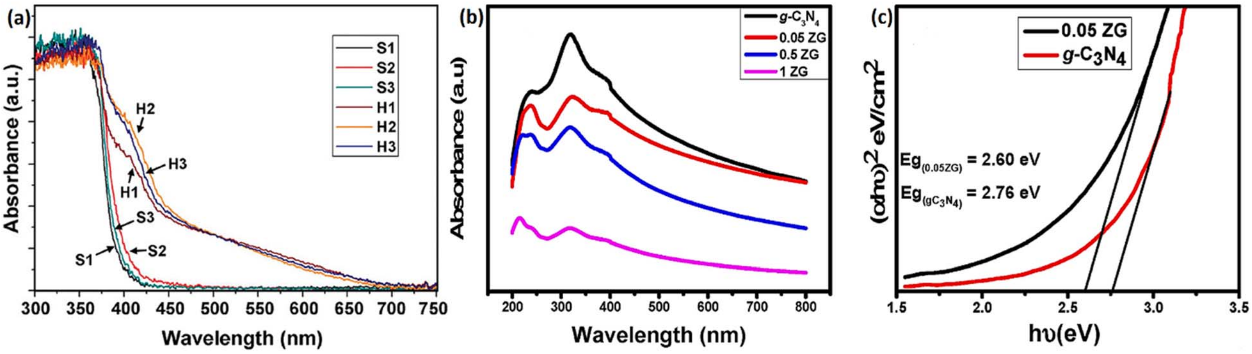

Fig. 12 (a) UV-vis absorption spectra of 3D superstructures (reproduced from ref. 150); (b) UV-visible absorption spectra of g-$C_3N_4$ and its heterostructures, and (c) Tauc plot of g-$C_3N_4$ and 0.05 ZG heterostructure for the determination of $E_g$ (reproduced from ref. 151). "This figure has been reproduced from ref. 150 with permission from American Chemical Society, copyright 2011". "This figure has been reproduced from ref. 151 with permission from Elsevier, copyright 2021".

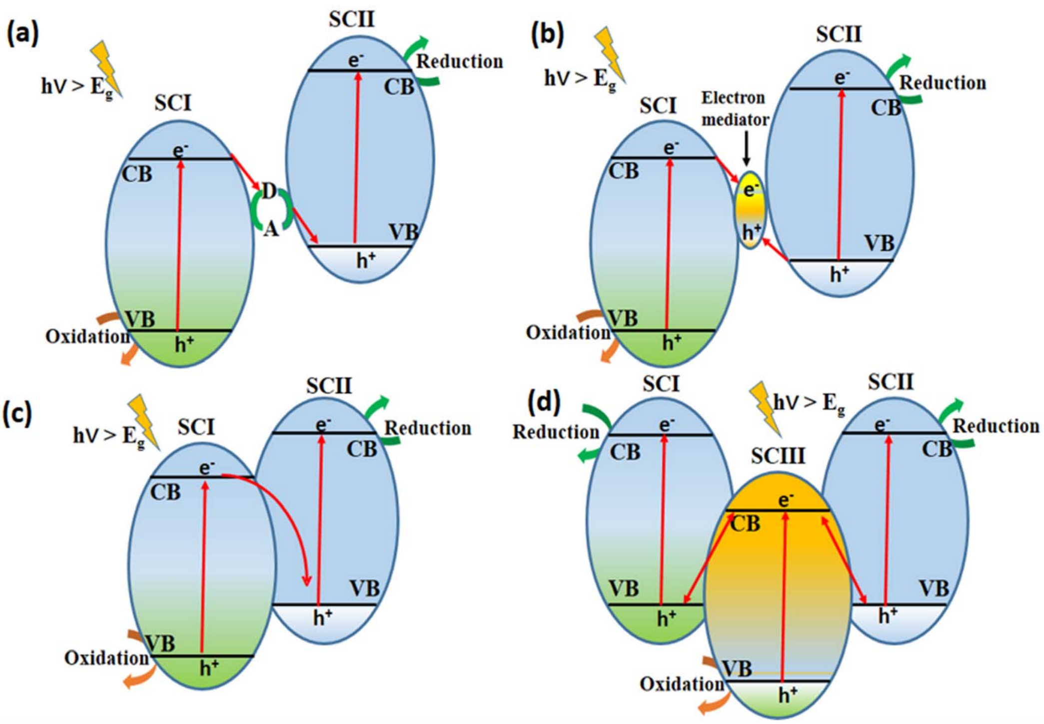

Fig. 13 A schematic overview of charge carrier migration in Z-scheme heterojunction photocatalysts when exposed to visible light: (a) conventional, (b) all-solid-state (ASS), (c) direct Z-scheme heterojunction, and (d) dual direct Z-scheme (reproduced from ref. 143).

comparison to the pristine g-$C_3N_4$ (2.76 eV) (Fig. 12(c)), reflecting the successful formation of type-II heterostructure.

**5.2.2. Z-scheme heterojunction photocatalysts.** The Z-scheme is an effective photocatalytic system that enhances the decoupling and transfer of photoinduced charge carriers, serving as an alternative to traditional heterojunctions.[152] A Z-scheme photocatalytic system can be distinguished as direct or indirect based on the presence of an electron mediator within the system. One of the components of a Z-scheme heterojunction photocatalyst is a reduction semiconductor with an elevated CB position (SC II), and the other component is an oxidation semiconductor with a reduced VB position (SC I). The presence of an electron mediator can sometimes be found, which ultimately results in an indirect Z-scheme photocatalyst. In 1979, Bard *et al.* presented the theory of Z-scheme heterojunction, which was influenced by the process of photosynthesis in plants.[153] The first applications of the Z-scheme heterojunction were in liquid-phase photocatalytic processes. Without significant direct contact, the redox mediator functions as an acceptor–donor pair at the semiconductor interface. As shown in Fig. 13(a),[143] the redox mediator acts as both a donor and an acceptor during light exposure, facilitating the transport of photoinduced electrons from the CB of SC I to the VB of SC II.[154] Consequently, oxidation and reduction reactions can occur successfully within this heterojunction system due to the accumulation of photoinduced holes in the VB of SC I and the accumulation of electrons in the CB of SC II.[145] Despite this, this system is confronted with several difficulties. For example, standard Z-scheme photocatalysts usually function in the liquid phase, which necessitates the exact control of the pH of the reaction environment. In addition, they frequently display poor charge transfer rates, which makes it difficult for them to be utilized in practical applications involving the degradation of contaminants. In addition, a great number of liquid-phase redox mediators are unstable and prone to deactivation, which leads to a decrease in the overall effectiveness of photocatalysis.[155]

In light of the constraints of liquid-phase Z-scheme heterojunction photocatalysts, researchers are seeking alternatives to boost the efficiency of indirect Z-scheme systems. In 2006, a novel Z-scheme photocatalyst was proposed, using an electron solid conductor and noble metal Au as an electron mediator instead of traditional redox couples, integrating CdS and $TiO_2$ and paving the way for all-solid-state (ASS) Z-scheme photocatalysts.[156] In this system, light energy greater than the semiconductors' band gaps excites electrons in SC I, generating holes in the VB. These electrons then move to the VB of SC II *via* conducting materials at the semiconductor interface (Fig. 13(b)),[143] maintaining redox capability and effective separation of the photoinduced carriers.[157] However, ASS Z-scheme semiconductor photocatalysts typically rely on rare and expensive electron mediators, and many experience a shielding effect, significantly limiting their long-term practical applicability.[158]

Research on direct Z-scheme photocatalysts began seven years after the proposal of the ASS Z-scheme heterojunction photocatalyst.[159] Direct Z-scheme photocatalysts, in contrast to traditional liquid-phase and ASS Z-scheme heterostructures, involve two semiconductors that are in close contact with one another (Fig. 13(c)).[143] This eliminates the requirement for an electron mediator. Notably, they successfully minimized backward reactions and light shielding effects without needing mediators while combining the advantages of indirect Z-scheme heterojunctions, such as effective decoupling of electron–hole pair and optimal redox potential.[160–162] Additionally, the development of an internal electric field at the interfaces of the direct Z-scheme system compensates for mediators, speeding up the recombination of charge carriers with lower redox potentials while preserving those with higher capabilities. Typically, the staggered band arrangement of two semiconductors results in an internal electric field only when both semiconductors have different work functions.[163]

Dual Z-scheme heterojunction photocatalytic systems with three semiconductors have recently attracted interest due to their distinct band alignment, charge transfer routes, and redox site locations. In a standard double Z-scheme heterojunction, charge carriers from the intermediate semiconductor (SC III) dissipate as they transfer from nearby semiconductors, leaving the outer semiconductors (SC I and SC II) to drive redox reactions, while SC III also contributes to oxidation or reduction (Fig. 13(d)).[143] In certain situations, electrons and holes on the intermediate semiconductor are depleted, leaving the peripheral semiconductors' charge carriers solely responsible for

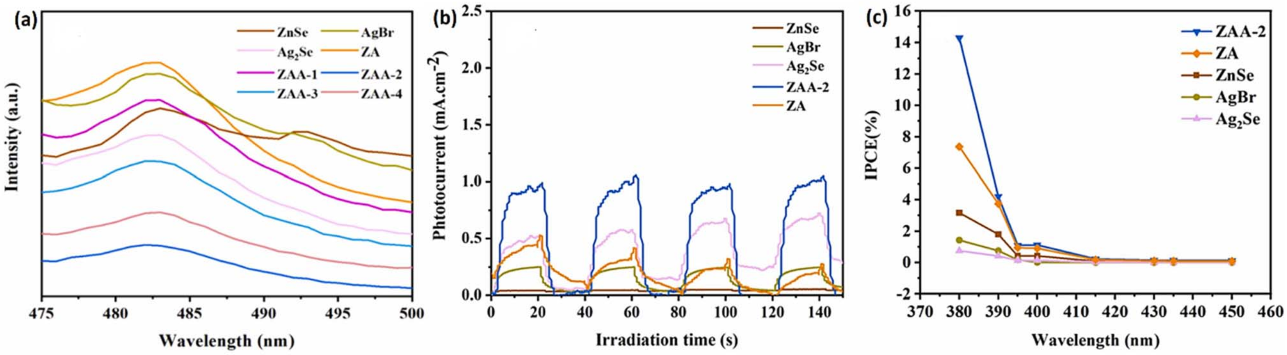

Fig. 14 (a) Photoluminescence spectra, (b) photocurrent response, and (c) IPCE of various fabricated samples (reproduced from ref. 165). "This figure has been reproduced from ref. 165 with permission from Elsevier, copyright 2023".

redox reactions.[164] For instance, Liang *et al.* fabricated a series $ZnSe/Ag_2Se/AgBr$ (ZAA) heterojunction by depositing ZnSe on the surface of AgBr, with the *in situ* generation of $Ag_2Se$ between the two components using a hydrothermal method and the resulting samples were labelled as ZAA-1, ZAA-2, ZAA-3, and ZAA-4, corresponding to ZnSe amounts of 0.15 g, 0.2 g, 0.25 g, and 0.3 g, respectively.[165] ZAA-2 displayed the lowest PL intensity at an excitation wavelength of 395 nm, indicating that it had the most efficient carrier separation (Fig. 14(a)). Additionally, the highest photocurrent response displayed by ZAA-2 under multiple on–off irradiations revealed efficient transport of photo-generated carriers (Fig. 14(b)). The incident photon-to-electron conversion (IPCE) efficiency, with ZAA-2 (14.30%) and ZA (7.37%) outperformed other materials (Fig. 14(c)). These findings demonstrate the superior light conversion efficiency of ZAA-2, where AgBr acts as a hole trap, ZnSe serves as an electron collector, and $Ag_2Se$ functions as an electron-buffer mediator, enabling effective separation and directional transfer of electrons and holes.

Despite extensive research, high efficiency in heterojunction photocatalysts remains elusive. Traditional type I/II systems are limited by ineffective suppression of charge carrier recombination and decreasing redox capabilities, hindering their broader use. In contrast, Z-scheme heterostructured photocatalysts enable efficient charge transfer and strong redox capabilities. However, conventional Z-scheme photocatalysts suffer from reduced light absorption because of redox ion mediators. In ASS Z-scheme photocatalysts, the scarce metal mediator can compete with the semiconductors for light absorption. Therefore, direct Z-scheme heterostructured photocatalysts are regarded as the most favourable heterojunction systems available till date.

## 6. Applications of ZnSe

ZnSe displays significant activity in environmental remediation due to its photocatalytic properties, enabling it to effectively break down pollutants in both aqueous medium and air. It serves as a catalyst in sustainable processes, such as water splitting and hydrogen generation. Additionally, ZnSe facilitates advanced oxidation processes (AOPs) in wastewater treatment, allowing for the targeted degradation of persistent organic chemicals like pesticides, herbicides, and pharmaceutical residues, textile dyes that are difficult to eliminate using conventional approaches. In the field of microbiology, ZnSe nanoparticles have gained attention as effective antimicrobial agents capable of inhibiting the growth of various bacteria, fungi, and viruses. This makes them valuable for developing disinfectants and antimicrobial coatings for medical devices and surfaces.

### 6.1. Photodegradation of pollutants

Rapid population growth and economic expansion have escalated water pollution, making it a critical global challenge. The rise in agricultural, industrial, and domestic activities has led to substantial degradation of river and groundwater quality, with toxic wastes contaminating these vital resources. These harmful pollutants pose serious threats to human health and disrupt the balance and integrity of ecosystems.[166,167] Significant sources of water contamination include heavy metal ions, dyes, phenols, polychlorinated biphenyls (PCBs), pharmaceutical residues, pesticides, and various non-natural compounds.[168–170]

Currently, a diverse set of methods ranging from physical and chemical to biological and hybrid techniques are being explored for the breakdown and mineralization of contaminants. Among the various methods, photocatalysis is notably promising and crucial due to its impressive efficiency, energy-saving advantages, gentle reaction conditions, and minimal generation of other pollutants. Consequently, it has attracted considerable interest from researchers in the scientific field.[171,172] Photocatalysis is a mechanism that accelerates the occurrence of a photoreaction through the use of a catalyst. The process works simply: when a photon with sufficient energy to meet or exceed the bandgap energy hits the catalyst, it produces a pair of charge carriers. This energy conversion triggers the generation of electrons and holes.[173] The electrons and holes generated by light interact with oxygen ($O_2$), water ($H_2O$), and hydroxyl groups, resulting in the production of reactive oxygen species (ROS) such as hydroxyl radicals ($^{\bullet}OH$) and superoxide radical anions ($O_2^{\bullet-}$), both of which have powerful oxidative capabilities.[174] After fluorine, these hydroxyl radicals exhibit the second-highest oxidation potential, measured at 2.8 eV.[174] These highly reactive species rapidly interact with organic molecules, with rate constants generally falling between $10^6$ and $10^9$ mol $L^{-1}$ $s^{-1}$.[175] They initiate a cascade of reactions with contaminants on the photocatalyst's surface, leading to the effective degradation of organic pollutants.[176]

According to Herrmann,[177] heterogeneous photocatalytic processes involve five distinct steps, specifically:

(i) Transfer of reactants to the catalyst surface, (ii) adsorption of one or more reactants, (iii) reaction of adsorbed reactants, (iv) desorption of products, and (v) diffusion of products away from the catalyst surface.

In the context of using ZnSe as a photocatalyst, the mechanism of heterogeneous photocatalysis can be described as follows:

$$\text{ZnSe} + h\nu \rightarrow \text{ZnSe}(\text{e}_{\text{conduction band}}{}^{-} + \text{h}_{\text{valence band}}{}^{+}) \quad (9)$$

Here, $\text{e}_{\text{conduction band}}{}^{-}$ and $\text{h}_{\text{valence band}}{}^{+}$ serve as reducing and oxidizing agents, respectively. The oxidation and reduction of pollutants are as follows (eqn 10–18):

Oxidative reaction:

$$\text{Organic pollutants} + \text{h}_{\text{valence band}}{}^{+} \rightarrow \text{oxidation products} \quad (10)$$

$$\text{ZnSe}(\text{h}_{\text{valence band}}{}^{+}) + \text{H}_2\text{O} \rightarrow \text{ZnSe} + \text{H}^{-} + {}^{\bullet}\text{OH} \quad (11)$$

This reaction proceeds with the neutralization of the $OH^-$ ion into $^{\bullet}OH$ by the $h^+$:

$$\text{ZnSe}(\text{h}_{\text{valence band}}{}^{+}) + \text{OH}^{-} \rightarrow \text{ZnSe} + {}^{\bullet}\text{OH} \quad (12)$$

$$\text{h}^{+} + \text{organic pollutants} \rightarrow \text{metabolites} \rightarrow \text{CO}_2 + \text{H}_2\text{O} \quad (13)$$

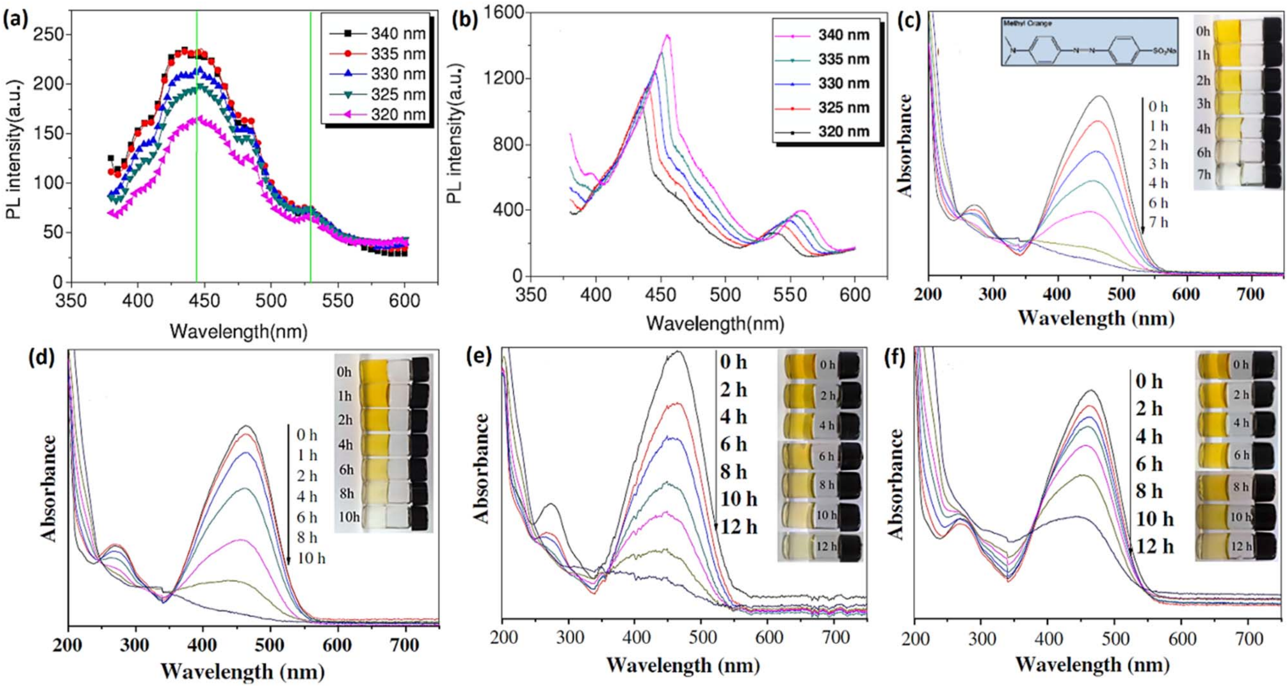

Fig. 15 Photoluminescence (PL) spectra of (a) ZnSe microspheres, and (b) commercially available ZnSe powder; temporal UV-visible absorption spectral shifts and related colour variations (insets) observed in MO solutions in the presence of (c) ZnSe microspheres, and (d) commercial ZnSe powder under UV light irradiation, temporal UV-visible absorption spectral shifts and related colour variations (insets) observed in MO solutions in the presence of (e) ZnSe microspheres, and (f) commercial ZnSe powder under visible light irradiation (reproduced from ref. 25). "This figure has been reproduced from ref. 25 with permission from IOP Publishing, copyright 2010".

Reductive reaction:

$$\text{Organic pollutants} + e_{\text{conduction band}}^{-} \rightarrow \text{reduction products} \tag{14}$$

In this process, $O_2^{\bullet-}$ is generated by the electron in the following manner:

$$\text{ZnSe}(e_{\text{conduction band}}^{-}) + O_2 \rightarrow \text{ZnSe} + O_2^{\bullet-} \tag{15}$$

$$O_2^{\bullet-} + H^+ \rightarrow HO_2^{\bullet} \tag{16}$$

$$HO_2^{\bullet} + H^+ + \text{ZnSe}(e_{\text{conduction band}}^{-}) \rightarrow H_2O_2 + \text{ZnSe} \tag{17}$$

$$^{\bullet}OH + \text{organic pollutants} \rightarrow \text{metabolites} \rightarrow CO_2 + H_2O \tag{18}$$

Within the outlined steps, the formation of hydroxyl radicals ($^{\bullet}OH$) and superoxide anion radicals ($O_2^{\bullet-}$) is pivotal in driving the photocatalytic oxidation reaction.[178,179]

### 6.1.1. Photodegradation of dyes.

Water serves as the most critical resource for life, yet nearly 80% of the world's population now faces water supply and security issues due to rapid industrialization, urbanization, and lack of awareness.[180] Wastewater contaminated with dyes, mainly from industries like textiles, paper, food processing, paints, and cosmetics, is a major source of water pollution.[181] These dyes harm aquatic life with toxic effects and block sunlight, disrupting underwater ecosystems.[182] Azo dyes, commonly applied in textile production, carry severe toxic and carcinogenic risks for both humans and animals.[183] Consequently, it is crucial to eliminate dye residues because of their toxic nature and their significant harm to human health and environmental well-being. These residues can lead to serious health issues and disrupt ecosystems, making their removal a priority. For instance, ZnSe microspheres synthesized by Cao *et al.* *via* a surfactant-free solvothermal method using selenophene ($C_4H_4Se$) and $ZnCl_2$ were evaluated for the photocatalytic degradation of the azo dye MO under ultraviolet (UV) and visible light.[25] Fig. 15(a) and (b) illustrates the photoluminescence (PL) emission spectra for ZnSe microspheres and commercial ZnSe powder. The photocatalytic performance of the ZnSe microspheres was assessed by the degradation of MO dye in a $5 \times 10^{-5}$ M aqueous solution under UV light for varying time periods (Fig. 15(c) and (d)), with the degradation process monitored using MO's characteristic absorption at $\lambda = 462$ nm. Control analyses showed negligible degradation of MO without UV light or ZnSe microspheres. In a comparative study, the synthesized ZnSe microspheres achieved about 94% MO degradation after 7 hours, changing the color from orange to transparent, while commercial ZnSe powder required 10 hours to reach 95.1% degradation. These results indicated that ZnSe microspheres reveal intrinsic photocatalytic behaviour under UV light. On the other hand, the photocatalytic performance of the synthesized ZnSe microspheres and commercial powder were assessed for degrading MO dye under visible light (Fig. 15(e) and (f)). The ZnSe microspheres achieved around 94.3% MO degradation within 12 hours, while the commercial ZnSe powder reached approximately 60.6% degradation in the same period. When subjected to UV or visible light, the excitation of ZnSe microspheres and commercial powder generated conduction-band electrons and valence-band holes. The notable variations in photocatalytic behaviour between the synthesized ZnSe microspheres and commercial ZnSe powder were due to the greater number of available surface active sites in the microspheres and the larger surface area, which improved the electron–hole separation efficiency in the ZnSe microspheres.[25,184]

The mechanism of photodegradation of MO dye can be shown by the following equations:

The ZnSe microspheres absorb UV or visible light having energy $h\nu$ equal to or greater than the bandgap energy ($E_g$), producing electron ($e^-$) and hole ($h^+$) pairs.

$$2\text{ZnSe} + h\nu \rightarrow \text{ZnSe}(e^-) + \text{ZnSe}(h^+) \quad (19)$$

The absorbed $H_2O$ on the surface of ZnSe microspheres captures the holes, producing highly reactive hydroxyl radicals ($^{\bullet}OH$), as shown in eqn (20).

$$H_2O + \text{ZnSe}(h^+) \rightarrow {}^{\bullet}OH + H^+ + \text{ZnSe} \quad (20)$$

In this process, $O_2$ functions as an electron acceptor from the conduction band, resulting in the formation of a superoxide anion radical ($O_2^{\bullet-}$), which then reacts with protons to yield $^{\bullet}OOH$, as depicted in eqn (21) and (22).

$$O_2 + \text{ZnSe}(e^-) \rightarrow O_2^{\bullet-} + \text{ZnSe} \quad (21)$$

$$O_2^{\bullet-} + H^+ \rightarrow {}^{\bullet}OOH \quad (22)$$

The $^{\bullet}OH$ radical may also arise from the trapped electron ($e^-$) subsequent to the creation of the $^{\bullet}OOH$ radical, as outlined in eqn (23) and (24):

$$^{\bullet}OOH + H^+ + \text{ZnSe}(e^-) \rightarrow H_2O_2 + \text{ZnSe} \quad (23)$$

$$H_2O_2 + \text{ZnSe}(e^-) \rightarrow {}^{\bullet}OH + OH^- + \text{ZnSe} \quad (24)$$

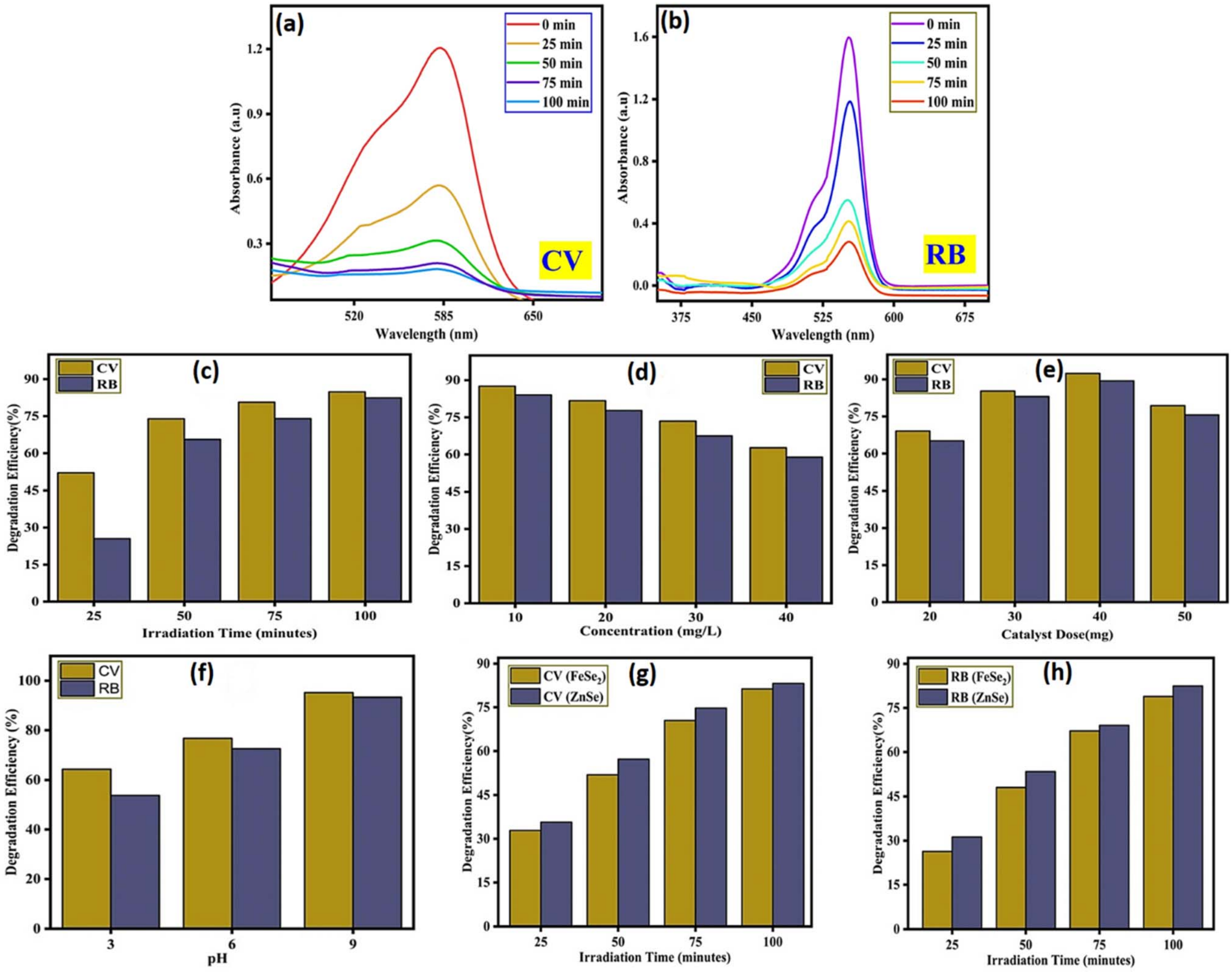

Fig. 16 Time-dependent UV-vis absorbance spectra of (a) CV, and (b) RB; effect of operational parameters on dye degradation using ZS/FS nanocomposite: (c) irradiation time, (d) initial dye concentration, (e) catalyst dose, and (f) solution pH; (g and h) comparison of degradation efficiencies of individual ZnSe (ZS) and $FeSe_2$ (FS) (reproduced from ref. 189). "This figure has been reproduced from ref. 189 with permission from Springer Nature, copyright 2024".

Table 3 Previously reported ZnSe-based photocatalysts for the photodegradation of organic contaminants

| Catalyst | Target contaminant | Source | Degradation efficiency, time | Ref. |
|---|---|---|---|---|
| ZnSe | MO | UV light | 94% in 7 h | 25 |
| ZnSe | AY 17 | UV light | 44% in 150 min | 190 |
| CuSe/ZnSe | MO | Visible light | 100% in 90 min | 191 |
| | MB | | 96% in 60 min | |
| ZnSe | MO | Visible light | 100% in 5 h | 192 |
| ZnSe/$TiO_2$ | MB | Visible light | 47% in 150 min | 193 |
| | MO | | 31% in 150 min | |
| | RhB | | 40% in 150 min | |
| ZnSe | MO | Simulated sunlight (100 mW $cm^{-2}$) | 96% in 9 h | 194 |
| Cu-doped ZnSe | MB | Visible light | 98.09% in 180 min | 195 |
| ZnTe/ZnSe | CR | UV-vis solar illumination | 94% in 65 min | 196 |
| ZnSe/rGO | MV | Visible light | 94% in 3 h | 197 |
| CS/ZnSe | Tartrazine | Sunlight | 98% in 3 h | 198 |
| | SY | | 97% in 3 h | |
| $CoNi_2O_4$/ZnSe | MB | Visible light | 92% in 2 h | 199 |
| $Fe_3O_4$/rGO/ZnSe/$TiO_2$ | MB | UV irradiation | 100% in 40 min | 200 |
| $ZnIn_2S_4$/ZnSe | TC | Visible light | 80% in 60 min | 201 |
| | OTC | | 74% in 60 min | |
| RGO–ZnSe | Norfloxacin | Simulated solar light | 83.5% in 40 min | 202 |
| ZnSe–Ag/g-$C_3N_4$ | Ceftriaxone sodium | Visible light | 89.24% in 90 min | 203 |
| $MoO_2$/ZnSe | Ciprofloxacin hydrochloride | Visible light | 80% in 180 min | 204 |
| $MoS_2$/ZnSe | Levofloxacin | Visible light | 73.2% in 2 h | 205 |
| ZnO/ZnSe/CdSe/$MoS_2$ | Amoxicillin | UV-visible | 100% in 30 min | 206 |

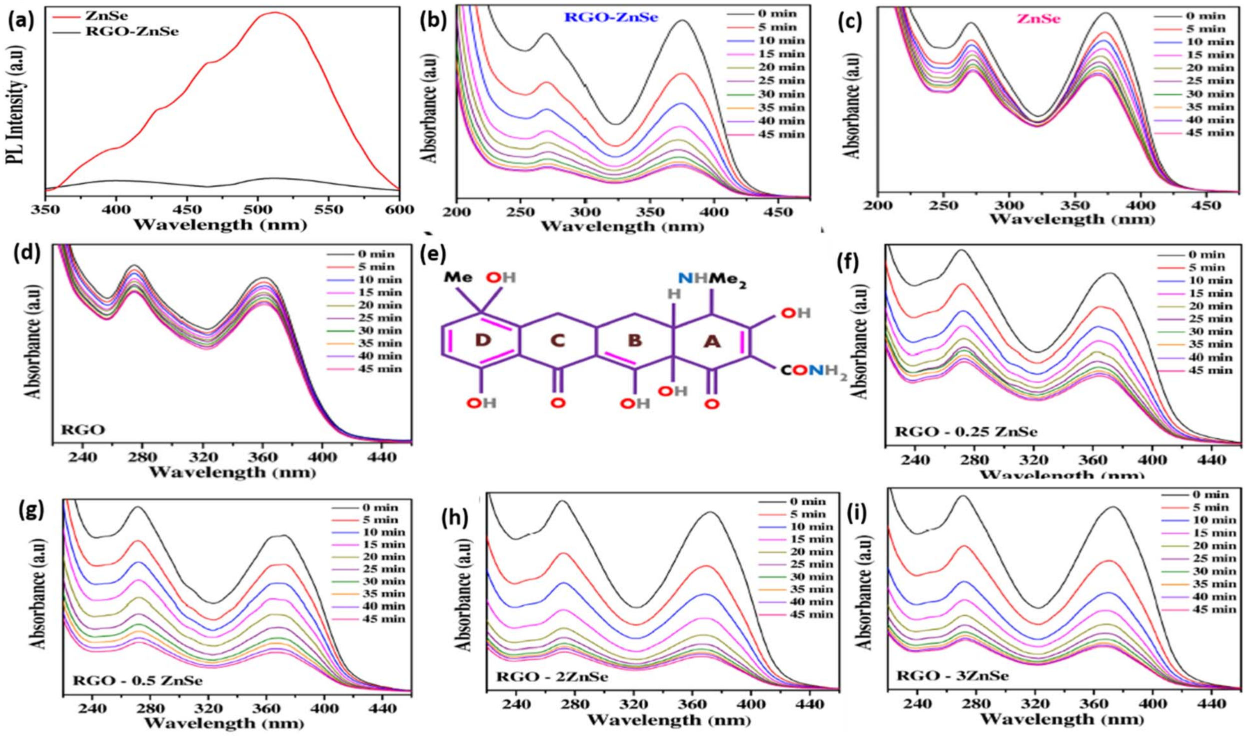

Fig. 17 (a) PL spectra of RGO–ZnSe and controlled ZnSe; UV-visible absorption spectra of an aqueous solution of tetracycline containing (b) RGO–ZnSe, (c) controlled-ZnSe, (d) controlled RGO; (e) structure of tetracycline; UV-visible absorption spectra of an aqueous solution of tetracycline containing (f) RGO–0.25 ZnSe, (g) RGO–0.5 ZnSe, (h) RGO–2 ZnSe, and (i) RGO–3ZnSe over distinct intervals of simulated solar light illumination (reproduced from ref. 212). "This figure has been reproduced from ref. 212 with permission from John Wiley and Sons, copyright 2018".

These radicals, including $^{\bullet}OH$ and $O_2^{\bullet-}$, possess exceptionally strong oxidizing capabilities, and can effectively degrade the MO dye.[185] Oxidative cleavage of azo dyes, including MO, is typically attributed to the subsequent attacks by $^{\bullet}OH$ radicals.[186] Following the addition of $^{\bullet}OH$ radicals to the aromatic group of MO, the carbon atom linked to the azo bond undergoes a transformation, resulting in the opening of the hydroxylated ring and ultimately producing $CO_2$ gas, $H_2O$, $SO_4^{2-}$, $NO_3^-$ and $NH_4^+$ through a series of oxidation steps, as illustrated below.[187]

$$\mathrm{MO} + {}^{\bullet}\mathrm{OH/O_2}^{\bullet-} \rightarrow (\text{intermediates}) \rightarrow \mathrm{CO_2} + \mathrm{H_2O} + \mathrm{SO_4}^{2-} + \mathrm{NO_3}^- + \mathrm{NH_4}^+ \quad (25)$$

The ZnSe/graphene nanocomposites, fabricated by Hsieh *et al.*, were assessed for the photocatalytic degradation of MB dye under visible-light irradiation achieving a degradation efficiency of 99.6% after 6 hours.[188] Recently, Bhat *et al.* synthesized a $ZnSe/FeSe_2$ (ZS/FS) heterostructure *via* a simple one-pot hydrothermal method and investigated its photocatalytic performance toward crystal violet (CV) and Rhodamine B (RB) under UV-visible light.[189] As shown in Fig. 16(a) and (b), the dye absorption intensity decreased with increasing irradiation time, achieving maximum degradation at 100 min-84.87% for CV and 82.43% for RB (Fig. 16(c)).

Fig. 16(d) shows that lower dye concentrations favoured degradation; for instance, 87.62% of 10 mg per L CV and 84.09% of 10 mg per L RB were degraded, while only 62.73% and 58.90% degradation were observed at 40 mg $L^{-1}$, respectively. Catalyst dose optimization indicated that 40 mg was the optimal amount, resulting in maximum degradation of 92.43% for CV and 89.39% for RB (Fig. 16(e)). Beyond this dose, efficiency declined due to increased turbidity and reduced photon absorption. Additionally, the effect of pH (3–9) on dye degradation was studied, with optimal performance observed at pH 9, where 95.23% of CV and 93.35% of RB were degraded (Fig. 16(f)). The enhancement at higher pH is attributed to increased $OH^-$ availability, promoting active radical generation. Comparative studies revealed that the ZS/FS heterostructure outperformed individual ZnSe and $FeSe_2$, which showed lower efficiencies-ZnSe: 83.19% (CV), 82.44% (RB); $FeSe_2$: 81.33% (CV), 78.89% (RB)-likely due to faster charge recombination in the pristine materials (Fig. 16(g and h)). Table 3 summarizes the photodegradation of various dyes using ZnSe based photocatalysts.

### 6.1.2. Photodegradation of antibiotics.

As chemotherapeutic agents, antibiotics act to inhibit and eliminate bacterial infections. Since Fleming's breakthrough discovery of penicillin in 1928, they have saved millions of lives.[207] Approximately 250 different antibiotics are utilized in both human and veterinary medicine.[208] However, improper antibiotic use has led to their continuous release into the water from industries, households, farms, and fisheries, making them significant emerging contaminants (ECs). Their complex structures, like β-lactam rings, tetracyclic nuclei, and lactone rings, give them long half-lives and resist microbial degradation, posing health risks. For instance, sulfadiazine, ofloxacin, tetracycline, and erythromycin have half-lives of 25.7, 11.1, 4.15, and 4.22 days, respectively.[209] This means antibiotics can travel long distances in rivers before their concentration decreases by half. Ongoing releases have lasting ecotoxic effects on wildlife, promote antibiotic-resistant genes (ARG) and bacteria (ARB), and can disrupt fish reproduction. Consequently, it is urgent to remove antibiotics from water sources.[210,211] For instance, RGO–ZnSe nanocomposites were fabricated *via* a one-step solvothermal reaction, evaluating their photocatalytic performance for tetracycline (TC) degradation under simulated solar light irradiation.[212] The PL spectra of ZnSe and RGO–ZnSe nanocomposite, excited at 300 nm, reveal a significant quenching effect due to robust interfacial interactions between ZnSe and RGO at ambient temperature (Fig. 17(a)). This pronounced reduction in PL intensity highlights an efficient charge transfer process, making RGO–ZnSe a compelling candidate for advanced photocatalytic applications. The photocatalytic behaviour was assessed with a UV-vis spectrophotometer. Fig. 17(b) shows the UV-vis absorption spectra of TC solution degraded by RGO–ZnSe for 0–45 min at 5-min intervals. Comparable data for controlled ZnSe and RGO photocatalysts are shown in Fig. 17(c) and (d), with the TC structure depicted in Fig. 17(e). The effectiveness of the RGO–ZnSe composite in photodegrading aqueous TC solutions was tested at varying ZnSe to RGO ratios (RGO0.25ZnSe, RGO–0.50ZnSe, RGO–2ZnSe, RGO–3ZnSe under uniform experimental conditions, with the UV-vis spectra presented in Fig. 17(f–i). The degradation efficacy of all the fabricated RGO–ZnSe composites is illustrated in Fig. 18, with the RGO–ZnSe demonstrating the highest photocatalytic behaviour, outperforming RGO and all other tested ratios, including controlled-ZnSe.

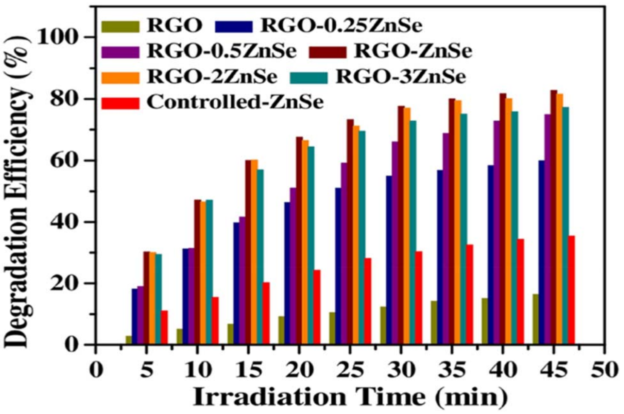

Fig. 18 Comparison of the degradation efficiency of all the fabricated RGO–ZnSe composites with varying ZnSe to RGO ratios (reproduced from ref. 212). "reproduced from ref. 212 with permission from [John Wiley and Sons], copyright [2018]".

The mechanism of the degradation of TC is explained below (eqn (26)–(33)):[212]

$$\mathrm{ZnSe} + h\nu \rightarrow \mathrm{ZnSe(e^- + h^+)} \quad (26)$$

$$\mathrm{RGO - ZnSe(e^-)} \rightarrow \mathrm{RGO(e^-)} + \mathrm{ZnSe(h^+)} \quad (27)$$

$$\mathrm{RGO(e^-)} + \mathrm{O_2} \rightarrow \mathrm{O_2}^{\bullet-} \quad (28)$$

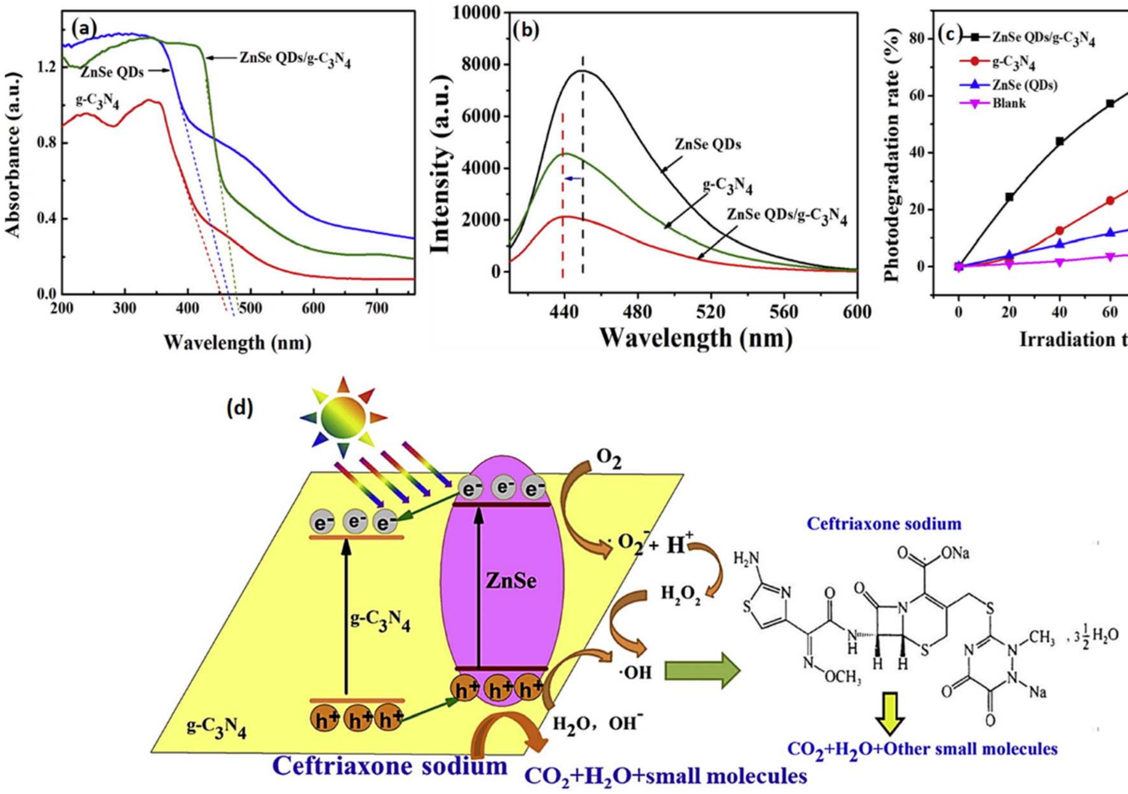

Fig. 19 (a) UV-vis diffused absorption spectra, (b) photoluminescence spectra, (c) photocatalytic performance; (d) possible degradation mechanism of ceftriaxone sodium using ZnSe QDs/g-$C_3N_4$ composite (reproduced from ref. 213). "This figure has been reproduced from ref. 213 with permission from Elsevier, copyright 2018".

$$RGO(e^-) + O_2^{\cdot -} + H^+ \rightarrow HO_2^- \quad (29)$$

$$HO_2^- + H^+ \rightarrow H_2O_2 \quad (30)$$

$$H_2O_2 + e^- \rightarrow {}^{\cdot}OH + OH^- \quad (31)$$

$$H_2O + ZnSe(h^+) \rightarrow {}^{\cdot}OH + H^+ + ZnSe \quad (32)$$

$$^{\cdot}OH/h^+/O_2^{\cdot -}/e^- + TC \rightarrow \text{degraded product} \quad (33)$$

Under the influence of visible light, excitons formed in ZnSe dissociate into electrons ($e^-$) and holes ($h^+$). Without RGO, most of these charges quickly recombined, limiting reactivity. However, the close contact between ZnSe NPs and RGO enabled the transfer of excited electrons to RGO, enhancing charge separation and reducing recombination. This process also led to the formation of hydroxyl radicals ($^{\cdot}OH$) from photoexcited holes in the valence band. The excited electrons moved freely along the conductive network of RGO. When $O_2$ was adsorbed onto the RGO surfaces, the electrons reacted with $O_2$, resulting in the formation of superoxide anion radical ($^{\cdot}O_2^-$). The TC molecules can be broken down into degradation products by the highly reactive species $^{\cdot}OH$, $h^+$, $^{\cdot}O_2^-$, and $e^-$, due to their strong reactivity.

Similarly, Zhao *et al.* synthesized a ZnSe QDs/g-$C_3N_4$ composite and investigated its photocatalytic efficiency for degrading Ceftriaxone sodium in water under visible light.[213] The DRS absorption edges of pure g-$C_3N_4$ and ZnSe QDs were observed at 454 nm and 466 nm, respectively, while the ZnSe QDs/g-$C_3N_4$ composite exhibited a red-shifted absorption at 475 nm, indicating improved visible light harvesting characteristics (Fig. 19(a)). Moreover, the composite showed the lowest photoluminescence intensity among all samples, suggesting superior charge carrier separation and enhanced photocatalytic performance (Fig. 19(b)). The ZnSe QDs/g-$C_3N_4$ composite exhibited a significantly higher degradation rate of ceftriaxone sodium compared to pure g-$C_3N_4$ and ZnSe QDs, confirming its superior photocatalytic activity (Fig. 19(c)). The proposed mechanism for the degradation of ceftriaxone sodium using the ZnSe QDs/g-$C_3N_4$ composite is illustrated in Fig. 19(d). Under visible light irradiation, photogenerated electrons ($e^-$) in the conduction band (CB) of ZnSe QDs transfer to the CB of g-$C_3N_4$, while holes ($h^+$) are excited from the valence band (VB) of g-$C_3N_4$ to the VB of ZnSe QDs. In this heterojunction, g-$C_3N_4$ serves as an electron acceptor, effectively suppressing the recombination of photogenerated $e^-/h^+$ pairs. The transferred electrons react with $O_2$ to form $^{\cdot}O_2^-$ radicals which further interact with $H^+$ to generate additional $^{\cdot}O_2^-$.Concurrently, the holes accumulated in the VB of ZnSe QDs oxidize $H_2O$ and $OH^-$ to produce $^{\cdot}OH$ radicals. These reactive species synergistically degrade Ceftriaxone sodium into $CO_2$, $H_2O$, and other smaller molecules. The proposed degradation pathway is as follows (eqn (34)–(37)):[213]

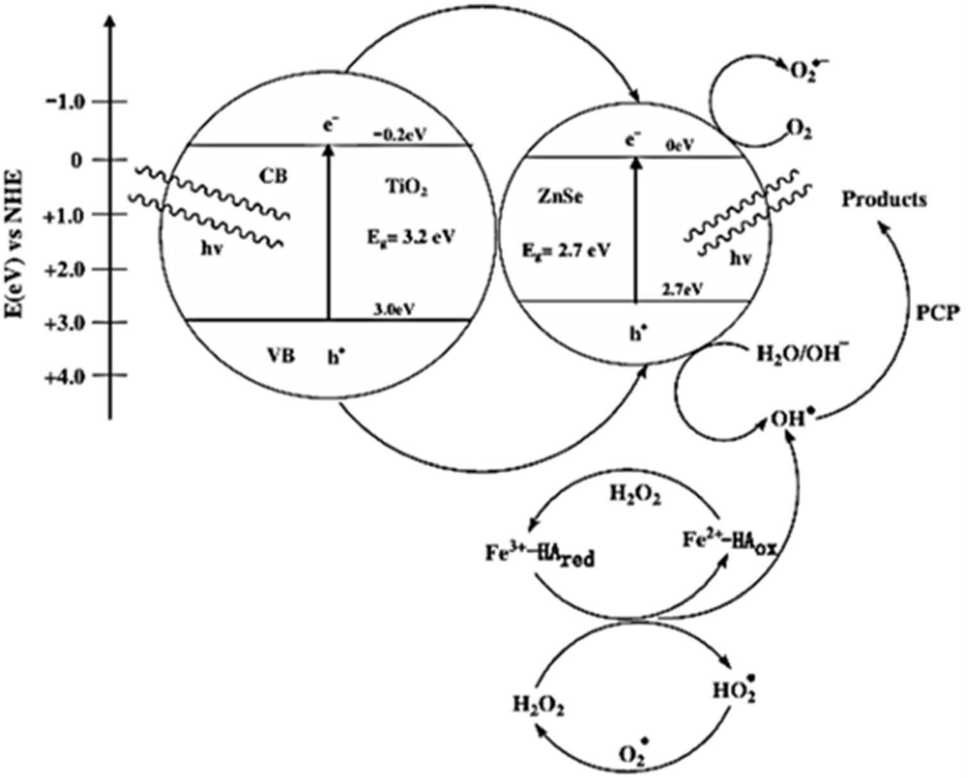

Fig. 20 Illustration of electron and hole transfer in the ZnSe sensitized $TiO_2$ NTAs and mechanism of photocatalysis degradation with support of the photo-Fenton system (reproduced from ref. 121). "This figure has been reproduced from ref. 121 with permission from Elsevier, copyright 2013".

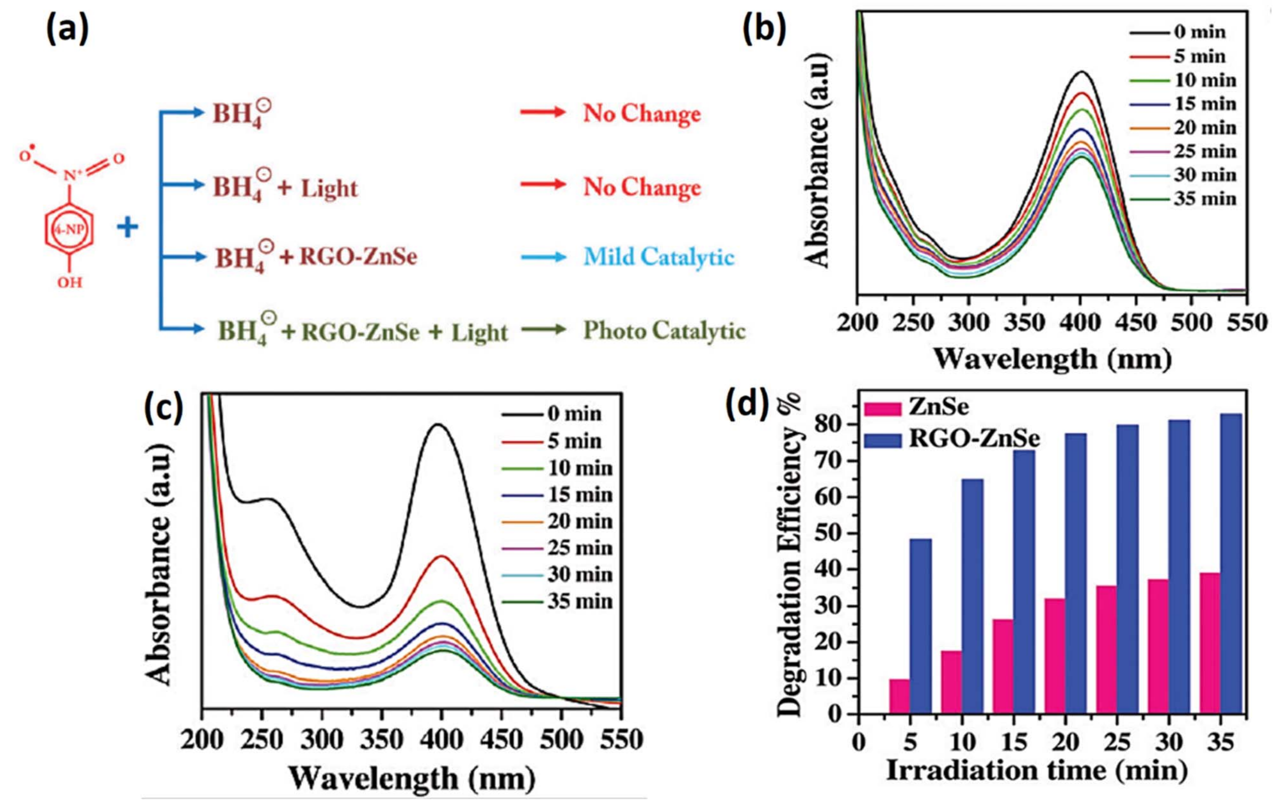

Fig. 21 (a) Schematic presentation of different reaction conditions for the possible reduction of 4-NP. UV-vis absorption spectra of 4-NP and $NaBH_4$ aqueous with (b) controlled ZnSe and (c) RGO–ZnSe composite for varying times of simulated solar light illumination, (d) comparison of photodegradation efficiency as a function of time for controlled ZnSe and the RGO–ZnSe composite (reproduced from ref. 219).

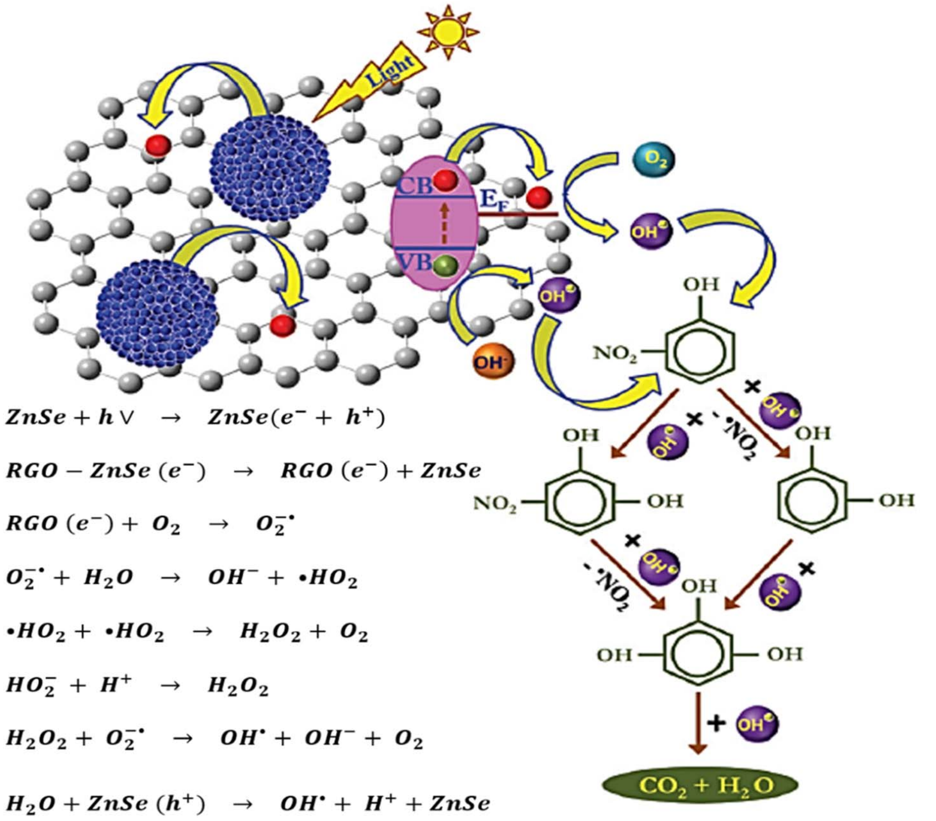

Fig. 22 Mechanism of photocatalytic 4-NP degradation using RGO–ZnSe composite (reproduced from ref. 219).

$$\text{ZnSe QDs/g-C}_3\text{N}_4 \xrightarrow{h\nu} \text{h}^+ + \text{e}^- \tag{34}$$

$$\text{h}^+ + \text{H}_2\text{O} \rightarrow \text{h}^+ + {}^{\bullet}\text{OH} \tag{35}$$

$$\text{e}^- + \text{O}_2 + \text{h}^+ \rightarrow {}^{\bullet}\text{OH} \tag{36}$$

$$\text{h}^+ + {}^{\bullet}\text{OH} + \text{ceftriaxone sodium} \rightarrow \text{CO}_2 + \text{H}_2\text{O} + \text{other small molecules} \tag{37}$$

Recently, Liu *et al.* synthesized a novel 3D/3D S-scheme ZnSe/$NiMoO_4$ heterostructure *via* a hydrothermal method, with 15% ZnSe identified as the optimal composition.[214] The photocatalytic performance was evaluated against tetracycline under visible light irradiation using a 300 W Xe lamp equipped with a UV cut-off filter ($\lambda < 400$ nm). $NiMoO_4$ exhibited the lowest activity, attributed to its weak absorption in the visible region and fast recombination of photogenerated charge carriers. Notably, all ZnSe/$NiMoO_4$ composites showed a substantial improvement in photocatalytic activity, with the 15% ZnSe/$NiMoO_4$ sample delivering the highest degradation efficiency under the same experimental conditions. The progressive decline in the absorption peaks at 357 and 275 nm, along with noticeable peak shifts, suggests the gradual degradation of tetracycline, involving the breakdown of aromatic structures and formation of intermediate compounds. Table 3 summarizes the previously reported ZnSe-based photocatalysts utilized for the photodegradation of various antibiotics.

**6.1.3. Photodegradation of phenolic compounds.** Among the diverse array of contaminants, the widespread presence of phenolic compounds in wastewater and their associated environmental risks have raised serious public health concerns.[215] Phenols and their derivatives are recognized for their strong resistance to biodegradation and high toxicity. These compounds are continuously released into aquatic systems through numerous human activities. Furthermore, the structural diversity, high toxicity, and environmental persistence of these compounds can severely impact ecosystem integrity and endanger human health through the contamination of surface and groundwater sources. As a result, the efficient removal of phenolic compounds from wastewater effluents has emerged as a significant challenge, essential for mitigating pollution risks and promoting the safe reuse of treated water.[216] The photocatalytic performance of the $WO_3$–ZnSe nanostructures was evaluated through the degradation of phenol under UV-visible light irradiation, with nearly 93% degradation achieved within 105 min.[217] The degradation mechanism can be described in two main steps: initially, highly reactive species such as free radicals are generated. In the second step, these radicals oxidize the phenol molecules adsorbed on the catalyst surface. The catalyst, surrounded by hydroxyl groups, becomes negatively charged when dispersed in the phenol solution. Due to electrostatic interaction, phenol-being weakly acidic, is readily

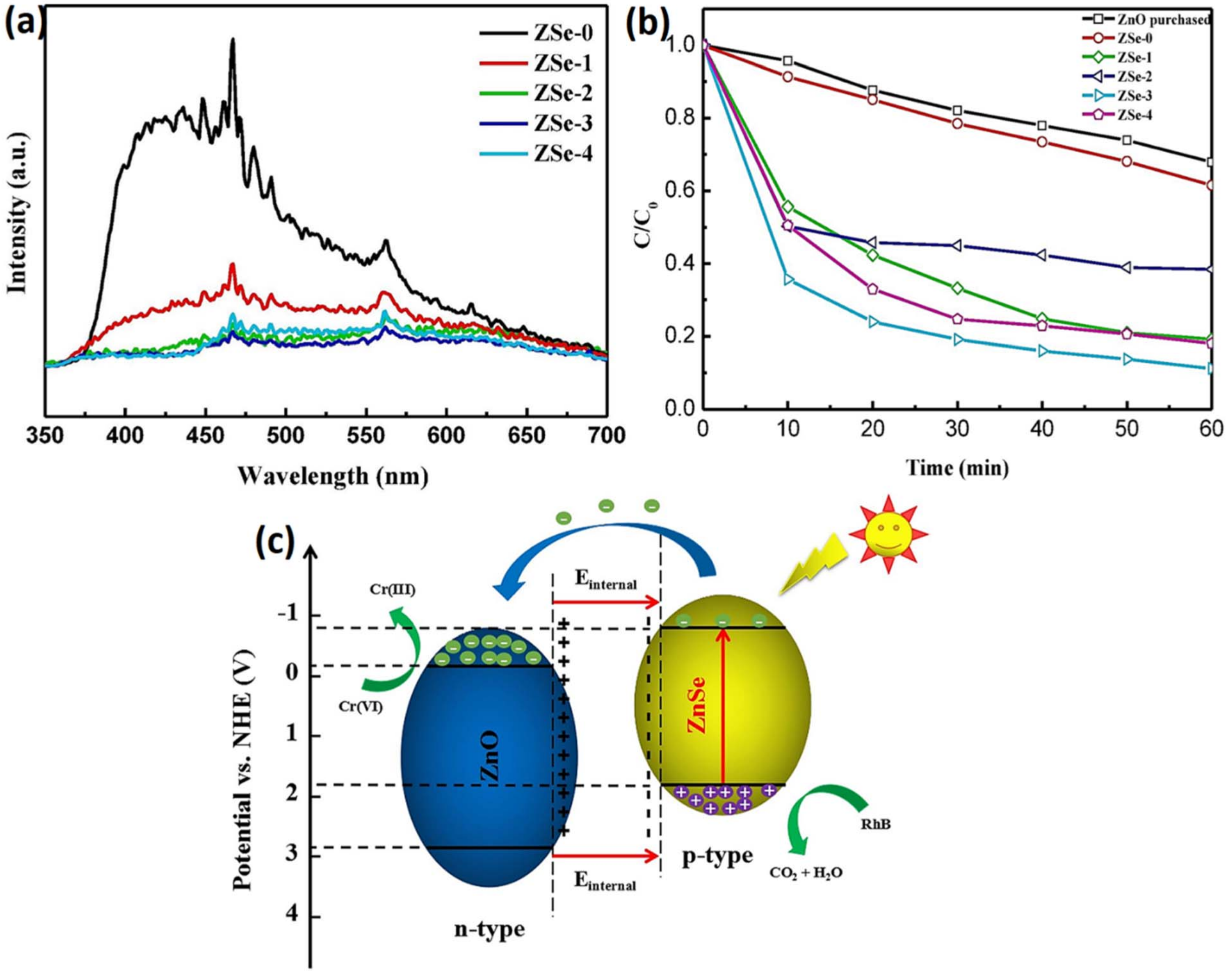

Fig. 23 (a) PL spectra of pure ZnO and ZnO/ZnSe composites at room temperature under 325 nm excitation, (b) time-dependent changes in $C/C_0$ of Cr(VI) using different photocatalysts under visible light exposure, and (c) proposed photocatalytic degradation pathways of Cr(VI) using ZnO/ZnSe composite (reproduced from ref. 225). "This figure has been reproduced from ref. 225 with permission from Elsevier, copyright 2021".

adsorbed onto the catalyst surface. Upon exposure to light, photons with energy equal to or greater than the bandgap excite the catalyst, resulting in the formation of electron–hole pairs. The excited electrons migrate to the CB, while holes remain in the VB. The holes oxidize the adsorbed hydroxyl groups, forming highly reactive $^{\bullet}OH$ radicals. Simultaneously, the CB electrons reduce molecular oxygen to $^{\bullet}O_2^-$ radicals, which further interact with water to produce $H_2O_2$. However, Kumar *et al.* previously reported a ZnSe–$WO_3$ nano-hetero-assembly supported by Gum ghatti for the effective photodegradation of a phenolic derivative, bisphenol A (BPA).[218] The designed Z-scheme photocatalyst exhibited superior visible light absorption and efficient charge separation, with gum ghatti serving as both a super-adsorbent and a charge carrier reservoir. BPA degradation was investigated under three different experimental conditions, achieving an impressive 99.5% degradation within just 45 minutes through the synergistic action of photocatalysis, adsorption, and ozonation. This nano-hetero-assembly demonstrated high surface area, excellent stability, and minimized charge carrier recombination.

In a related study, ThanhThuy *et al.* synthesized a ZnSe/$TiO_2$ nanotube array (NTAs) photocatalyst *via* pulse electrodeposition of ZnSe nanoparticles onto $TiO_2$ NTAs and demonstrated its application in the photo-Fenton-assisted degradation of pentachlorophenol (PCP).[121] The enhanced degradation is attributed to the HA-mediated photosensitized generation of $H_2O_2$ and $^{\bullet}O_2^-$ radicals under AM 1.5G illumination. After 80 min of irradiation, PCP removal efficiencies were recorded at 93.2%, 68.9%, and 60.2% for $H_2O_2$ concentrations of 150 μM, 75 μM, and 40 μM, respectively. Extending the irradiation time to 2 hours improved the degradation to 99% and 79.9% for $H_2O_2$ concentrations of 75 μM and 40 μM, respectively. These findings confirm the critical role of $H_2O_2$ in generating $^{\bullet}OH$ radicals, which significantly enhance the oxidative degradation of PCP in the ZnSe/$TiO_2$ photocatalytic system. The decline in efficiency at higher initial concentrations of PCP is attributed to increased optical density, which limits light penetration and photon absorption at the catalyst surface. Additionally, elevated PCP levels reduce the availability of active sites due to competitive adsorption, thereby diminishing the generation of $^{\bullet}OH$ radicals and other reactive species essential for effective degradation. Furthermore, Fig. 20 illustrates the proposed mechanism of charge transfer in the ZnSe-sensitized $TiO_2$ NTAs, highlighting the photocatalytic degradation pathway facilitated by the synergistic action of the photo-Fenton process.

Similarly, ZnSe-decorated RGO was utilized in the photocatalytic degradation of 4-nitrophenol (4-NP) (Fig. 21(a)).[219] While a progressive decline in the 4-NP absorption peak was observed in the UV-vis absorbance spectra with increasing irradiation time, the absence of a characteristic aminophenol peak (∼295 nm) confirms that the degradation proceeds *via* an oxidative rather than a reductive pathway for both catalysts (Fig. 21(b) and (c)). Notably, the RGO–ZnSe composite achieved approximately 85% degradation of 4-NP within 35 min, significantly outperforming the pristine ZnSe (35%) and RGO (24%) under identical conditions (Fig. 21(d)). Upon illumination, both ZnSe and RGO components in the composite generate excitons. These excitons in ZnSe undergo diffusion and separation at the RGO/ZnSe interface, where efficient electron transfer from ZnSe to RGO occurs, leaving behind holes in the semiconductor matrix. The spatially separated electron–hole pairs in the RGO–ZnSe system effectively initiate the formation of $^{\bullet}OH$ radicals, which are pivotal in driving the photocatalytic degradation process. A comprehensive schematic representation of the $^{\bullet}OH$ generation pathway and the proposed mechanism underpinning the elevated activity of the RGO–ZnSe composite is presented in Fig. 22.

### 6.2. Removal of Cr(VI) from aqueous medium

With rapid global industrialization, environmental issues have become more severe, with heavy metal pollutants such as Pb, Cd, Cr, As, and Hg posing significant threats to human health.[220] Among these, hexavalent chromium [Cr(VI)] is especially toxic, known for its carcinogenic, mutagenic, and irreversible harmful effects on living organisms. Consequently, the reduction of Cr(VI) to the less toxic and more stable trivalent chromium [Cr(III)] has garnered significant attention.[221] Therefore, developing an economical, sustainable, and highly

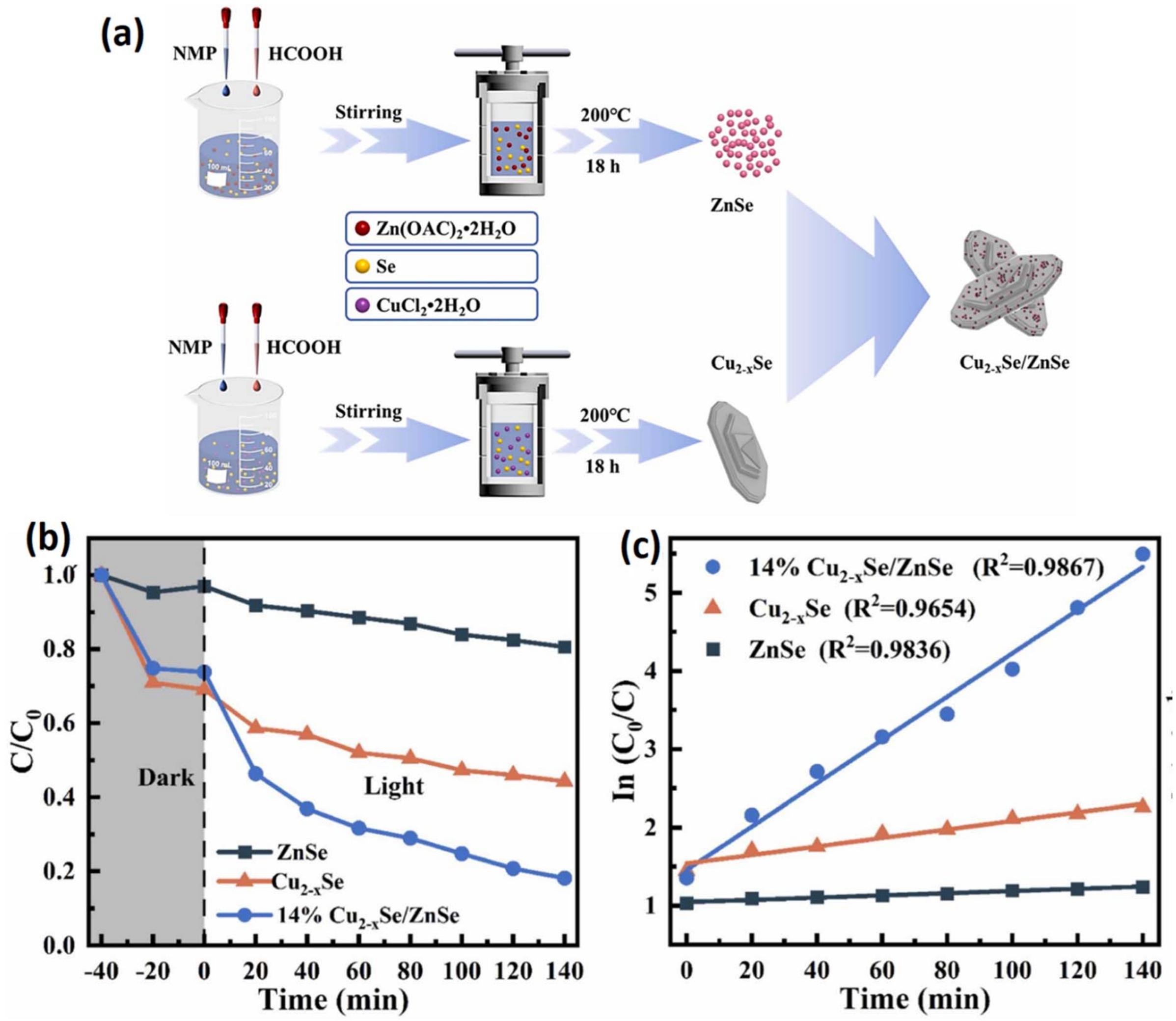

Fig. 24 (a) Synthetic scheme of $Cu_{2-x}Se$/ZnSe composite; photocatalytic Cr(VI) reduction studies: (b) comparison of activities of individual materials and 14% $Cu_{2-x}Se$/ZnSe composite, and (c) kinetic analysis (reproduced from ref. 226). "This figure has been reproduced from ref. 226 with permission from Elsevier, copyright 2025".

Table 4 Summary of Cr(VI) photoreduction using ZnSe-based materials

| Catalyst | Synthetic method | Source | Efficiency | Ref. |
|---|---|---|---|---|
| $MoSe_2/ZnO/ZnSe$ | Hydrothermal | Visible light | 100% | 227 |
| ZnO/ZnSe | Two-step hydrothermal and ion-exchange | Visible light | 88.8% | 225 |
| 14% $Cu_{2-x}Se/ZnSe$ | Solvothermal | — | 82% | 226 |
| $ZnS/ZnSe/MoSe_2$ | Solvothermal and ion-exchange | Visible light | 96% | 221 |
| 3% $ZnSe/TiO_2$ | Solution-based synthesis | Visible light | 83% | 222 |

efficient method for Cr(VI) removal from wastewater is of utmost importance. Photocatalysis has recently emerged as an effective and environmentally friendly approach for reducing highly toxic Cr(VI) ions to the less toxic Cr(III), and further to insoluble $Cr(OH)_3$, through photoinduced electrons in the CB. Among various semiconductor materials, transition metal chalcogenides have gained attention due to their abundance and suitable band gaps, enabling efficient visible-light-driven photocatalysis.[222] Notably, ZnSe exhibits excellent physicochemical properties that are highly dependent on its particle size, morphology, and synthesis method.[223,224] Zhang *et al.* successfully synthesized a ZnSe/ZnO p–n heterojunction *via* a combination of hydrothermal and ion exchange methods, significantly enhancing the photocatalytic reduction of Cr(VI).[225] PL analysis revealed that the ZSe-3 composite exhibited the lowest PL intensity, indicating superior charge carrier separation compared to pure ZnO, which showed the highest PL intensity (350–700 nm) (Fig. 23(a)).

As shown in Fig. 23(b), ZSe-3 demonstrated the highest photocatalytic activity, achieving 88.8% Cr(VI) reduction within 60 min, outperforming ZSe-1 and ZSe-2. In contrast, bare ZnO and commercial ZnO showed significantly lower efficiencies, with Cr(VI) reduction rates of only 38.5% and 32.1%, respectively. The enhanced performance of the ZnSe/ZnO nanocomposite is attributed to the favourable band alignment between ZnSe and ZnO. Upon visible-light irradiation, electrons in the CB of ZnSe, which possesses a more negative potential than ZnO, transfer to the CB of ZnO, while $h^+$ migrate from the VB of ZnO to that of ZnSe. This effective charge separation facilitates the reduction of Cr(VI) to Cr(III), as supported by the CB potential of ZnO being sufficiently negative (Fig. 23(c)).

In a recent study, Yu *et al.* fabricated a novel p–n heterojunction photocatalyst by integrating ZnSe nanoparticles onto $Cu_{2-x}Se$ nanoplates, effectively generating a built-in electric field that promotes rapid charge carrier separation and minimizes recombination (Fig. 24(a)).[226] This synergistic interaction significantly enhanced the photocatalytic performance, with the 14% $Cu_{2-x}Se/ZnSe$ composite exhibiting superior activity compared to other formulations. Under identical conditions, the individual components ZnSe and $Cu_{2-x}Se$ displayed relatively low Cr(VI) removal efficiencies of 19% and 56%, respectively, after 140 min of irradiation. Notably, the 14% $Cu_{2-x}Se/ZnSe$ heterostructure exhibited a marked enhancement in photocatalytic activity, reaching a Cr(VI) reduction efficiency of 82% under identical experimental conditions (Fig. 24(b) and (c)). Further, Qiu *et al.* successfully fabricated $ZnS/ZnSe/MoSe_2$ (ZZM) nanocomposites incorporating dual type-II heterojunctions through a combination of solvothermal synthesis and ion exchange techniques, for the first time.[221] The Cr(VI) reduction performance of the ZZM photocatalysts was assessed under visible light illumination, achieving a Cr(VI) removal rate of 96%. The improved photocatalytic activity can be assigned to the dual heterostructures, which effectively promoted the separation and migration of photogenerated charge carriers. Meanwhile, the extended light response range and the increased specific surface area also contribute to the improvement of the photocatalytic efficiency. A comparative overview of Cr(VI) photoreduction using various ZnSe-based photocatalysts is presented in Table 4.

### 6.3. Reduction of $CO_2$

As modern lifestyles progress, energy consumption is expected to reach 25–27 TW, surpassing 80% of available fossil fuel reserves. This heavy reliance will deplete resources and emit large amounts of $CO_2$, disrupting ecological carbon balance.[228] The increasing emissions are causing severe environmental issues, like melting polar ice caps and rising sea levels. To counter this, researchers are working on capturing and converting $CO_2$ into useful fuels. Carbon capture and storage (CCS) methods offer a promising solution, including the catalytic hydrogenation of $CO_2$ into compounds like formate/formic acid, methanol or dimethyl ether.[229] While significant efforts have gone into developing heterogeneous electrocatalysts to valorize $CO_2$, achieving efficient and selective electroreduction remains challenging due to high overpotentials and the formation of multiple intermediates.[230] In contrast, photoreduction processes present a promising alternative for improving selectivity and efficiency. Extensive research on photocatalysts has led to advanced strategies for $CO_2$ photoreduction, with early studies using $TiO_2$ semiconductors in aqueous suspension successfully producing formaldehyde, formic acid, methanol, and methane.[231]

Various materials have been explored for $CO_2$ photoreduction, with numerous novel materials being thoroughly investigated.[41–43] Among these, zinc chalcogenide-based catalysts stand out as promising candidates for $CO_2$ photoreduction. Zinc chalcogenides, particularly ZnSe, are promising for $CO_2$ photoreduction due to their visible-light responsiveness, with bandgaps of 2.7 eV.[44] Unlike ZnO and ZnS, which require UV light, these materials have conduction band potentials negative enough to reduce $CO_2$ efficiently, matching the redox potentials of typical $CO_2$ reduction products (−0.24 to −0.61 V *vs.* NHE).[232] Although ZnSe

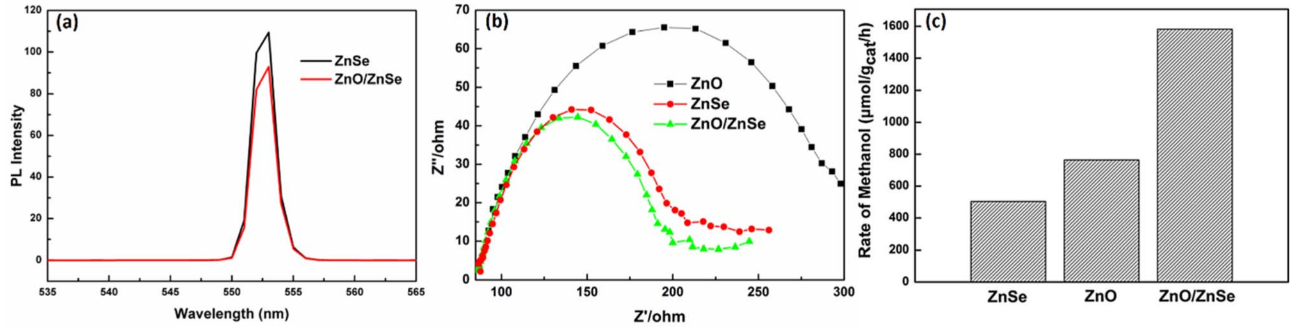

Fig. 25 (a) The PL spectra for both pure ZnSe and the 3 wt% ZnO/ZnSe composite, (b) EIS analysis of ZnO, ZnSe, and 3 wt% ZnO/ZnSe composite electrodes, and (c) the photocatalytic reduction of $CO_2$ to methanol using pure ZnO, ZnSe, and 3 wt% ZnO/ZnSe composite materials (reproduced from ref. 233). "This figure has been reproduced from ref. 233 with permission from Elsevier, copyright 2018".

demonstrates promising potential for $CO_2$ photocatalytic reduction, its overall photocatalytic efficiency remains low because of rapid electron–hole recombination. This recombination process limits the availability of charge carriers needed for effective $CO_2$ reduction, thereby hindering performance. To overcome this limitation and enhance its photocatalytic activity, modifications to the pure ZnSe structure are essential, such as preparation of heterojunction, defects, and morphology, allowing for modulation of their photocatalytic performance.[129,233] For instance, in 2018, Zhang *et al.* synthesized ZnO/ZnSe composites *via* a solvothermal technique, enabling the photocatalytic reduction of $CO_2$ into methanol.[233] The PL spectra showed that the 3 wt% ZnO/ZnSe composite has the highest electron–hole separation efficiency, suppressing recombination and maximizing methanol production (Fig. 25(a)). The EIS Nyquist plot in Fig. 25(b), with its smallest arc size for the 3 wt% ZnO/ZnSe composite, confirms enhanced charge separation and electron transport, supporting the PL results. As depicted in Fig. 25(c), the 3 wt% ZnO/ZnSe nanohybrid demonstrated a $CO_2$ reduction rate to methanol of 1581.82 $\mu mol\ g_{cat}{}^{-1}\ h^{-1}$, which is notably higher than the 503.88 $\mu mol\ g_{cat}{}^{-1}\ h^{-1}$ and

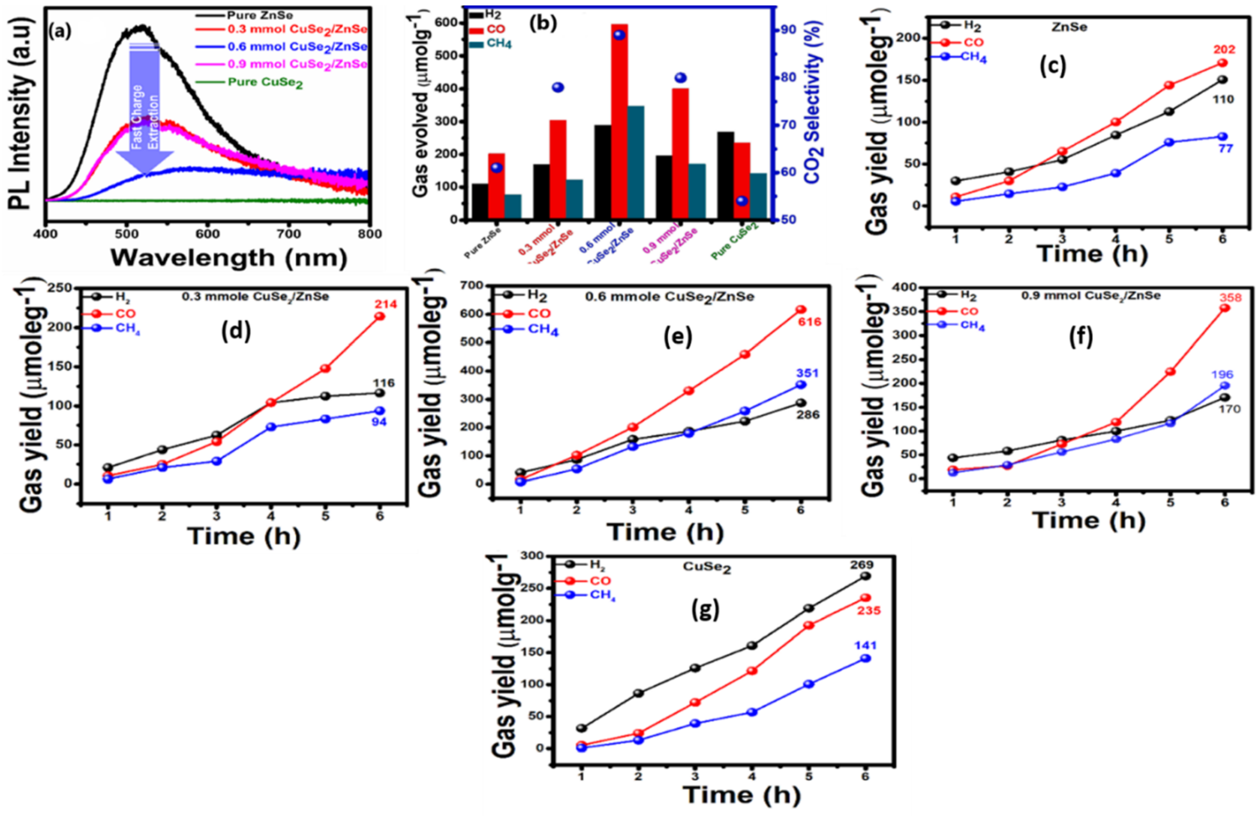

Fig. 26 (a) PL spectra, and (b) $CO_2$ photoreduction activities of pure ZnSe, 0.3 mmol $CuSe_2$/ZnSe, 0.6 mmol $CuSe_2$/ZnSe, 0.9 mmol $CuSe_2$/ZnSe, and pure $CuSe_2$; photoreduction of $CO_2$ by (c) pure $ZnSe_2$, (d) 0.3 mmol $CuSe_2$/ZnSe, (e) 0.6 mmol $CuSe_2$/ZnSe, (f) 0.9 mmol $CuSe_2$/ZnSe, and (g) pure $CuSe_2$ (reproduced from ref. 234). "This figure has been reproduced from ref. 234 with permission from Elsevier, copyright 2024".

763.9 μmol $g_{cat}^{-1}$ $h^{-1}$ observed for pristine ZnSe and ZnO, respectively.

Recently, Z-scheme $CuSe_2$/ZnSe heterostructures were synthesized through a straightforward hydrothermal approach for the reduction of $CO_2$ photocatalytically under UV-visible light exposure, using different concentrations of copper(II) acetate hydrate (0.30 mmol, 0.6 mmol, and 0.9 mmol).[234] The PL spectra, portrayed in Fig. 26(a), shows that all the composite photocatalysts exhibit reduced emission intensities than the pure ZnSe. The 0.6 mmol $CuSe_2$/ZnSe photocatalyst exhibits the weakest intensity, indicating an elevated minimization in charge recombination rate and enhanced charge separation. Pure $CuSe_2$, however, shows no photoemission, likely due to minimal charge carrier generation.

Fig. 26(b) shows the $CO_2$ photoreduction activities of the prepared photocatalysts. Pure ZnSe produced 202 μmol per g CO, 77 μmol per g $CH_4$, and 110 μmol per g $H_2$. Incorporating $CuSe_2$ as a co-catalyst significantly enhanced the activity, with the 0.6 mmol $CuSe_2$/ZnSe heterostructure showing the best photocatalytic efficiency. As shown in Fig. 26(e), the photocatalytic yields of CO, $CH_4$, and $H_2$ for 0.6 mmol $CuSe_2$/ZnSe reached 616, 351, and 286 μmol $g^{-1}$ after 6 hours of irradiation. These values surpass those of pure ZnSe, 0.3 mmol $CuSe_2$/ZnSe, 0.9 mmol $CuSe_2$/ZnSe, and $CuSe_2$, as shown in Fig. 26(c–g).[234]

### 6.4. Gas sensing with ZnSe-based sensors

Monitoring hazardous gases is vital not only for environmental protection but also for industrial safety and regulatory compliance. Recent advances in gas sensor technology have focused on detecting harmful species such as CO, $NO_2$, and $NH_3$ which are widely emitted from vehicles, factories, and household materials.

$NO_2$ is a prominent air pollutant generated from common combustion processes, including vehicular exhaust, industrial operations, and domestic heating systems. Its detrimental impact on environmental and human health has intensified the need for efficient detection technologies.[235] In this context, chemiresistive sensors have been extensively investigated to meet this need, with research focusing on optimizing their response characteristics, including enhanced selectivity, faster response times, and improved operational stability. These developments are essential to creating more effective tools for monitoring air quality.[236] Despite these advancements, studies on ZnSe-based sensors remain limited. Moreover, the majority of reported ZnSe gas sensors require elevated operating temperatures, which restricts their use in low-energy applications. The performance of ZnSe nanowires in detecting $NO_2$ were assessed using interconnected networked ZnSe nanowire sensor system.[237] The study revealed that ZnSe could serve as an effective sensing material at room temperature. When exposed to $NO_2$ concentrations from 50 ppb to 5 ppm, the sensor demonstrated response rates of 101–102% in dark conditions and significantly higher responses of 113–234% under UV light. The response of ZnSe nanowires to 5 ppm $NO_2$ significantly increased from 102% to 234% as the intensity of UV illumination rose from 0 to 1.2 mW $cm^{-2}$. Notably, the sensing performance of ZnSe nanowires was either surpassed or matched that of traditional metal oxide semiconductors, which typically require elevated $NO_2$ concentrations and higher operating temperatures to achieve similar results. Liu *et al.* reported that a mesoporous ZnSe/ZnO heterojunction-based sensor exhibited a significantly enhanced response, about 7.3 times greater than that of pristine ZnO and ZnSe sensors, when detecting 8 ppm of $NO_2$ at 200 °C.[39] The enhanced selectivity of the sensor toward $NO_2$ can be primarily ascribed to its strong molecular polarity, which facilitates more favourable interactions at the heterojunction interface compared to less polar VOCs. Furthermore, the operation at a moderate temperature of 200 °C favours the presence of less reactive chemisorbed $O^-$ species, which are less likely to interact with VOCs. This contrasts with conventional ZnO-based sensors operated at over 300 °C, where more reactive $O^{2-}$ species dominate the surface, increasing cross-sensitivity to various gases and reducing selectivity. In another study, Liu *et al.* developed a ZnSe/$SnO_2$-based sensor that effectively detected $NO_2$ at concentrations as low as 2.4 ppm.[238] The hybrid sensor demonstrated a markedly enhanced sensing performance, delivering a response nearly 6.94 times greater than that of pure $SnO_2$. In contrast, the ZnSe sensor exhibited negligible sensitivity under the same operating temperature of 160 °C.

Recently, Abimaheshwari *et al.* fabricated n-ZnSe/p-PANI hybrid using a straightforward hydrothermal method, followed by an evaluation of their $NO_2$ gas sensing capabilities.[239] While pristine ZnSe required an elevated temperature of 100 °C to exhibit a sensing response, the ZnSe/PANI composites showed significantly enhanced performance at much lower temperature (30 °C). Among the various formulations, the 20 wt% composite (denoted as ZnSe-P2) demonstrated an outstanding maximum response of 77% at a remarkably low temperature of 30 °C, whereas ZnSe-P1 and ZnSe-P3 exhibited considerably lower responses of 25% and 20%, respectively, under the same conditions. Moreover, at an operating temperature of 30 °C, the sensor recorded a response time ($T_{res}$) of 112 s and a recovery time ($T_{rec}$) of 648 s, at an operating temperature of 30 °C. The enhanced sensing capability of the fabricated sensor is primarily attributed to the formation of a depletion region at the ZnSe/PANI interface, which facilitates efficient charge transfer and provides a greater number of active sites for gas interaction. Factors such as the operating temperature, composite composition, and nature of the target gas play crucial roles in determining the overall sensing performance. To determine the most effective operating temperature for the developed sensor, a temperature-dependent sensing study was carried out at 30 °C, 50 °C, and 100 °C using 20 ppm of $NO_2$ gas, as illustrated in Fig. 27(a). Pure ZnSe demonstrated its highest response of 9.4% at 100 °C, indicating a preference for elevated temperatures. In contrast, the composite sensors achieved their peak performance at 30 °C, highlighting a significant reduction in optimal operating temperature due to the incorporation of PANI. As the temperature exceeded the optimal point, the sensing responses of the composites began to decline. This decrease is attributed to the dominance of desorption over adsorption at elevated temperatures. Notably, incorporating PANI into the ZnSe matrix significantly enhanced the gas sensing response compared to pure ZnSe, indicating that the improved interfacial charge transfer between ZnSe and PANI

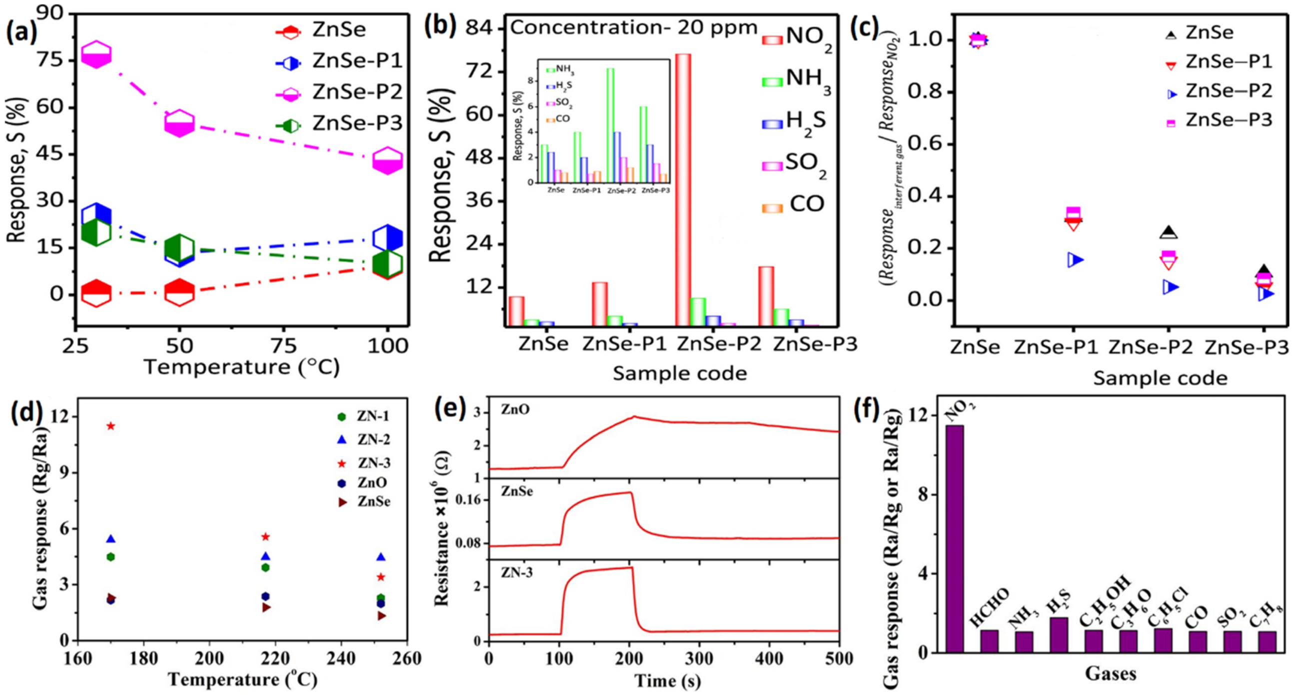

Fig. 27 (a) Sensing response as a function of operating temperature, (b) selectivity, and (c) selectivity factor of the fabricated sensors (reproduced from ref. 239); (d) comparative $NO_2$ sensing performance of ZnO–ZnSe variants (ZN-1, ZN-2, ZN-3) alongside pristine ZnO and ZnSe across varying temperatures, (e) response performance of ZnO, ZnSe and ZN-3 sensors toward 10 ppm $NO_2$ at 170 °C, and (f) response profiles of the ZN-3 sensor toward $NO_2$ and other common gases (reproduced from ref. 240). "This figure has been reproduced from ref. 239 with permission from Elsevier, copyright 2024". "This figure has been reproduced from ref. 240 with permission from Elsevier, copyright 2023".

contributes to the reduced optimal operating temperature of 30 °C. However, an excessive amount of PANI led to a decline in sensing performance, due to the aggregation of ZnSe particles on the surface of the PANI sheets, which decreases the effective surface area and limits the number of accessible active sites for gas adsorption, ultimately impairing sensor efficiency. To evaluate selectivity, sensing measurements were performed against various gases, including $NO_2$, $NH_3$, $H_2S$, $SO_2$, and CO. As illustrated in Fig. 27(b) and (c), all sensors demonstrated the highest response toward $NO_2$, confirming strong selectivity. This selective behaviour varies depending on the nature of the target gas and is governed by factors such as surface reaction dynamics, kinetic energy, and ionization energy of the analyte. $NO_2$, with a relatively small kinetic diameter of 310 pm and a lower ionization energy of 9.586 eV, interacts more readily with the sensing materials, accounting for its preferential detection over other gases.

In another study, Gao *et al.* utilized a one-step, template-free hydrothermal synthesis approach to prepare ZnO–ZnSe hollow nanospheres rich in nano-heterojunctions.[240] The gas sensing responses of ZnO, ZnSe, and ZnO–ZnSe composites were evaluated toward 10 ppm $NO_2$ at various operating temperatures, demonstrating optimal sensing performance at 170 °C (Fig. 27(d)). As illustrated in Fig. 27(e), the transient response profiles showed a markedly enhanced response for ZN-3, approximately 5.32 and 5.02 times greater than that of pure ZnO and ZnSe, respectively. Fig. 27(f) illustrates the selectivity analysis of the ZN-3 sensor toward $NO_2$ and a range of potential interfering gases. At 170 °C, the ZnO–ZnSe composite sensor exhibited a high response of 11.49 to 10 ppm $NO_2$, while significantly lower responses were recorded for formaldehyde (1.15), $NH_3$ (1.07), $H_2S$ (1.79), ethanol (1.14), acetone (1.13), chlorobenzene (1.23), CO (1.09), $SO_2$ (1.09), and toluene (1.08) at 100 ppm each. At 10 ppm, the sensor achieved a response of 11.49 with a response time of 100 s and a recovery time of 48 s. Notably, the sensor demonstrated a detection limit as low as 100 ppb.

Besides $NO_2$, ammonia ($NH_3$) is another widespread air pollutant, primarily originating from agricultural practices, animal husbandry, and industrial processes.[241] Exposure to high concentrations of $NH_3$-either acute or prolonged-can lead to serious health complications, including respiratory distress, organ damage, and in severe cases, death. Even at lower concentrations, sustained exposure may contribute to chronic inflammatory conditions.[242] Therefore, developing a sensor capable of detecting ammonia at parts-per-million (ppm) levels is of critical importance. Recently, Thayil and Parne fabricated ZnSe nanostructures exhibiting spherical and flower-like morphologies by adjusting the concentration of ethylenediaminetetraacetic acid (EDTA).[243] These nanostructures were utilized for $NH_3$ gas sensing at room temperature for the first time. Their study demonstrated that increased EDTA content promoted the formation of flower-like structures, which offer enhanced surface area, an essential factor for improving gas sensing efficiency. The improved sensing behaviour of ZnSe prepared with 2 g of EDTA is largely credited to its flower-like structure, which increases the active surface area, enhancing gas adsorption. In the presence of air, oxygen molecules adsorb onto the ZnSe surface and capture electrons, forming ionized oxygen species ($O_2^-$), as described in the following reaction steps:

$$O_2(\text{gas}) \rightarrow O_2(\text{ads}) \tag{38}$$

$$O_2(\text{ads}) + e^- \rightarrow O_2^-(\text{ads}) \tag{39}$$

when $NH_3$ molecules come into contact with the ZnSe surface, they react with the adsorbed oxygen species, leading to electron transfer back into the ZnSe material, as illustrated in the following reaction:

$$3O_2^-(\text{ads}) + 4NH_3 \rightarrow 2N_2 + 6H_2O + 2e^- \tag{40}$$

The restoration of electrons to the ZnSe surface results in a measurable change in resistance, serving as the detection signal.

On the other hand, acetone is a prevalent volatile organic compound that plays a significant role in human metabolism. Monitoring acetone levels has become crucial for physicians to assess patient health. Typically, acetone concentrations in the breath of healthy adults are below 0.8 ppm, whereas in diabetic patients, these levels can rise to around 1.8 ppm due to irregular glucose metabolism.[245,246] Therefore, accurate detection of acetone gas, particularly around the 1 ppm level, can help effectively prevent potential risks associated with acetone accumulation and enable real-time monitoring of human health. In 2022, Zhu *et al.* developed an oxygen-vacancy-rich ZnO/ZnSe heterojunction by embedding ZnSe into ZIF-8-derived ZnO, followed by an annealing process.[244] The resulting material demonstrated superior acetone sensing capabilities, even at low concentrations. To determine the optimal operating temperature for gas sensitivity, the sensor's response to 50 ppm acetone was systematically evaluated across varying temperatures. As depicted in Fig. 28(a), the ZnO/ZnSe-2 and

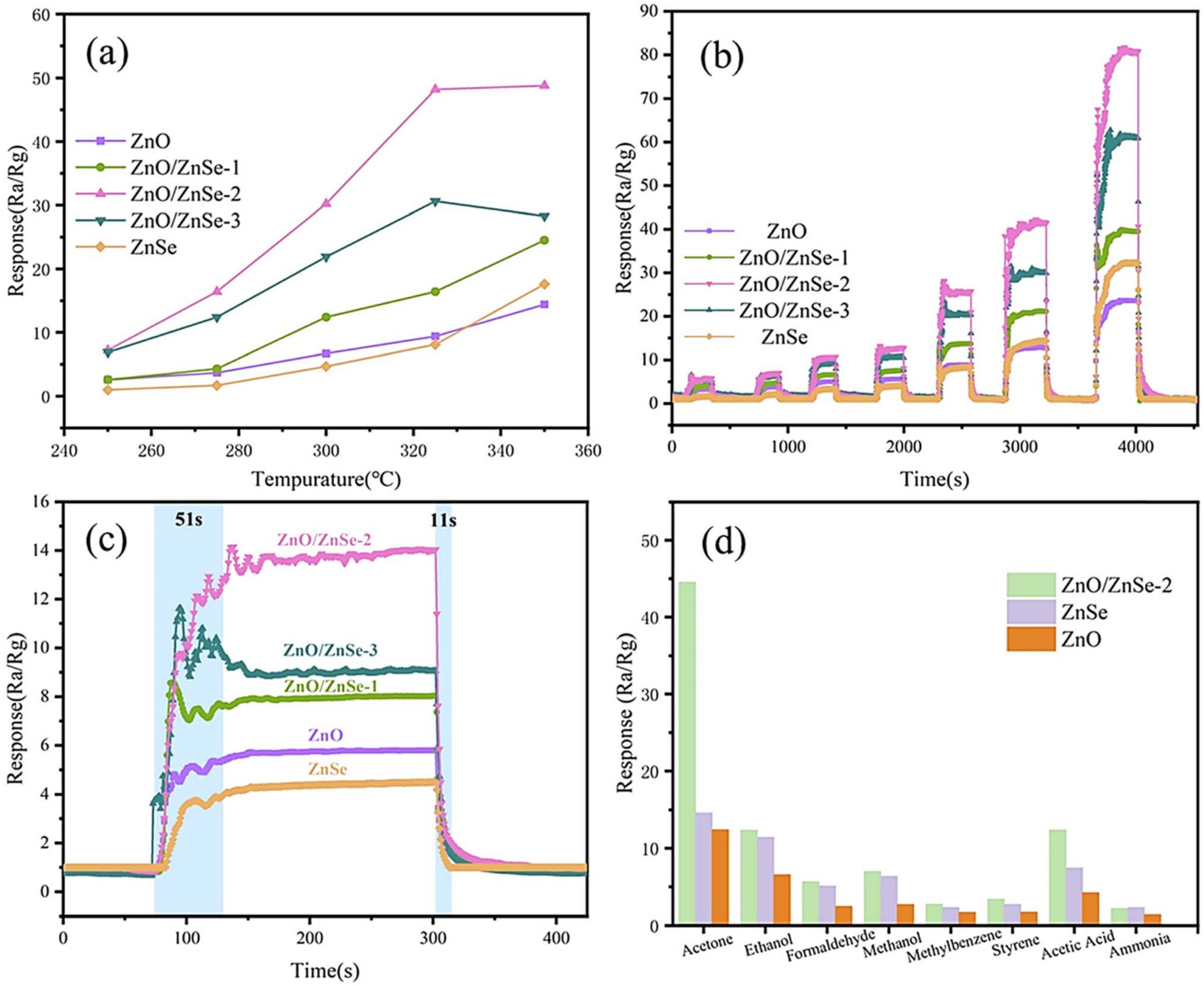

Fig. 28 (a) Sensor responses to 50 ppm acetone as a function of operating temperature, (b) real-time response curves at 325 °C for acetone concentrations ranging from 1–100 ppm, (c) dynamic response profile towards 10 ppm acetone at 325 °C, and (d) selectivity profiles of sensors toward various interfering gases at 325 °C (reproduced from ref. 244). "This figure has been reproduced from ref. 244 with permission from Elsevier, copyright 2022".

ZnO/ZnSe-3 composites demonstrated markedly superior responses around 325 °C compared to pristine ZnO and ZnSe. This enhancement confirms that the heterojunction composites significantly improve sensing performance while enabling operation at a comparatively lower temperature. To further evaluate the influence of composition on acetone sensing, dynamic response measurements were carried out for ZnO, ZnSe, and the three composite variants over a concentration range of 1–100 ppm. As shown in Fig. 28(b), ZnO/ZnSe-2 demonstrated exceptional sensitivity, with response values of 5.8, 7.2, 10.7, 12.7, 25.6, 42.3, and 80.8 corresponding to acetone concentrations of 1, 2, 5, 10, 20, 50, and 100 ppm, respectively. Notably, the composite exhibited excellent low-concentration detection, achieving a substantial response of 5.8 even at 1 ppm, underscoring its strong potential for trace-level acetone sensing in practical applications. Furthermore, the ZnO/ZnSe-2 composite exhibited rapid sensing dynamics, with a notably short response time of 51 s and an even faster recovery time of approximately 11 s, highlighting its excellent reversibility and responsiveness (Fig. 28(c)). To further examine its selectivity, the sensor was exposed to various common interfering gases (each at 50 ppm) under a constant operating temperature of 325 °C. As illustrated in Fig. 28(d), the ZnO/ZnSe-2 composite showed a significantly higher response to acetone compared to other gases, underscoring its strong selectivity and potential for reliable acetone detection in complex environmental conditions.

Apart from the above mentioned gases, other gases such as $CO_2$ and $SO_2$ are hazardous with well-documented adverse impacts on human health.[247] $CO_2$, a major greenhouse gas, plays a critical role in accelerating global climate change through enhanced atmospheric warming.[248] In contrast, $SO_2$ is a pungent, corrosive, and toxic gas primarily emitted from various manufacturing processes.[249] Inhalation of $SO_2$ can lead to a range of serious health issues, including respiratory disorders, cardiovascular complications, and acute breathing difficulties. In a recent study, Khalil *et al.* explored the gas-sensing capabilities of ZnSe nanocages toward $CO_2$ and $SO_2$ using DFT simulations.[40] The interaction energies confirm that all isomeric configurations are thermodynamically stable, with adsorption processes characterized as exothermic. The study revealed distinct adsorption behaviours: $SO_2$ molecules undergo physisorption on the ZnSe nanocage surface, while $CO_2$ molecules exhibit chemisorption. Among the investigated configurations, the $CO_2$@ZnSe-A isomer was identified as the most stable, exhibiting the highest adsorption affinity toward $CO_2$ with a substantial interaction energy of $-149.8$ kcal mol$^{-1}$. This highlights the superior adsorption capability of the ZnSe nanocage compared to previously reported ZnSe nanotube structures.

## 6.5. Energy storage

The rapid growth of the global economy has led to an increasing demand for energy, which is still largely met by fossil fuels such as oil, natural gas, and coal. However, these non-renewable resources are being depleted at an alarming rate. Moreover, their continued use significantly contributes to environmental degradation and climate change. As a result, the shift toward sustainable and renewable energy sources has become a critical global priority.[250] With the advancement of innovative concepts and deeper understanding in material physics and chemistry, significant progress has been achieved in cutting-edge renewable energy storage technologies, including fuel cells, batteries, and supercapacitors. Furthermore, the rising demand for electric vehicles has positioned energy storage systems, particularly lithium-ion batteries (LIBs), at the forefront of technological research and development.[251,252] In this perspective, ZnSe has emerged as a promising material for energy storage owing to its excellent electrochemical characteristics, making it suitable for applications in supercapacitors and Li-ion batteries. As a potential high-capacity anode material for advanced Li-ion batteries, a thorough understanding of its electrochemical reaction pathways is crucial for designing efficient electrodes and enhancing overall performance. Additionally, the weaker M–S, M–Se, and M–Te bonds compared to M–O bonds in oxides enhance the kinetics of conversion reactions during charge/discharge cycles.[253] *Ex situ* X-ray diffraction (XRD) and extended X-ray absorption fine structure (EXAFS) studies have shown that during lithiation, ZnS undergoes conversion into LiZn and $Li_2S$, while during delithiation, it only partially reverts back to ZnS, leaving residual traces of elemental Zn and S.[254,255] In the case of ZnSe, its lithiation–delithiation and sodiation–desodiation behaviours closely resemble those of ZnS and ZnO, indicating similar conversion-based electrochemical mechanisms.[256,257] However, the presence of selenium enables a more complete conversion reaction during charging, with lower voltage plateau (~1.3 V and ~1.0 V), attributed to its narrower band gap, reduced bond strength, and lower electronegativity.[258,259]

The electrochemical charge/discharge mechanism for ZnSe can be represented by the following reactions:

Intercalation and conversion reaction

$$xA^+ + \mathrm{ZnSe} + xe^- \leftrightarrow A_x\mathrm{Se} + \mathrm{Zn} \quad (0 < x \leq 2) \tag{41}$$

Alloying reaction

$$xA^+ + \mathrm{Zn} \leftrightarrow A_x\mathrm{Zn} - xe^- \quad (0 < x \leq 1) \tag{42}$$

Overall reaction

$$(x+2)A^+ + \mathrm{ZnSe} + (x+2)e^- \leftrightarrow A_2\mathrm{Se} + A_x\mathrm{Zn} \quad (0 < x \leq 1) \tag{43}$$

where, A = Li, Na, K.

### 6.5.1. Anode for Li ion batteries.

Beyond its extensive use in the semiconductor industry, ZnSe has attracted significant attention for energy storage applications due to its high theoretical capacity (557 mA h g$^{-1}$) and superior electrical conductivity.[258] To overcome performance limitations, extensive efforts have been directed towards engineering ZnSe nanostructures and hybridizing it with conductive carbon materials such as carbon nanoparticles, porous carbon, graphene, carbon nanotubes, and carbon nanofibers. These enhancements have been achieved using a variety of synthesis routes, including hydrothermal synthesis, pulsed laser deposition (PLD), *in situ* pyrolysis or selenization, and solid-state or mechanical milling approaches.[253] For example, using PLD, Xue *et al.* prepared highly crystalline ZnSe thin films and pioneered the investigation of its lithium storage mechanism through *ex situ* XRD and *in situ* absorbance spectroscopy.[260] Their analysis confirmed the reversible generation and decomposition of LiZn and $Li_2Se$, suggesting that both alloying/dealloying and partial selenidation/reduction of nanoscale Zn take place during the lithiation process. Despite showing better cycling performance than the Zn–Se/Li system (Zn–Se is a simple Zn and Se mixture), the ZnSe/Li cell suffered from notable irreversible capacity loss and poor cycle life, likely due to the high crystallinity of the zinc alloy phase and sluggish electrochemical kinetics. ZnSe and its composites, owing to their intrinsically low potential plateau, are well-suited for operation within a narrow voltage window (*e.g.*, 0–2.0 V), which can enhance the overall energy density and voltage efficiency in full-cell configurations. For instance, a ZnSe/C nanocomposite fabricated *via* a simple solid-state synthesis exhibited excellent cycling stability, retaining a very stable capacity retention of *ca.* 437 mA h $g^{-1}$ over 300 cycles at a current rate of 100 mA $g^{-1}$. In contrast, when cycled over a wider range of 0–3.0 V, a higher capacity of around 705 mA h $g^{-1}$ was achieved.[258]

Graphene, as a single-layer carbon material, offers exceptional advantages, such as high electrical conductivity, mechanical flexibility, large surface area, and structural robustness-making it an ideal support matrix for TMCs to enhance their electrochemical performance.[261] As a notable example, Zhang *et al.* synthesized polyhedral ZnSe/reduced graphene oxide (rGO) nanocomposites (ZnSe@rGO) *via* a simple one-pot hydrothermal method, where irregularly shaped ZnSe nanoparticles (∼40 nm) were uniformly anchored on graphene nanosheets.[262] When employed as anodes for lithium-ion batteries, these ZnSe/rGO nanocomposites demonstrated significantly enhanced electrochemical performance compared to pure ZnSe, attributed to the synergistic interaction between ZnSe and rGO. The composite delivered a high reversible capacity of 876 mA h $g^{-1}$ at 100 mA $g^{-1}$, along with remarkable cycling stability and rate capability-retaining 778 mA h $g^{-1}$ after 400 cycles at 1000 mA $g^{-1}$. In addition, the distinctive structure of the ZnSe/rGO nanocomposite plays a crucial role in improving performance by inhibiting ZnSe nanoparticle aggregation and preventing the restacking of graphene layers. The flexible graphene matrix serves as a conductive scaffold that facilitates rapid electron transport, buffers the volume changes of ZnSe and provides abundant accessible sites for lithium-ion storage. These synergistic effects result in enhanced electrochemical performance, highlighting the ZnSe/rGO

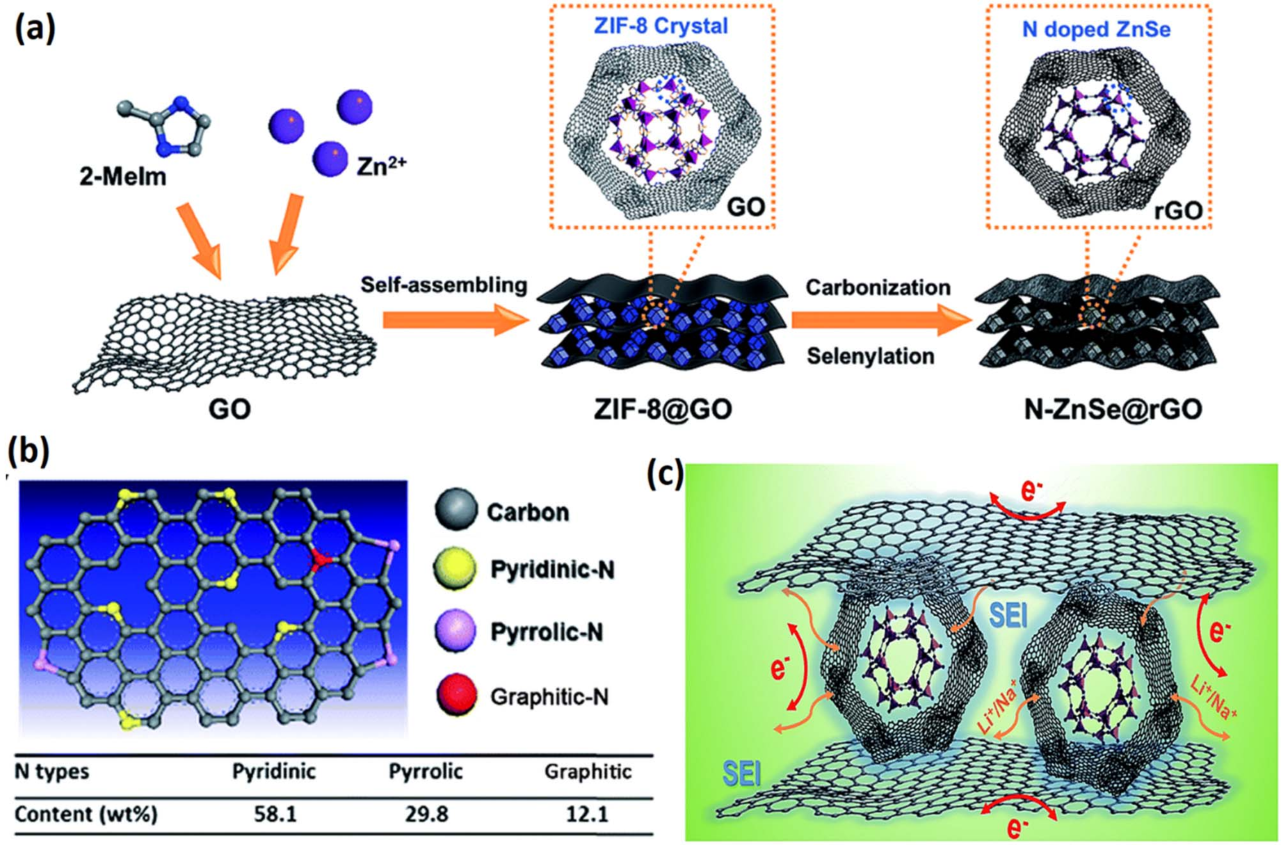

Fig. 29 (a) Schematic illustration of the preparation process of N-ZnSe@rGO, (b) graphical representation of the configurations and contents of three types of N in N-ZnSe@rGO, and (c) schematic illustration of the related mechanism of $Li^+/Na^+$ intercalation and extraction in the N–ZnSe@rGO electrode (reproduced from ref. 263).

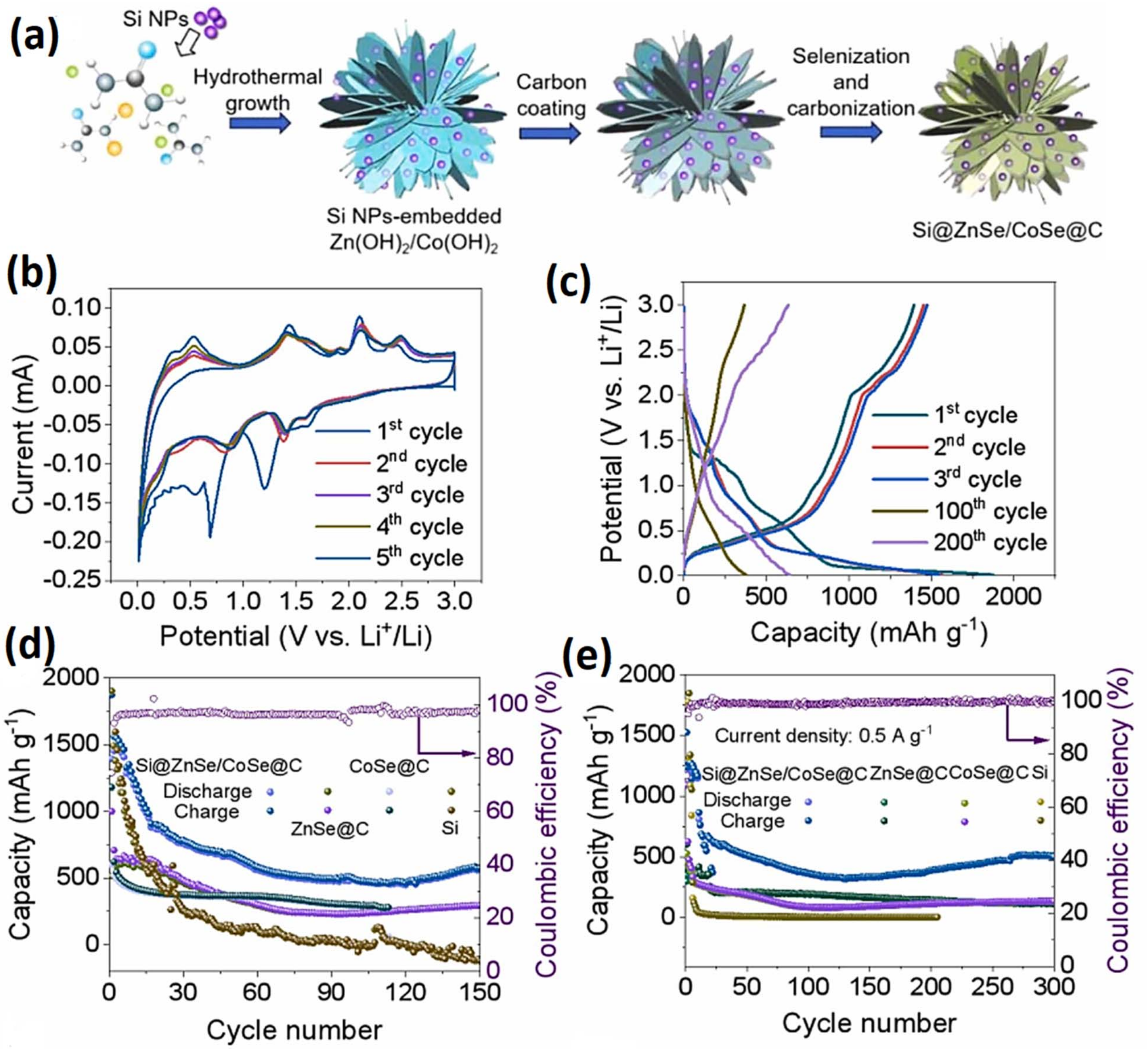

Fig. 30 (a) Illustration for the sample preparation, (b) CV profiles of Si@ZnSe/CoSe@C cycling at 0.1 mV s$^{-1}$, (c) charge–discharge profiles of Si@ZnSe/CoSe@C at 0.1 A g$^{-1}$, capacities of Si@ZnSe/CoSe@C, CoSe@C, ZnSe@C and Si at (d) 0.1 and (e) 0.5 A g$^{-1}$, anodes were pre-cycled at 0.1 A g$^{-1}$ for activation 10 cycles (reproduced from ref. 265). "This figure has been reproduced from ref. 265 with permission from Elsevier, copyright 2025".

nanocomposite as a strong candidate for high-performance anode materials in advanced lithium-ion batteries. Two years later, Liu *et al.* developed nitrogen-doped ZnSe (N-ZnSe) polyhedra encapsulated in reduced graphene oxide (rGO) composites, derived from ZIF-8 *via* a carbonization–selenylation process (Fig. 29).[263] The optimized N-ZnSe@rGO composite demonstrated an exceptional capacity of 836 mA h g$^{-1}$ at 100 mA g$^{-1}$ and excellent long-term stability, retaining 464 mA h g$^{-1}$ at 2000 mA g$^{-1}$ after 1000 cycles when used as an anode in lithium-ion batteries. The N-doping of ZnSe increases the density of active sites and enhances electronic conductivity, while the rGO matrix offers a high surface area and conductive framework, facilitating charge transfer and preventing ZnSe pulverization and aggregation.

Again, Liu *et al.* synthesized nitrogen-doped carbon-encapsulated hollow ZnSe/CoSe$_2$ (ZnSe/CoSe$_2$@N–C) nanospheres through a straightforward solvothermal method followed by selenization and carbonization.[264] The resulting nanospheres exhibited a multi-level nanoscale architecture, comprising a thin nitrogen-doped carbon shell (~12 nm) and hollow selenide cores formed by nanoscale subunits with rough surface features and abundant internal voids. The robust nitrogen-doped carbon shell, combined with the synergistic interaction between the dual metal ions (Zn and Co), significantly enhances both electron and ion transport, facilitating efficient lithium-ion insertion and extraction. As a result, the ZnSe/CoSe$_2$@N–C nanospheres exhibit a high reversible capacity of 1153 mA h g$^{-1}$ over 100 cycles at 100 mA g$^{-1}$ and

Table 5 Summary of the lithium storage performance of previously reported ZnSe-based materials

| Composite | Current density (mA $g^{-1}$) | Specific capacity (mA h $g^{-1}$) | Cycle no. | Voltage region (V) | ICE (%) | Ref. |
|---|---|---|---|---|---|---|
| ZnSe/C | 100 | 705 | 300 | 0–3 | 76 | 258 |
| ZnSe@NC nanocubes | 500 | 1167 | 500 | 0.01–3.0 | 68.8 | 266 |
| ZnSe–rGO | 100 | 876 | 50 | 0.01–3 | 58.6 | 262 |
| | 1000 | 778 | 400 | | | |
| MOF-derived ZnSe/NC | 1000 | 724.4 | 500 | 0.01–3.0 | 68.8 | 267 |
| ZnSe ND@N-PC | 600 | 1134 | 500 | 0.01–3.0 | 56.7 | 268 |
| Spherical-like ZnSe | 100 | 433 | 50 | 0.01–3.0 | 55.3 | 36 |
| ZnSe/C hollow spheres | 1000 | 574 | 800 | 0.01–3.0 | 73.9 | 269 |
| | 10 000 | 319 | 5000 | | | |
| ZnSe-NC@$CoSe_2$-NC | 200 | 718 | 600 | 0.005–3 | 67.6 | 270 |
| 3D ZnSe/$CoSe_2$-C composite | 100/1000 | 807/700 | 100/500 | 0.01–3.0 | 69 | 271 |

retain an impressive capacity of 966 mA h $g^{-1}$ after 500 cycles at a high current density of 2000 mA $g^{-1}$. Compared to other nitrogen-doped carbon architectures-such as hollow carbon spheres and mesoporous structures-these nanospheres demonstrate markedly superior cycling stability and capacity retention. Recently, an innovative strategy was introduced to improve the performance of lithium-ion battery anode by incorporating Si nanoparticles into a three-dimensional ZnSe/CoSe composite framework, which is further encapsulated within a carbon shell (Fig. 30(a)).[265] In the initial scan of the cyclic voltammetry (CV) profile of the Si@ZnSe/CoSe@C composite, distinct cathodic peaks appear at 1.62, 1.21, and 0.68 V (Fig. 30(b)). The peak at 1.62 V corresponds to the initial insertion of $Li^+$ ions into the composite matrix. The 1.21 V peak is attributed to the formation of $Li_xZn(Co)Se$ and the solid electrolyte interphase (SEI) layer on the anode surface, while the 0.68 V peak is associated with the conversion reaction between $Li_xZn(Co)Se$ and $Li^+$, resulting in the generation of metallic Co, Zn, and $Li_2Se$. Additionally, a peak at 0.23 V is ascribed to the reduction of Si to form $Li_xSi$ alloys. In the second scan, the cathodic peaks shift to 1.38 and 0.82 V, likely due to side reactions triggered by the initial lithiation/delithiation process. On the anodic side, a peak at 1.43 V corresponds to the multi-step dealloying of $Li_xZn$, while a broad peak centered at 2.10 V is indicative of the reversible selenization of Co, following the reaction: $Co + Li_2Se \rightarrow Li_xCoSe \rightarrow CoSe$. Additional peaks observed between 0.01–0.7 V are related to the electrochemical reactions among Co, Zn, and $Li_2Se$. Furthermore, the peaks at 0.32 and 0.53 V correspond to the transformation of $Li_xSi$ alloys back to amorphous Si. The consistent overlap of CV curves in subsequent cycles reflects the high reversibility and stability of the electrochemical processes. Fig. 30(c) presents the cycling performance of the Si@ZnSe/CoSe@C anode at 0.1 A $g^{-1}$. During the initial cycle, distinct discharge plateaus appear at 0.73 and 1.31 V, while charge plateaus are observed at 2.09 and 1.36 V, consistent with the CV results. The first-cycle discharge capacity reaches 1874 mA h $g^{-1}$, with an initial coulombic efficiency (CE) of 74.4%. Notably, the rapid increase in CE over subsequent cycles suggests effective suppression of irreversible side reactions, minimized electrolyte decomposition, and the formation of a stable and protective SEI layer. As shown in Fig. 30(d), the Si@ZnSe/CoSe@C anode delivers a stable specific capacity of 563 mA h $g^{-1}$ with a coulombic efficiency of 98.2% after 150 cycles at a current density of 0.1 A $g^{-1}$. Under a higher current density of 0.5 A $g^{-1}$, it maintains a capacity of 501 mA h $g^{-1}$ with an exceptional CE of 99.9% after 300 cycles (Fig. 30(e)). In contrast, ZnSe@C, CoSe@C, and pure Si electrodes exhibit significantly inferior cycling performance. The enhanced capacity and long-term stability of the Si@ZnSe/CoSe@C composite are attributed to the synergistic effect between the selenide phases and Si nanoparticles, as well as the unique 3D flower-like architecture. This robust structure effectively accommodates volume expansion during cycling by providing internal void spaces that buffer mechanical stress. The electrochemical reaction mechanisms involved in the cycling of the Si@ZnSe/CoSe@C anode are outlined below, and a comparative summary of the lithium storage performance of representative ZnSe-based materials is provided in Table 5.

Reduction process:

$$CoSe + xLi^+ \rightarrow Li_xCoSe \quad (1.21\ V) \tag{44}$$

$$Li_xZn(Co)Se + Li^+ \rightarrow Co + Zn + Li_2Se \quad (0.68\ V) \tag{45}$$

$$Si + xLi^+ \rightarrow Li_xSi \quad (0.23\ V) \tag{46}$$

Oxidation process:

$$Co + Li_2Se \rightarrow Li_xCoSe \rightarrow CoSe \quad (2.10\ V) \tag{47}$$

$$Li_xZn \rightarrow xLi^+ + Zn \quad (1.43\ V) \tag{48}$$

$$Co + Zn + Li_2Se \rightarrow Li_xZn(Co)Se \quad (0.01\text{–}0.7\ V) \tag{49}$$

$$Li_xSi \rightarrow Si + xLi^+ \quad (0.32\ V,\ 0.53\ V) \tag{50}$$

### 6.5.2. Anodes for sodium ion batteries.

Sodium-ion batteries (SIBs) have emerged as highly promising candidates for large-scale energy storage systems. Transition metal chalcogenides (TMCs), known for their alloying and conversion reaction mechanisms, are extensively investigated as anode materials due to their high theoretical capacities and rich redox chemistry.[272] Among them, ZnSe has demonstrated notable

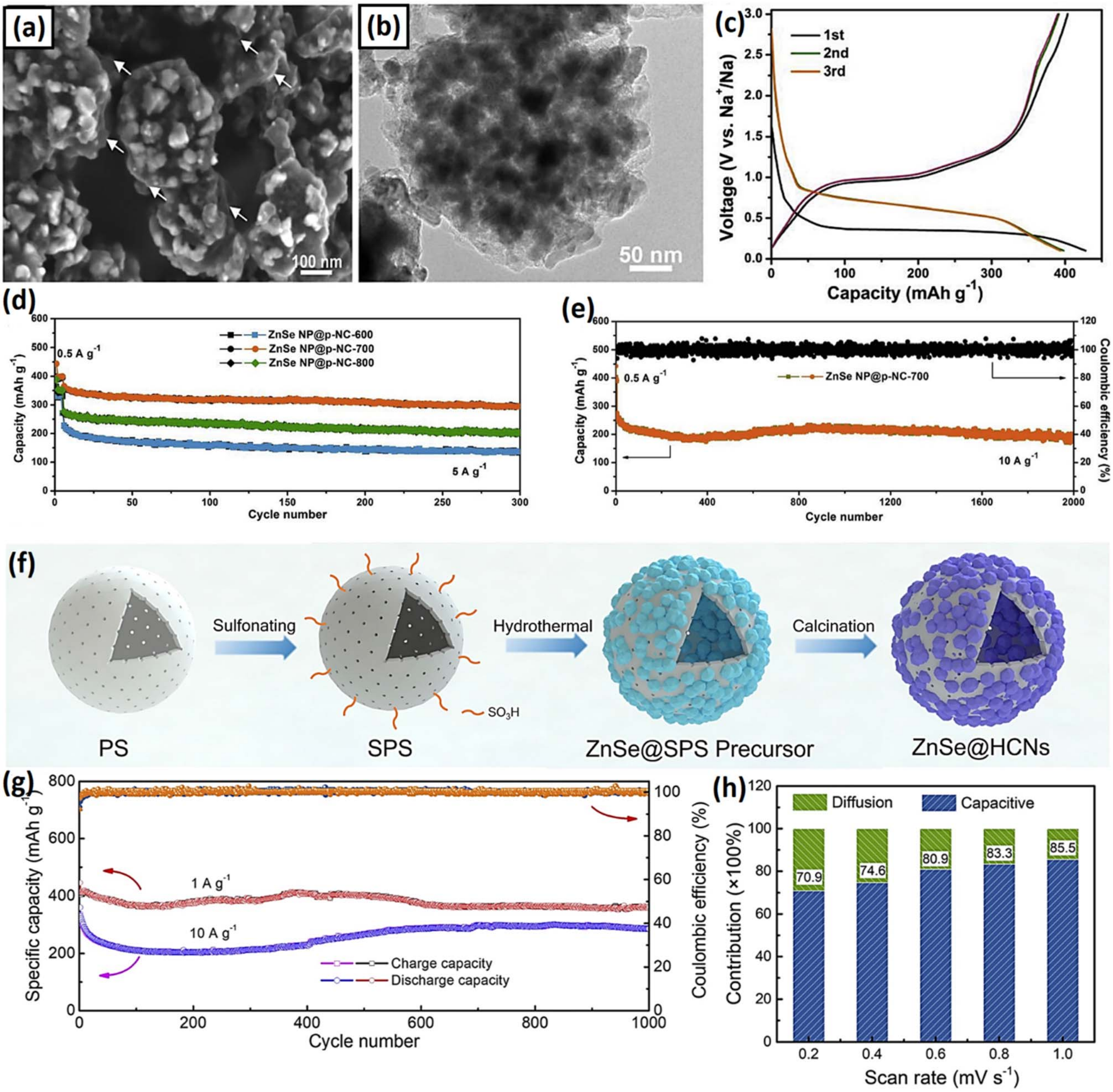

Fig. 31 (a) FESEM, and (b) TEM images of the synthesized ZnSe NP@p-NC-700, electrochemical performances: (c) GCD profiles of ZnSe NP@p-NC-700 at a current density of 0.5 A $g^{-1}$), (d and e) cycling performance of different ZnSe NP@p-NCs synthesized at varied temperatures at current densities of 5 and 10 A $g^{-1}$, respectively (reproduced from ref. 273); (f) schematic illustration of the formation of hybrid ZnSe@HCNs, electrochemical performance of ZnSe@HCNs: (g) cyclic stability at 1.0 and 10 A $g^{-1}$, and (h) percent of pseudocapacitive contribution at different scan rate (reproduced from ref. 274). "This figure has been reproduced from ref. 273 with permission from Elsevier, copyright 2019". "This figure has been reproduced from ref. 274 with permission from Elsevier, copyright 2019".

electrochemical activity as an anode material for SIBs, extending its potential beyond lithium-ion battery applications.[253] For example, Li *et al.* synthesized a hierarchical hybrid material ZnSe nanoparticles intricately confined within a 3D porous nitrogen-doped graphitic carbon framework (ZnSe NP@pNC), using a self-templated *in situ* selenation reaction between Zn-based zeolitic imidazolate framework (ZIF-8) nanododecahedra and selenium powder (Fig. 31(a and b)).[273]

This "popcorn ball"-like architecture, with its tailored porosity and conductive carbon matrix, significantly enhances sodium-ion storage kinetics. The resulting ZnSe NP@pNC composite showcases remarkable electrochemical performance, including a high initial coulombic efficiency (94.3%), outstanding rate capability, and long-term cycling stability, delivering 294.2 mA h $g^{-1}$ after 300 cycles at 5 A $g^{-1}$ and retaining 181.7 mA h $g^{-1}$ even after 2000 cycles at 10 A $g^{-1}$ (Fig. 31(c–e)). The ZnSe NP@p-NC composites, featuring highly

Table 6 Summary of the Na-storage performance of previously reported ZnSe based materials

| Type | Current density (mA $g^{-1}$) | Specific capacity (mA h $g^{-1}$) | Cycle no. | Voltage region (V) | ICE % | Ref. |
|---|---|---|---|---|---|---|
| ZnSe@C@rGO | 500/5000 | 293/224 | 140/1000 | 0.01–3.0 | 68.1 | 275 |
| 3D hierarchical ZnSe/C | 500/5000 | 434/285 | 500/1000 | 0.1–3.0 | 86.3 | 276 |
| $CoSe_2$/ZnSe@NC nanobox | 10 000 | 232/212 | 3000/10 000 | 0–3.0 | 71.7 | 278 |
| ZnSe/$Sb_2Se_3$@NC | 500/5000 | 438/295 | 120/250 | 0.01–3.0 | 90.5 | 279 |
| ZnSe-NC@$CoSe_2$-NC | 100 | 309 | 150 | 0.005–3.0 | 56.9 | 270 |
| ZnSe–$FeSe_2$/rGO | 50 | 363 | 100 | 0.01–3.0 | 76.9 | 280 |
| Willow-leaf-like ZnSe@NC | 200 | 71(107) | 1500 (550) | 0.01–3.0 | 51.3 | 281 |
| ZnSe@PCNF (N-doped mesoporous carbon nanofibers) | 500 | 270 | 1000 | 0.01–3.0 | 66 | 282 |
| $SnSe_2$/ZnSe@PDA nanobox | 100/1000 | 744/616 | 200/1000 | 0.1–3.0 | 71.6 | 283 |
| Open ZnSe/C nanocages | 50/500 | 318/189 | 50/1000 | 0.01–2.5 | 47.8 | 284 |

crystalline ZnSe with minimal lattice defects and well-regulated particle dispersion, exhibit significantly reduced ion diffusion resistance and superior electrochemical performance, particularly enhanced rate capability. Furthermore, the elevated ZnSe content and increased graphitization degree of the carbon matrix synergistically contribute to improved electronic conductivity within the composite.

Designing ZnSe at the nanoscale and integrating it with carbon-based matrices have emerged as effective strategies for enhancing electrochemical performance. Men *et al.* reported that the ZnSe@C electrode promoted the formation of

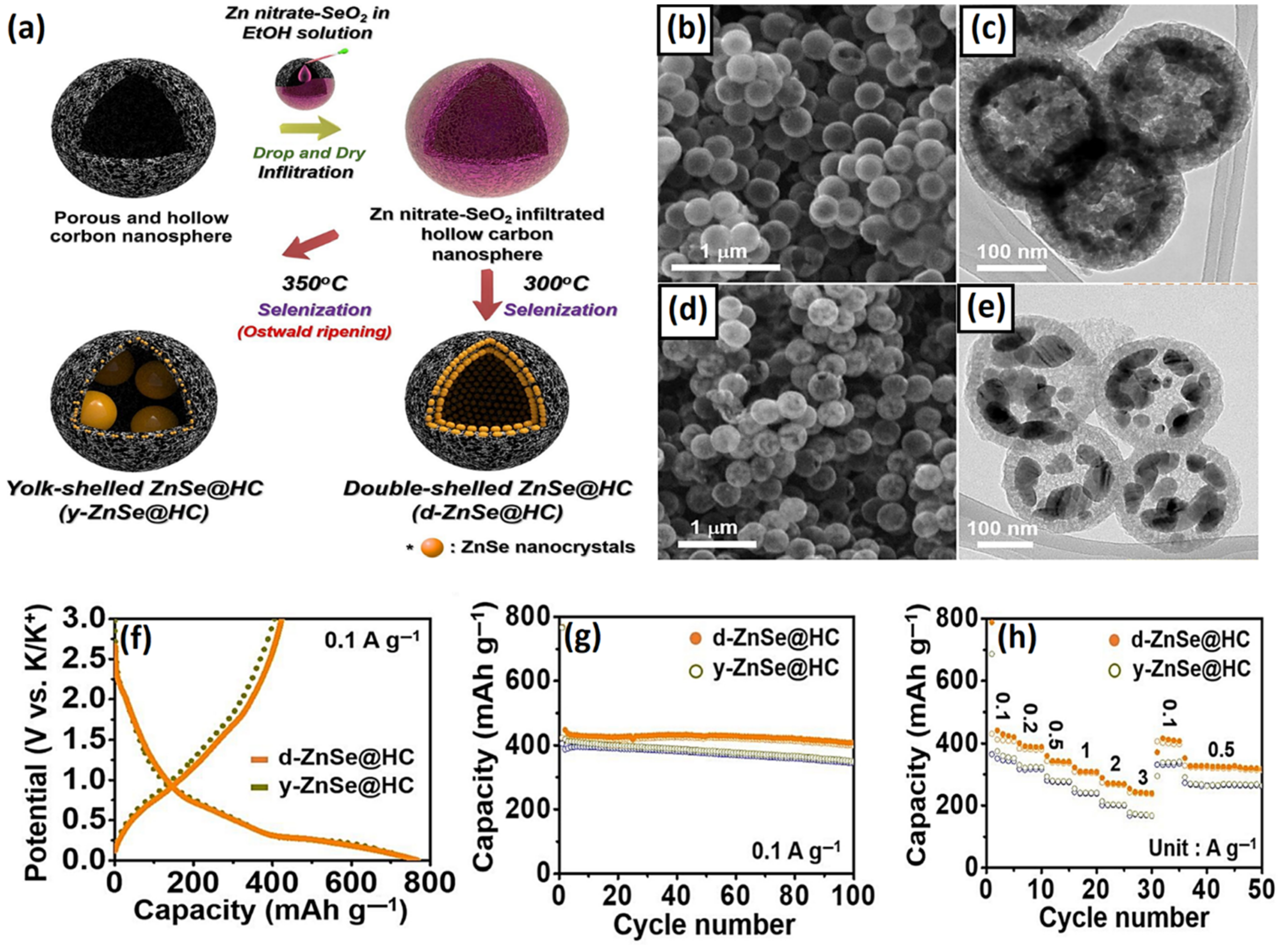

Fig. 32 (a) Schematic preparation diagram of y-ZnSe@HC and d-ZnSe@HC; TEM images of (b and c) d-ZnSe@HC, and (d and e) y-ZnSe@HC; (f) initial discharge/charge profile of d-ZnSe@HC and y-ZnSe@HC at 0.1 A $g^{-1}$, and (g) corresponding cycling performance, and (h) rate performance of d-ZnSe@HC and y-ZnSe@HC at various current densities from 0.1 to 3 A $g^{-1}$ (reproduced from ref. 289). "This figure has been reproduced from ref. 289 with permission from John Wiley and Sons, copyright 2021".

a relatively thick SEI layer.[275] Notably, selenium actively participated in SEI formation and gets partially dissolved into the electrolyte as polyselenides during the reverse charging process, which in turn hindered ion diffusion kinetics and compromised structural stability of the electrode. In contrast, the incorporation of reduced graphene oxide (rGO) effectively mitigated electrolyte decomposition and facilitated the formation of a thin, stable SEI layer. Consequently, the ZnSe@C@rGO composite exhibited outstanding cycling stability, retaining 96.4% of its capacity after 1000 cycles at a high current density of 5 A $g^{-1}$. The formation of metal–oxygen–carbon (M–O–C) bonds has emerged as an effective strategy to enhance charge/ion transport, immobilize polyselenides, and improve structural integrity and electrochemical performance through deliberate structural design. In this context, Zn–O–C bonds were successfully engineered by anchoring ZnSe nanoparticles onto a 3D carbon matrix.[276] These Zn–O–C linkages act as electron/ion conductive bridges, significantly boosting charge transfer kinetics and ion diffusion. As a result, the ZnSe/C anode demonstrated impressive electrochemical performance, delivering a high-rate capability of 281.1 mA h $g^{-1}$ at 5 A $g^{-1}$ and maintaining a stable capacity of 434 mA h $g^{-1}$ over 500 cycles at 0.5 A $g^{-1}$.

Interestingly, ZnSe and its composites generally follow a diffusion-controlled mechanism (battery-type behaviour) when used as anodes in SIBs, differing from the surface-controlled (capacitor-like) behaviour commonly seen in LIBs.[37,273] However, an exception arises in the case of ultrafine ZnSe nanoparticles, which can exhibit significant pseudo-capacitive characteristics.[277] Lu *et al.* developed a well-defined hollow hybrid structure, wherein ultrafine ZnSe nanoparticles were simultaneously deposited on the inner and outer surfaces of amorphous hollow carbon nanospheres (ZnSe@HCNs) (Fig. 31(f)).[274] The unique hierarchical ZnSe@HCNs architecture facilitates a mixed sodium storage mechanism involving intercalation, conversion, and alloying reactions. During discharge to 0.1 V, ZnSe is transformed into $Na_2Se$ and a cubic $NaZn_{13}$ phase *via* multiple intermediates. This rational design effectively inhibits nanoparticle aggregation, preserves electrode architecture, and ensures structural robustness throughout cycling. As a result, the ZnSe@HCNs anode delivers excellent electrochemical performance, including a high reversible capacity, superior rate capability (266.5 mA h $g^{-1}$ at 20 A $g^{-1}$), prolonged cycling stability (361.9 mA h $g^{-1}$ at 1 A $g^{-1}$ over 1000 cycles with 87% retention), and a high ICE of 92.2% (Fig. 31(g

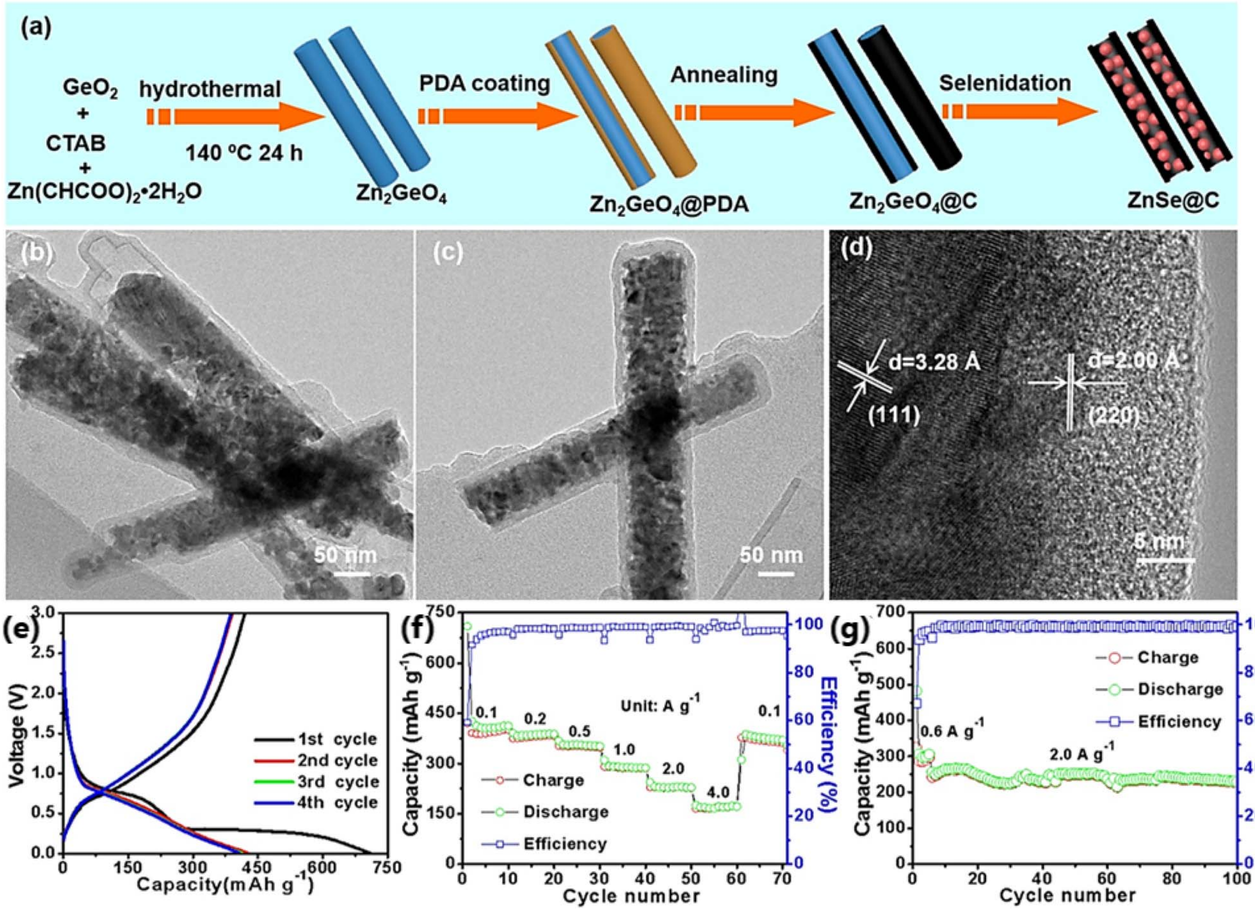

Fig. 33 (a) Schematic preparation diagram of porous ZnSe@C nanorods, (b and c) TEM, and (d) HRTEM image of ZnSe@C, (e) initial four discharge/charge profile at 0.1 A $g^{-1}$, (f) rate performance from 0.1 to 4.0 A $g^{-1}$, and (g) long-term cycling stability of ZnSe@C nanorods at 2.0 A $g^{-1}$ (reproduced from ref. 285). "This figure has been reproduced from ref. 285 with permission from Elsevier, copyright 2020".

Table 7 Electrochemical performance comparisons of recently reported ZnSe-based materials for PIBs

| Composite | Current density (mA $g^{-1}$) | Specific capacity (mA h $g^{-1}$) | Cycle no. | Voltage region (V) | ICE (%) | Ref. |
|---|---|---|---|---|---|---|
| ZnSe–C@NC | 1000 | 326.6 | 1000 | 0.01–3.0 | 81.8 | 290 |
| LN-ZnSe/C | 200 | 383 | 100 | 0.01–3.0 | 59.5 | 291 |
| | 1000 | 179 | 1200 | 0.01–3.0 | | |
| MP-ZnSe@NC | 500 | 247 | 500 | 0.01–3.0 | 61 | 38 |
| ZnSe@NC NFs | 200 | 337 | 300 | 0.01–3.0 | 62 | 292 |
| ZnSe NP@NHC | 100/200 | 133/111 | 1200/1600 | 0.3–2.9 | 47.7 | 293 |
| ZnSe–$FeSe_2$/rGO | 50 | 363 | 100 | 0.01–3.0 | 36.3 | 280 |
| Open ZnSe/C nanocages | 50/500 | 318/189 | 50/1000 | 0.01–2.5 | 47.8 | 284 |
| Double-shell ZnSe–C nanospheres | 100/200 | 400/230 (170) | 100/200 | 0.01–3 | 55 | 289 |

and h)). Table 6 shows the summary of the Na-storage performance of the previously reported ZnSe based materials.

**6.5.3. Anodes for potassium ion batteries.** Potassium-ion batteries (PIBs) have emerged as a promising alternative to lithium-ion batteries (LIBs) due to the low redox potential and natural abundance of potassium, which is comparable to that of sodium but with a more favorable redox potential.[285,286] Nevertheless, the relatively large ionic radius of $K^+$ presents challenges such as sluggish reaction kinetics and potential structural degradation of electrode materials. To address these issues, extensive research has focused on the design of suitable active materials and advanced electrode architectures. Among these, TMCs, particularly ZnSe-based anodes, have garnered attention due to their advantageous potential plateau, high theoretical capacity, good electrical conductivity, and cost-effectiveness. ZnSe integrates the benefits of both conversion and alloying mechanisms, making it a promising anode material for PIBs. It offers relatively high energy conversion efficiency, excellent electronic conductivity, and long cycling stability, and has thus garnered significant interest in recent years as a next-generation electrode material.[277,287,288] Lee *et al.* synthesized carbon-coated ZnSe nanospheres with yolk–shell (y-ZnSe@HC) and double-shell (d-ZnSe@HC) architectures through an infiltration-assisted selenization strategy (Fig. 32(a)).[289] SEM and TEM analyses confirmed the formation of uniformly shaped nanospheres with comparable diameters, although the y-ZnSe@HC displayed a slightly larger ZnSe core size (Fig. 32(b–e)). In terms of electrochemical performance, the y-ZnSe@HC exhibited a marginally higher reversible capacity than the d-ZnSe@HC, likely due to improved structural dynamics and ion transport pathways. When tested at a current density of 0.1 A $g^{-1}$, the double-shell structured ZnSe@C (d-ZnSe@HC) demonstrates a higher reversible capacity of 400 mA h $g^{-1}$ after 100 cycles, compared to 360 mA h $g^{-1}$ for the

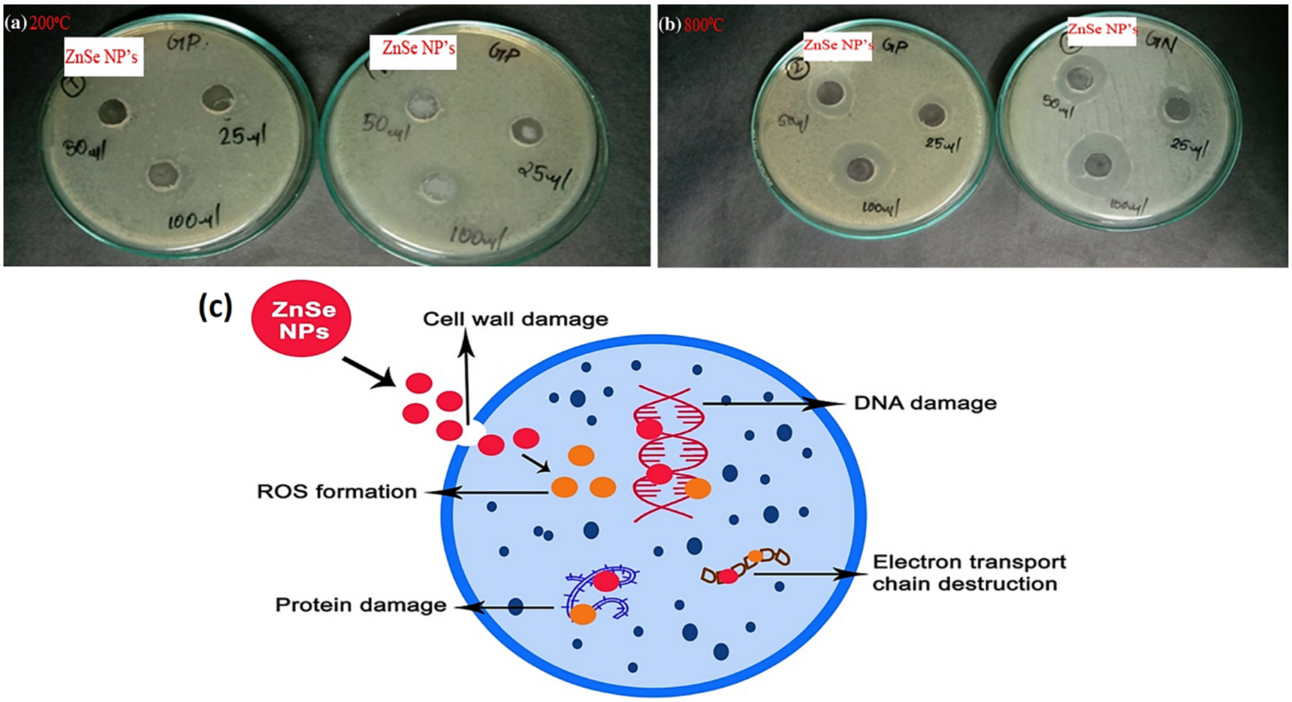

Fig. 34 Antibacterial activity of ZnSe nanoparticles calcined at (a) 200 °C, (b) 800 °C, and (c) mechanism of the action of ZnSe nanoparticles on bacterial cell (reproduced from ref. 72). "This figure has been reproduced from ref. 72 with permission from Springer Nature, copyright 2021".

yolk–shell counterpart (y-ZnSe@HC) (Fig. 32(f and g)). Furthermore, under varying current densities of 0.1, 0.2, 0.5, 1, 2, and 3 A $g^{-1}$, d-ZnSe@HC delivers capacities of 400, 385, 340, 300, 270, and 240 mA h $g^{-1}$, respectively (Fig. 32(h)). These values consistently outperform those of y-ZnSe@HC, which exhibits corresponding capacities of 380, 320, 275, 240, 200, and 170 mA h $g^{-1}$.

Porous and hollow nanostructures are advantageous and offer ample internal voids for mitigating volume expansion, due to their high surface area and open frameworks. Xu *et al.* strategically synthesized nitrogen-doped carbon-decorated porous ZnSe@C nanorods *via* a hydrothermal approach, which was coupled with *in situ* dopamine polymerization and a subsequent hydrothermal sulfidation process (Fig. 33(a)).[285] The TEM images (Fig. 33(b–d)) confirm the presence of fine ZnSe nanoparticles encapsulated within a carbon shell, with a measured lattice spacing of 3.28 Å, corresponding to the (111) plane of ZnSe.

As shown in Fig. 33(e), the ZnSe@C anode delivered an initial discharge capacity of 709 mA h $g^{-1}$ with a reversible capacity of 420 mA h $g^{-1}$ and ICE of 59.2%. Upon increasing the current densities from 0.1 to 0.2, 0.5, 1.0, 2.0, and 4.0 A $g^{-1}$, the electrode retained capacities of 389, 380, 352, 286, 226, and 168 mA h $g^{-1}$, respectively (Fig. 33(f)). The unique ZnSe@C nanorod significantly buffered the volume fluctuations during cycling and improved electronic conductivity, resulting in a stable capacity of 204 mA h $g^{-1}$ after 100 cycles at 2.0 A $g^{-1}$ for potassium-ion battery applications (Fig. 33(g)).[285] The outstanding rate capability of ZnSe@C can be attributed to its distinctive porous nanorod structure wrapped in a conductive carbon shell, which offers abundant active sites and sufficient void space to accommodate K-ion insertion and mitigate volume changes. A comparative summary of the electrochemical performance of recently reported ZnSe-based anode materials for potassium-ion batteries is presented in Table 7.

### 6.6. Antimicrobial activities

Bacterial infections pose a serious global health risk, impacting economic and social progress. Developing stable antibiotic molecules could provide new strategies for controlling the rising spread of pathogenic and antibiotic-resistant bacteria.[294,295] The increase in bacterial mutations and the spread of hospital-acquired infections make treating resistant pathogens even more complex, especially in developing nations. This urgent situation calls for the discovery of innovative antibacterial agents to tackle antibiotic-resistant strains like *Staphylococcus aureus*, *Pseudomonas aeruginosa*, and *Escherichia coli*. Zinc chalcogenides offer promising results, showing effective antimicrobial properties against these harmful pathogens.[295,296] Conventional antibiotics disrupt bacterial cell wall construction, interfere with protein synthesis, or inhibit DNA replication. Nanoparticles, on the other hand, employ different strategies to destroy bacterial cells: (i) binding to the target cell surface and rupturing the cell wall, (ii) penetrating the cell wall to disrupt essential biochemical pathways, and (iii) producing reactive oxygen species that degrade the cell wall, causing cell death.[297] For instance, the antimicrobial activities of the ZnSe NPs calcined at 200 °C and 800 °C were analyzed by Beena *et al.*, tested against *B. subtilis* and *E. coli*, as shown in Fig. 34(a) and (b).[72] ZnSe nanoparticles at 800 °C show better anti-bacterial activity than

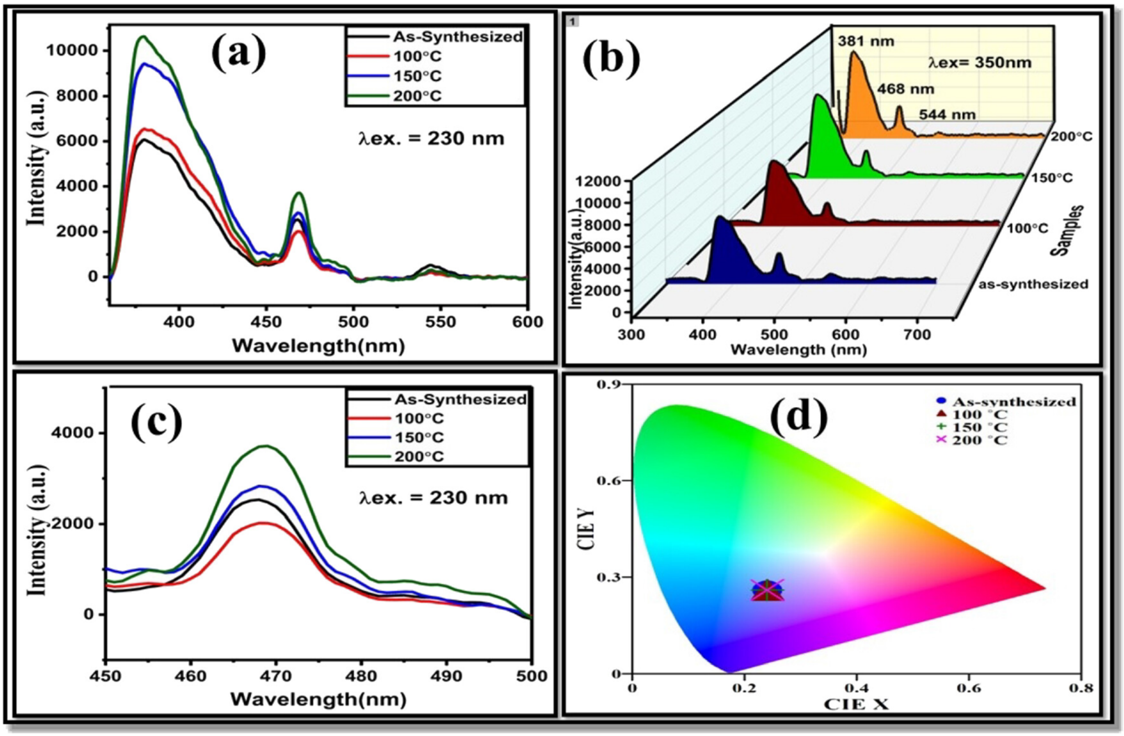

Fig. 35 (a) Photoluminescence spectra, (b) 3D image of photoluminescence spectra, (c) enlarged portion of photoluminescence spectra from 450 to 500 nm, (d) CIE plot of ZnSe NSs (reproduced from ref. 106).

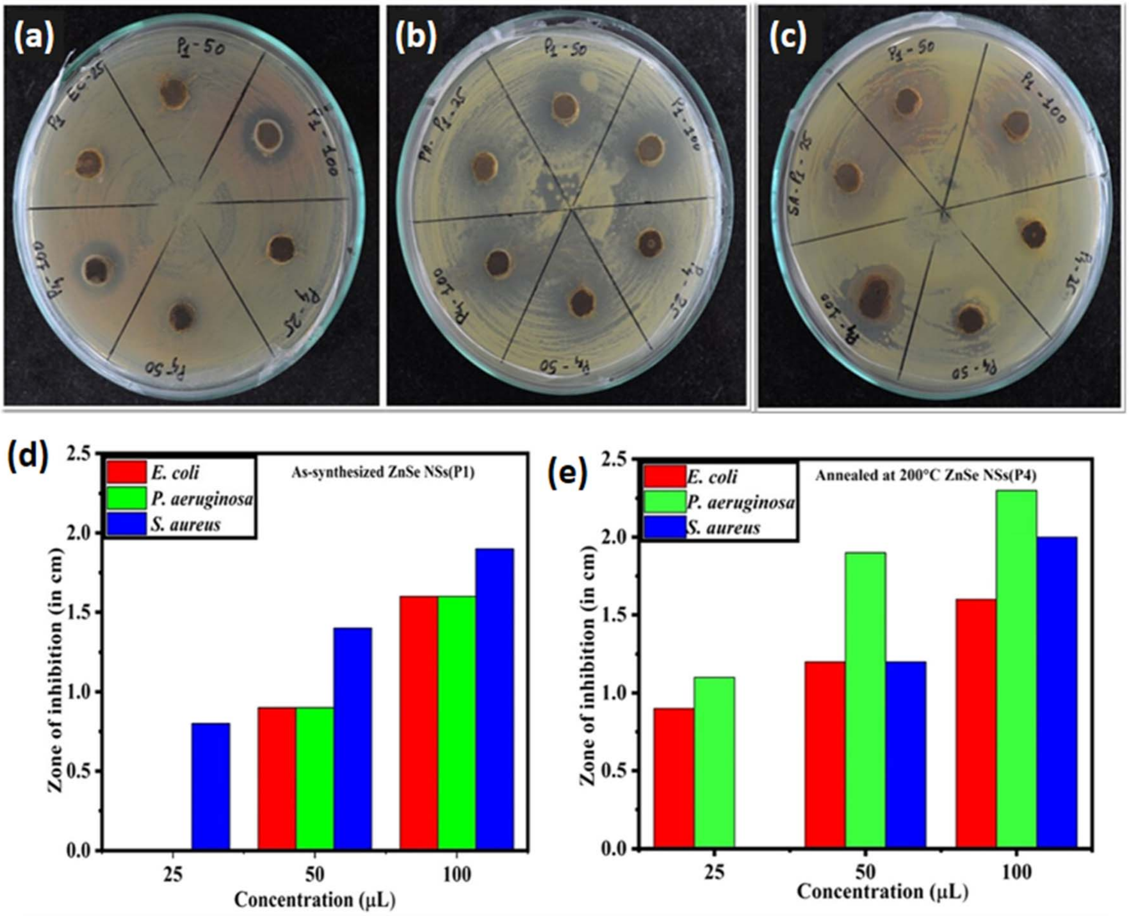

Fig. 36 Antibacterial activity of ZnSe NSs (P1 and P4) against: (a) *Escherichia coli*, (b) *Pseudomonas aeruginosa*, (c) *Staphylococcus aureus*, (d and e) bar graph displaying the antibacterial activities, highlighting the zones of inhibition (ZOI) against *Escherichia coli* (red), *Pseudomonas aeruginosa* (green), and *Staphylococcus aureus* (blue) (reproduced from ref. 106).

those at 200 °C, with lattice imperfections in the latter leading to reduced activity. The Zn and Se ions disrupt the cell wall and DNA, impairing DNA replication and destabilizing proteins. ROS formation from ZnSe NPs also affects the electron transport chain. The antibacterial mechanism is illustrated in Fig. 34(c).

Similar studies were performed by Gupta *et al.* by employing synthesized ZnSe nanostructures (NSs) through an eco-friendly co-precipitation method, followed by annealing at 100, 150, and 200 °C.[106] They assessed the antimicrobial activities of both the as-synthesized (P1) sample and the 200 °C annealed sample (P4) against *Escherichia coli*, *Pseudomonas aeruginosa*, and *Staphylococcus aureus*. The PL spectra of the as-fabricated and annealed samples in Fig. 35(a) demonstrates a progressive enhancement in the intensity of the emission peaks with increasing annealing temperatures. Fig. 35(b) and (c) present the 3D surface plots of the PL spectra and an enlarged portion of Fig. 35(a), respectively, both demonstrating the enhanced emission peak intensity. The CIE plot of ZnSe NSs, in Fig. 35(d), shows all samples emit blue light. The sample annealed at 200 °C displays the strongest blue emission, highlighting that annealing improves this property. The antibacterial activity of P1 and P4 ZnSe samples is shown in Fig. 36(a–c). Fig. 36(d) and (e) presents a bar chart displaying the antimicrobial effectiveness of P1 and P4 against *Escherichia coli*, *Pseudomonas aeruginosa*, and *Staphylococcus aureus*. P1 (as-synthesized ZnSe NSs) was most effective against *Staphylococcus aureus*, with ZOI increasing with concentration. P4 exhibited activity against all three bacteria, with ZOI also increasing with concentration. The ZOI against *Pseudomonas aeruginosa* was higher than that against *Escherichia coli* and *Staphylococcus aureus*. These results indicate that annealed ZnSe nanostructures possess enhanced blue emission and improved antibacterial activity, suggesting their potential for applications in bioimaging and antibacterial treatments.

## 7. Conclusion

Zinc selenide (ZnSe), an intrinsic semiconductor characterized by a direct bandgap of 2.7 eV, has emerged as a highly renowned material for photocatalytic applications owing to its optimally aligned conduction band (CB) and valence band (VB) positions. Its versatility spans a wide array of domains, including wastewater treatment, environmental remediation, gas sensors, and energy conversion. Nevertheless, the practical employment of ZnSe is often hampered by intrinsic limitations such as rapid charge carrier recombination and structural instability. To address these challenges, various modification strategies, such as doping and heterojunction engineering, have been employed to augment its photocatalytic efficacy. The review particularly elaborates the Z-scheme heterojunctions, which have demonstrated superior capabilities in facilitating efficient charge separation and enhancing photocatalytic performance compared to conventional heterojunction systems. Integrating ZnSe with complementary semiconductor materials exhibiting suitable band edge alignments has proven highly effective in amplifying its photocatalytic efficacy. Additionally, core–shell heterostructures based on ZnSe have garnered attention for their ability to remarkably improve optoelectronic properties.

Beyond photocatalysis, ZnSe has showcased considerable promise in gas sensing applications, particularly for $NO_2$, $NH_3$, and acetone detection, although its potential for sensing other gases such as VOCs and $SO_2$ remains underexplored. Its intrinsic semiconducting nature, coupled with favourable surface chemistry and photo responsiveness, positions ZnSe as a compelling candidate for next-generation sensing technologies. ZnSe-based electrodes have also been extensively investigated for energy storage applications. Their well-developed porosity, nanoscale dimensions, and high electrical conductivity render them attractive materials for devices such as $Li^+$, $Na^+$, and $K^+$ ion batteries. Transition metal selenides, by virtue of their unique electronic structures and the high conductivity imparted by selenium atoms, exhibit remarkable electrochemical properties. Consequently, ZnSe has demonstrated significant potential as an anode material, offering high theoretical capacities and robust redox activity. However, despite outperforming analogous metal oxides in several respects, research on metal selenides, particularly for energy storage, remains relatively limited. Moreover, challenges such as volume expansion and cycling instability highlight the necessity for further structural optimization and hybridization with conductive matrices. Additionally, due to their exceptional fluorescence properties and inherent biocompatibility, ZnSe nanocrystals hold considerable promise for biomedical applications.[298,299]

In this context, the present review provides a comprehensive examination of the intrinsic attributes of ZnSe nanostructures, encompassing their structural, optical, and electronic properties. It further summarizes the various fabrication methodologies which have been instrumental in fine-tuning parameters like particle size, morphology, and crystallinity to optimize performance across diverse applications. Special emphasis is placed on the surface modification strategies, including elemental doping and the construction of heterostructures. This review not only highlights the pioneering advancements in ZnSe-based photocatalysts, with a particular focus on Z-scheme heterojunction systems, but also highlights the multifaceted applications of ZnSe nanomaterials. These include the photodegradation of dyes, antibiotics, phenolic contaminants, $CO_2$ reduction, Cr(VI) remediation, gas sensing, energy storage, and antimicrobial activity.

## 8. Limitations and future outlook

ZnSe nanostructures have garnered substantial research pursuit, primarily owing to their rich physicochemical properties and expansive scope of potential applications. Among inorganic semiconductors, ZnSe stands out for its diverse and intricate nanoscale morphologies. Over the past decade, considerable strides have been made in elucidating the fundamental properties of ZnSe-based nanostructures and identifying their key challenges, thereby enriching the scientific knowledge pool. However, these advances remain relatively modest compared to the extensive progress witnessed for more prevalent electronic and optoelectronic materials, such as ZnO nanostructures. Nevertheless, the distinctive properties, noteworthy recent progress, and broad functional prospects collectively affirm ZnSe nanostructures as compelling candidates for advanced technological applications. It is anticipated that a systematic exploration of the "synthesis–property–application" nexus will catalyze intensified research endeavours, not only to address the existing challenges but also to promote intense investigations into inorganic semiconductor nanostructures. Despite substantial advancements, several critical challenges must be addressed to facilitate the practical deployment of ZnSe-based systems:

(i) A paramount priority for future research is to enhance the long-term structural and operational stability of ZnSe materials under optimized conditions. While they exhibit exceptional photocatalytic performance, issues such as surface corrosion, structural degradation, and rapid charge carrier recombination can significantly deteriorate their efficacy over time. Strategies including the design of protective coatings, the introduction of novel dopants, or the development of composite matrices are imperative to augment environmental resilience without compromising multifunctionality. Such improvements are essential for realizing real-world applications.

(ii) Another critical aspect lies in scaling up of ZnSe production to meet industrial demands. Industrial process mainly relies on methods such as Bridgman–Stockbarger process, Molecular Beam Epitaxy (MBE), solution based methods (spin coating and dip coating), Chemical Vapour Deposition (CVD), and Physical Vapour Deposition (PVD).[300–302] However, each of these methods often faces challenges such as solution-based routes often produce lower crystalline quality. Similarly, ZnSe grown in CVD is prone to exhibits some defects such as tiny pores and impurities, due to raw material quality and limited growth control, and the advanced technology required for CVD significantly increase production cost.[303] Likewise, PVD also faces limitations such as requirement of high vacuum conditions, material volatilization at high temperature, defect formation. Therefore, future research should focus on cost-effective, scalable, and environmentally friendly synthesis strategies, such as green chemistry or continuous-flow production to enable large scale fabrication of high quality ZnSe materials suitable for commercial applications.

(iii) More rigorous investigations are necessary to correlate the photocatalytic performance with light absorption, surface architecture, particle size, morphology, and synthetic methodology of ZnSe-based nanocomposites.

(iv) Integration of ZnSe with advanced materials, such as graphene, carbon nanotubes, or conductive polymers, can dramatically elevate photocatalytic and electrochemical functionalities by improving the charge separation dynamics, increasing surface area, and extending light absorption spectra.

This would further broaden their utility in solar-driven environmental remediation, gas detection, and next-generation battery technologies.

(v) While ZnSe-based sensors have demonstrated promising sensitivity toward $NO_2$, investigations into their efficacy for detecting other analytes, such as VOCs (*e.g.*, formaldehyde, benzene) and $SO_2$, remain limited. Future efforts should explore innovative sensor architectures and surface functionalization to achieve improved selectivity, sensitivity, and rapid response across a diverse array of target gases.

(vi) Comprehensive mechanistic studies including elucidation of degradation pathways and photocatalytic kinetics under complex water matrices-are crucial for translating laboratory success into field applications. Density functional theory (DFT) simulations can provide atomic-level insights into the reaction mechanisms and evaluate the stability of the catalyst, thereby guiding the rational design of ZnSe-based systems. Also, advanced characterization techniques-such as *in situ* XRD, soft X-ray absorption spectroscopy, *in situ* TEM, *in situ* Raman spectroscopy, and neutron diffraction-can unravel dynamic processes and structural evolutions during catalysis.

(vii) Finally, environmental and toxicological assessment profiles of ZnSe-based hybrid materials are indispensable to ensure their safe and sustainable integration into practical technologies.

(viii) In energy storage, improving the structural integrity of ZnSe-based electrodes is crucial to mitigate issues such as volume changes and interfacial instability. Optimizing metal selenide electrodes through careful control of precursors, processing conditions, calcination parameters, porosity, and morphological and electrochemical attributes is essential. Nanostructuring, composite formation, and innovative electrode architectures hold promise for enhancing cycling stability and rate capability. Notably, ternary and multinary ZnSe-systems represent largely untapped avenues that could unlock superior electrochemical performance, akin to their well-studied metal oxide counterparts.

(ix) A deeper understanding of the interfacial behaviour, achieved through synergistic *in situ* experimental studies and theoretical modelling, will be vital for optimizing material design.

(x) A pivotal future direction for ZnSe-based gas sensors lies in engineering systems capable of high-performance operation at room temperature. Presently, many sensors necessitate elevated temperatures (>200 °C) to attain optimal sensitivity and rapid response, imposing significant energy demands that constrain their applicability, particularly in portable and wearable devices. Advancing this field will require the design of novel nanostructures and composite materials-leveraging techniques such as strategic doping, heterojunction integration, and activation *via* external stimuli like UV irradiation-to enable efficient low-temperature sensing. Such innovations will facilitate the development of energy-efficient, practical devices tailored for environmental monitoring and healthcare diagnostics.

(xi) Beyond achieving room-temperature operation, future research must prioritize enhancing the sensitivity and selectivity of ZnSe-based gas sensors, particularly for detecting low concentrations of hazardous gases such as $NO_2$, $NH_3$, and CO. Sensor sensitivity is intrinsically linked to tailored surface properties and material composition. Advanced doping approaches-including the incorporation of metals like Cu, Ni, and Pd-have demonstrated improvements in gas-sensing performance, though often with a trade-off between sensitivity and operating temperature dictated by dopant choice. Strategic introduction of novel dopants can modulate electronic structures, promoting faster charge carrier dynamics and more efficient gas adsorption. Additionally, exploring innovative dopant combinations and engineering heterojunction nanocomposites will be crucial for achieving superior sensitivity and selectivity. Such advancements will enable precise detection of trace gases, broadening applicability from industrial safety systems to urban environment monitoring.

(xii) Addressing the influence of environmental factors, particularly humidity, on the performance of gas sensor remains a critical challenge. Humidity can disrupt gas adsorption dynamics, compromising sensitivity and accuracy, especially in variable environments like outdoor air quality monitoring and industrial settings. Future research should prioritize the development of novel materials and hydrophobic coatings, as well as sensor architectures that limit water molecule interactions with active sensor surfaces, to enhance reliability under humid conditions. Additionally, deeper mechanistic insights into the influence of humidity on the sensing processes are essential for devising effective mitigation strategies.

(xiii) Advancing flexible, transparent, and portable gas sensors represents a compelling research frontier, propelled by the rise of wearable technologies and real-time environmental monitoring needs. Integrating ZnSe nanostructures into flexible substrates promises lightweight, robust, and highly sensitive devices. However, critical challenges persist in preserving sensor performance under mechanical stress, ensuring long-term durability, and maintaining stability amid fluctuations in humidity and temperature.

(xiv) Additionally, integrating gas sensors into wearable health monitoring devices holds immense promise for delivering personalized assessments of pollutant exposure, thereby advancing individualized health tracking. These emerging applications highlight the imperative for sustained innovation in sensor design, with a focus on miniaturization, energy efficiency, and seamless wireless integration.

Collectively, these advancements highlight the extraordinary multifaceted potential of ZnSe in tackling pressing environmental and technological imperatives, thereby charting a course for pioneering innovations in sustainable remediation, advanced sensing platforms, and next-generation energy storage systems.

## Abbreviation

| | |
|---|---|
| QDs | Quantum dots |
| EDTA | Ethlenediamine tetraacetic acid |
| MO | Methyl orange |
| SC | Semiconductor |

| | |
|---|---|
| CB | Conduction band |
| VB | Valence band |
| ASS | All-solid-state |
| MB | Methylene blue |
| AY 17 | Acid yellow 17 |
| RhB | Rhodamine B |
| CR | Congo red |
| MV | Methyl violet |
| SY | Sunset yellow |
| TC | Tetracycline |
| OTC | Oxytetracycline |
| RGO | Reduced graphene oxide |
| ZOI | Zones of inhibition |

## Conflicts of interest

There are no conflicts to declare.

## Data availability

No primary research results, software or code have been included and no new data were generated or analysed as part of this review.

## References

1 M. Anpo and M. Takeuchi, The design and development of highly reactive titanium oxide photocatalysts operating under visible light irradiation, *J. Catal.*, 2003, **216**, 505–516, DOI: 10.1016/S0021-9517(02)00104-5.

2 V. Gadore, S. R. Mishra and M. Ahmaruzzaman, Recent Developments in Transition Metal Selenide-Based Materials for Energy Storage, Conversion, Generation, Environmental Remediation, and Sensing, *J. Inorg. Organomet. Polym. Mater.*, 2024, **2024**, 1–36, DOI: 10.1007/S10904-024-03199-W.

3 H. P. Shivaraju, S. R. Yashas and R. Harini, Application of Mg-doped TiO2 coated buoyant clay hollow-spheres for photodegradation of organic pollutants in wastewater, *Mater. Today Proc.*, 2020, **27**, 1369–1374, DOI: 10.1016/J.MATPR.2020.02.754.

4 V. Gadore, S. Ranjan Mishra and M. Ahmaruzzaman, SnS2 modified carbonate-intercalated Ni-Zn-Fe trimetallic LDH as a novel photocatalyst for persulfate activation: Influence of operational parameters, co-existing ions and organic compounds, *Chem. Eng. J.*, 2023, **475**, 146157, DOI: 10.1016/J.CEJ.2023.146157.

5 S. Roy, J. Darabdhara and M. Ahmaruzzaman, Recent advances of Copper- BTC metal-organic frameworks for efficient degradation of organic dye-polluted wastewater: Synthesis, mechanistic insights and future outlook, *J. Hazard. Mater. Lett.*, 2024, **5**, 100094, DOI: 10.1016/J.HAZL.2023.100094.

6 S. Roy, S. R. Mishra, V. Gadore and M. Ahmaruzzaman, Harmonising light and structure: exploring ZnO/MOF composite photocatalysts for environmental remediations, *Int. J. Environ. Anal. Chem.*, 2024, 1–13, DOI: 10.1080/03067319.2024.2353904.

7 A. Bafana, S. S. Devi and T. Chakrabarti, Azo dyes: Past, present and the future, *Environ. Rev.*, 2011, **19**, 350–370, DOI: 10.1139/A11-018/ASSET/IMAGES/LARGE/A11-018F3.JPEG.

8 S. R. Mishra and M. Ahmaruzzaman, Cerium oxide and its nanocomposites: Structure, synthesis, and wastewater treatment applications, *Mater. Today Commun.*, 2021, **28**, 102562, DOI: 10.1016/J.MTCOMM.2021.102562.

9 B. T. T. Hien, V. T. Mai, P. T. Thuy, V. X. Hoa and T. T. K. Chi, Structural, Optical, and Photocatalytic Properties of ZnSe Nanoparticles Influenced by the Milling Time, *Crystallographica*, 2021, **11**, 1125, DOI: 10.3390/CRYST11091125.

10 T. Prakash, Review on nanostructured semiconductors for dye sensitized solar cells, Electron, *Mater. Lett.*, 2012, **8**, 231–243, DOI: 10.1007/S13391-012-1038-X/METRICS.

11 S. Roy, J. Darabdhara and M. Ahmaruzzaman, Sustainable degradation of pollutants, generation of electricity and hydrogen evolution via photocatalytic fuel cells: An Inclusive Review, *Environ. Res.*, 2023, **236**, 116702, DOI: 10.1016/J.ENVRES.2023.116702.

12 M. A. Rauf and S. S. Ashraf, Fundamental principles and application of heterogeneous photocatalytic degradation of dyes in solution, *Chem. Eng. J.*, 2009, **151**, 10–18, DOI: 10.1016/J.CEJ.2009.02.026.

13 A. Fujishima and K. Honda, Electrochemical Photolysis of Water at a Semiconductor Electrode, *Nature*, 1972, **238**(5358), 37–38, DOI: 10.1038/238037a0.

14 K. Nakata and A. Fujishima, TiO2 photocatalysis: Design and applications, *J. Photochem. Photobiol. C Photochem. Rev.*, 2012, **13**, 169–189, DOI: 10.1016/J.JPHOTOCHEMREV.2012.06.001.

15 V. Vimonses, S. Lei, B. Jin, C. W. K. Chow and C. Saint, Kinetic study and equilibrium isotherm analysis of Congo Red adsorption by clay materials, *Chem. Eng. J.*, 2009, **148**, 354–364, DOI: 10.1016/J.CEJ.2008.09.009.

16 H. W. P. Carvalho, A. P. L. Batista, R. Bertholdo, C. V. Santilli, S. H. Pulcinelli and T. C. Ramalho, Photocatalyst TiO2-Co: The effect of doping depth profile on methylene blue degradation, *J. Mater. Sci.*, 2010, **45**, 5698–5703, DOI: 10.1007/S10853-010-4639-5/FIGURES/6.

17 J. Yu, Y. Su and B. Cheng, Template-Free Fabrication and Enhanced Photocatalytic Activity of Hierarchical Macro-/Mesoporous Titania, *Adv. Funct. Mater.*, 2007, **17**, 1984–1990, DOI: 10.1002/ADFM.200600933.

18 Z. Wang, L. Yin, M. Zhang, G. Zhou, H. Fei, H. Shi and H. Dai, Synthesis and characterization of Ag3PO4/multiwalled carbon nanotube composite photocatalyst with enhanced photocatalytic activity and stability under visible light, *J. Mater. Sci.*, 2014, **49**, 1585–1593, DOI: 10.1007/S10853-013-7841-4/SCHEMES/1.

19 W. Yao, B. Zhang, C. Huang, C. Ma, X. Song and Q. Xu, Synthesis and characterization of high efficiency and stable Ag 3 PO 4/TiO 2 visible light photocatalyst for the degradation of methylene blue and rhodamine B

solutions, *J. Mater. Chem.*, 2012, **22**, 4050–4055, DOI: 10.1039/C2JM14410G.

20 L. Ren, L. Ma, L. Jin, J. B. Wang, M. Qiu and Y. Yu, Template-free synthesis of BiVO4 nanostructures: II. Relationship between various microstructures for monoclinicBiVO4 and their photocatalytic activity for the degradation of rhodamine B under visiblelight, *Nanotechnology*, 2009, **20**, 405602, DOI: 10.1088/0957-4484/20/40/405602.

21 M. L. Guan, D. K. Ma, S. W. Hu, Y. J. Chen and S. M. Huang, From hollow olive-shaped BiVO4 to n-p core-shell BiVO 4@Bi2O3 microspheres: Controlled synthesis and enhanced visible-light-responsive photocatalytic properties, *Inorg. Chem.*, 2011, **50**, 800–805, DOI: 10.1021/IC101961Z/SUPPL_FILE/IC101961Z_SI_001.PDF.

22 N. Zhang, S. Liu and Y. J. Xu, Recent progress on metal core@semiconductor shell nanocomposites as a promising type of photocatalyst, *Nanoscale*, 2012, **4**, 2227–2238, DOI: 10.1039/C2NR00009A.

23 Z. Tong, D. Yang, J. Shi, Y. Nan, Y. Sun and Z. Jiang, Three-Dimensional Porous Aerogel Constructed by g-C3N4 and Graphene Oxide Nanosheets with Excellent Visible-Light Photocatalytic Performance, *ACS Appl. Mater. Interfaces*, 2015, **7**, 25693–25701, DOI: 10.1021/ACSAMI.5B09503/SUPPL_FILE/AM5B09503_SI_001.PDF.

24 M. Xu, L. Han and S. Dong, Facile fabrication of highly efficient g-C3N4/Ag 2O heterostructured photocatalysts with enhanced visible-light photocatalytic activity, *ACS Appl. Mater. Interfaces*, 2013, **5**, 12533–12540, DOI: 10.1021/AM4038307/SUPPL_FILE/AM4038307_SI_001.PDF.

25 H. Cao, Y. Xiao and S. Zhang, The synthesis and photocatalytic activity of ZnSe microspheres, *Nanotechnology*, 2010, **22**, 015604, DOI: 10.1088/0957-4484/22/1/015604.

26 X. Wu, R. Xu, R. Zhu, R. Wu and B. Zhang, Converting 2D inorganic–organic ZnSe–DETA hybrid nanosheets into 3D hierarchical nanosheet-based ZnSe microspheres with enhanced visible-light-driven photocatalytic performances, *Nanoscale*, 2015, **7**, 9752–9759, DOI: 10.1039/C5NR02329G.

27 S. Venkatachalam, D. Mangalaraj, S. K. Narayandass, K. Kim and J. Yi, Structure, optical and electrical properties of ZnSe thin films, *Phys. B Condens. Matter*, 2005, **358**, 27–35, DOI: 10.1016/J.PHYSB.2004.12.022.

28 H. I. Elsaeedy, A. A. Hassan, H. A. Yakout and A. Qasem, The significant role of ZnSe layer thickness in optimizing the performance of ZnSe/CdTe solar cell for optoelectronic applications, *Opt. Laser Technol.*, 2021, **141**, 107139, DOI: 10.1016/J.OPTLASTEC.2021.107139.

29 F. Cao, W. Shi, L. Zhao, S. Song, J. Yang, Y. Lei and H. Zhang, Hydrothermal synthesis and high photocatalytic activity of 3D wurtzite ZnSe hierarchical nanostruetures, *J. Phys. Chem. C*, 2008, **112**, 17095–17101, DOI: 10.1021/JP8047345/SUPPL_FILE/JP8047345_SI_001.PDF.

30 Z. Mu, Q. Zheng, R. Liu, M. Wasim Iqbal Malik, D. Tang, W. Zhou, Q. Wan, Z. Mu, M. W. I Malik, Q. Wan, Q. Zheng, D. Tang, W. Zhou and R. Liu, 1D ZnSSe-ZnSe Axial Heterostructure and its Application for Photodetectors, *Adv. Electron. Mater.*, 2019, **5**, 1800770, DOI: 10.1002/AELM.201800770.

31 S. Park, S. Kim, G. J. Sun, D. B. Byeon, S. K. Hyun, W. I. Lee and C. Lee, ZnO-core/ZnSe-shell nanowire UV photodetector, *J. Alloys Compd.*, 2016, **658**, 459–464, DOI: 10.1016/J.JALLCOM.2015.10.247.

32 M. El-assar, T. E. Taha, F. E. A. El-Samie, H. A. Fayed and M. H. Aly, ZnSe-based highly-sensitive SPR biosensor for detection of different cancer cells and urine glucose levels, *Opt. Quant. Electron.*, 2023, **55**, 1–16, DOI: 10.1007/S11082-022-04326-Y/TABLES/2.

33 H. Okuyama, T. Miyajima, Y. Morinaga, F. Hiei, M. Ozawa and K. Akimoto, ZnSe/ZnMgSSe blue laser diode, *Electron. Lett.*, 1992, **28**, 1798–1799, DOI: 10.1049/EL:19921146.

34 K. Katayama, H. Matsubara, F. Nakanishi, T. Nakamura, H. Doi, A. Saegusa, T. Mitsui, T. Matsuoka, M. Irikura, T. Takebe, S. Nishine and T. Shirakawa, ZnSe-based white LEDs, *J. Cryst. Growth*, 2000, **214–215**, 1064–1070, DOI: 10.1016/S0022-0248(00)00275-X.

35 C. C. Kim and S. Sivananthan, Optical properties of ZnSe and its modeling, *Phys. Rev. B: Condens. Matter Mater. Phys.*, 1996, **53**, 1475, DOI: 10.1103/PhysRevB.53.1475.

36 Y. Fu, Z. Zhang, K. Du, Y. Qu, Q. Li and X. Yang, Spherical-like ZnSe with facile synthesis as a potential electrode material for lithium ion batteries, *Mater. Lett.*, 2015, **146**, 96–98, DOI: 10.1016/J.MATLET.2015.02.019.

37 C. Tang, X. Wei, X. Cai, Q. An, P. Hu, J. Sheng, J. Zhu, S. Chou, L. Wu and L. Mai, ZnSe Microsphere/Multiwalled Carbon Nanotube Composites as High-Rate and Long-Life Anodes for Sodium-Ion Batteries, *ACS Appl. Mater. Interfaces*, 2018, **10**, 19626–19632, DOI: 10.1021/ACSAMI.8B02819/ASSET/IMAGES/LARGE/AM-2018-028192_0006.JPEG.

38 D. Yeol Jo and S. K. Park, Facile strategy for synthesis of mesoporous ZnSe nanobelts coated with nitrogen-doped carbon as high-performance anodes for potassium-ion batteries, *Appl. Surf. Sci.*, 2023, **609**, 155278, DOI: 10.1016/J.APSUSC.2022.155278.

39 W. Liu, D. Gu and X. Li, Ultrasensitive NO2 Detection Utilizing Mesoporous ZnSe/ZnO Heterojunction-Based Chemiresistive-Type Sensors, *ACS Appl. Mater. Interfaces*, 2019, **11**, 29029–29040, DOI: 10.1021/ACSAMI.9B07263/ASSET/IMAGES/LARGE/AM9B07263_0007.JPEG.

40 N. Khalil, J. Yaqoob, M. U. Khan, H. A. Rizwan, A. Jabbar, R. Hussain, Z. Zafar, H. W. Darwish and F. Abbas, Exploring the potential of ZnSe nanocage as a promising tool for CO2 and SO2 sensing: A computational study, *J. Chem. Theor. Comput.*, 2024, **1231**, 114428, DOI: 10.1016/J.COMPTC.2023.114428.

41 C. C. Yang, Y. H. Yu, B. Van Der Linden, J. C. S. Wu and G. Mul, Artificial photosynthesis over crystalline TiO2-based catalysts: Fact or fiction?, *J. Am. Chem. Soc.*, 2010, **132**, 8398–8406, DOI: 10.1021/JA101318K/SUPPL_FILE/JA101318K_SI_002.PDF.

42 S. Rej, M. Bisetto, A. Naldoni and P. Fornasiero, Well-defined Cu 2 O photocatalysts for solar fuels and chemicals, *J. Mater. Chem. A*, 2021, **9**, 5915–5951, DOI: 10.1039/D0TA10181H.

43 S. Zeng, P. Kar, U. K. Thakur and K. Shankar, A review on photocatalytic CO2 reduction using perovskite oxide nanomaterials, *Nanotechnology*, 2018, **29**, 052001, DOI: 10.1088/1361-6528/AA9FB1.

44 Q. Zhang, H. Li, Y. Ma and T. Zhai, ZnSe nanostructures: Synthesis, properties and applications, *Prog. Mater. Sci.*, 2016, **83**, 472–535, DOI: 10.1016/J.PMATSCI.2016.07.005.

45 P. Zhou, M. Zhang, L. Wang, Q. Huang, Z. Su, L. Li, X. Wang, Y. Li, C. Zeng and Z. Guo, Synthesis and Electrochemical Performance of ZnSe Electrospinning Nanofibers as an Anode Material for Lithium Ion and Sodium Ion Batteries, *Front. Chem.*, 2019, **7**, 473780, DOI: 10.3389/FCHEM.2019.00569/BIBTEX.

46 A. R. Khataee, M. Hosseini, Y. Hanifehpour, M. Safarpour and S. W. Joo, Hydrothermal synthesis and characterization of Nd-doped ZnSe nanoparticles with enhanced visible light photocatalytic activity, *Res. Chem. Intermed.*, 2014, **40**, 495–508, DOI: 10.1007/S11164-012-0977-Z/TABLES/2.

47 C. Chen, B. Zhang, X. Fu and R. H. Liu, A novel polysaccharide isolated from mulberry fruits (Murus alba L.) and its selenide derivative: structural characterization and biological activities, *Food Funct.*, 2016, **7**, 2886–2897, DOI: 10.1039/C6FO00370B.

48 F. Chen, L. Hou, L. Zhu, C. Yang, F. Zhu, H. Qiu and S. Qin, Effects of selenide chitosan sulfate on glutathione system in hepatocytes and specific pathogen-free chickens, *Poult. Sci.*, 2020, **99**, 3979–3986, DOI: 10.1016/J.PSJ.2020.04.024.

49 A. Chauhan, A. Sudhaik, P. Raizada, A. A. P. Khan, A. Singh, Q. Van Le, V. H. Nguyen, T. Ahamad, S. Thakur, P. Singh and A. M. Asiri, Enhancement strategies for ZnSe based photocatalysts: Application to environmental remediation and energy conversion, *Process Saf. Environ. Prot.*, 2023, **170**, 415–435, DOI: 10.1016/J.PSEP.2022.12.017.

50 S. Dai, G. Feng, Y. Zhang, L. Deng, H. Zhang and S. Zhou, The effects of the impurity distribution on the electrical and optical properties of Cr2+:ZnSe nanowires: First-principles study, *Results Phys.*, 2018, **8**, 628–632, DOI: 10.1016/J.RINP.2017.12.075.

51 C. Y. Yeh, Z. W. Lu, S. Froyen and A. Zunger, Zinc-blende–wurtzite polytypism in semiconductors, *Phys. Rev. B: Condens. Matter Mater. Phys.*, 1992, **46**, 10086, DOI: 10.1103/PhysRevB.46.10086.

52 P. Reiss, ZnSe based colloidal nanocrystals: synthesis, shape control, core/shell, alloy and doped systems, *New J. Chem.*, 2007, **31**, 1843–1852, DOI: 10.1039/B712086A.

53 S. Acharya, A. B. Panda, S. Efrima, Y. Golan, A. B. Panda and S. Efrima, Polarization Properties and Switchable Assembly of Ultranarrow ZnSe Nanorods**, Commun, *Adv. Mater.*, 2007, **19**, 1105–1108, DOI: 10.1002/adma.200602057.

54 N. Chestnoy, R. Hull and L. E. Brus, Higher excited electronic states in clusters of ZnSe, CdSe, and ZnS: Spin-orbit, vibronic, and relaxation phenomena, *J. Chem. Phys.*, 1986, **85**, 2237–2242, DOI: 10.1063/1.451119.

55 A. Petris and G. Georgescu, Analysis of thickness influence on refractive index and absorption coefficient of zinc selenide thin films, *Opt. Express*, 2019, **27**(24), 34803–34823, DOI: 10.1364/OE.27.034803.

56 Z. Yu, Z. Xu, X. Wu and Z. Ma, Electronic structure and optical properties of ZnSe from first-principles calculations, *16th International Photonics and Optoelectronics Meetings*, 2014, p. JF2A.37, DOI: 10.1364/FBTA.2014.JF2A.37.

57 K. Kabita and B. I. Sharma, A theoretical study on the B3 phases of ZnSe: Structural and electronic properties, *Pramana–J. Phys.*, 2017, **89**, 1–4, DOI: 10.1007/S12043-017-1405-0/FIGURES/3.

58 J. M. Gonçalves, D. P. Rocha, M. N. T. Silva, P. R. Martins, E. Nossol, L. Angnes, C. Sekhar Rout and R. A. A. Munoz, Feasible strategies to promote the sensing performances of spinel MCo 2 O 4 (M = Ni, Fe, Mn, Cu and Zn) based electrochemical sensors: a review, *J. Mater. Chem. C*, 2021, **9**, 7852–7887, DOI: 10.1039/D1TC01550H.

59 J. Tarique, S. M. Sapuan, N. F. Aqil, A. Farhan, J. I. Faiz and S. Shahrizan, *A Comprehensive Review Based on Chitin and Chitosan Composites, Composites from the Aquatic Environment*, 2023, pp. 15–66, DOI: 10.1007/978-981-19-5327-9_1.

60 A. Sobhani and M. Salavati-Niasari, Transition metal selenides and diselenides: Hydrothermal fabrication, investigation of morphology, particle size and and their applications in photocatalyst, *Adv. Colloid Interface Sci.*, 2021, **287**, 102321, DOI: 10.1016/J.CIS.2020.102321.

61 E. D. Kolb and R. A. Laudise, Hydrothermal crystallization of Zinc selenide, *J. Cryst. Growth*, 1970, **7**, 199–202, DOI: 10.1016/0022-0248(70)90010-2.

62 Q. Liang, Y. Bai, L. Han, X. Deng, X. Wu, Z. Wang, X. Liu and J. Meng, Hydrothermal synthesis of ZnSe:Cu quantum dots and their luminescent mechanism study by first-principles, *J. Lumin.*, 2013, **143**, 185–192, DOI: 10.1016/J.JLUMIN.2013.04.032.

63 Y. L. Duan, S. L. Yao, C. Dai, X. H. Liu and G. F. Xu, Characterization of ZnSe microspheres synthesized under different hydrothermal conditions, *Trans. Nonferrous Met. Soc. China*, 2014, **24**, 2588–2597, DOI: 10.1016/S1003-6326(14)63387-2.

64 A. Sobhani and M. Salavati-Niasari, Optimized synthesis of ZnSe nanocrystals by hydrothermal method, *J. Mater. Sci. Mater. Electron.*, 2016, **27**, 293–303, DOI: 10.1007/S10854-015-3753-1/FIGURES/9.

65 S. Y. Bu, L. W. Li, P. Xie, H. Liu and S. L. Xue, Synthesis and optical properties of ZnSe micro-grasses and microspheres grown on graphene oxide sheets by the hydrothermal method, *Ceram. Int.*, 2016, **42**, 5075–5081, DOI: 10.1016/J.CERAMINT.2015.12.021.

66 S. Intachai, N. Khaorapapong and M. Ogawa, Hydrothermal synthesis of zinc selenide in smectites, *Appl. Clay Sci.*, 2017, **135**, 45–51, DOI: 10.1016/J.CLAY.2016.09.002.

67 I. F. Cruz, C. Freire, J. P. Araújo, C. Pereira and A. M. Pereira, Multifunctional Ferrite Nanoparticles: From Current Trends Toward the Future, *Magnetic Nanostructured Materials: From Lab to Fab*, 2018, pp. 59–116, DOI: 10.1016/B978-0-12-813904-2.00003-6.

68 S. Gupta and B. Hegde, Comparison of Co-precipitation and Hydrothermal Methods in the Preparation of Fe3O4@SiO2-Pro-Cu Nanocatalyst, *J. Synth. Chem.*, 2024, **3**, 287–300, DOI: 10.22034/JSC.2024.495390.1093.

69 A. J. Ahamed, K. Ramar and P. Vijaya Kumar, Synthesis and Characterization of ZnSe Nanoparticles by Co-precipitation Method, *J. Nanosci. Nanotechnol.*, 2016, **2**, 148–150. https://www.jacsdirectory.com/jnst.

70 M. Bigdeli Tabar, S. M. Elahi, M. Ghoranneviss and R. Yousefi, Controlled morphology of ZnSe nanostructures by varying Zn/Se molar ratio: the effects of different morphologies on optical properties and photocatalytic performance, *CrystEngComm*, 2018, **20**, 4590–4599, DOI: 10.1039/C8CE00775F.

71 A. Sanchez-Martinez, J. P. Ortiz-Beas, A. M. Huerta-Flores, E. R. López-Mena, J. Pérez-Álvarez and O. Ceballos-Sanchez, ZnSe nanoparticles prepared by coprecipitation method for photocatalytic applications, *Mater. Lett.*, 2021, **282**, 128702, DOI: 10.1016/J.MATLET.2020.128702.

72 V. Beena, S. Ajitha, S. L. Rayar, C. Parvathiraja, K. Kannan and G. Palani, Enhanced Photocatalytic and Antibacterial Activities of ZnSe Nanoparticles, *J. Inorg. Organomet. Polym. Mater.*, 2021, **31**, 4390–4401, DOI: 10.1007/S10904-021-02053-7/FIGURES/11.

73 P. Gupta, P. Patel, K. M. Sujata, P. K. Litoriya and R. G. Solanki, Facile synthesis and characterization of ZnSe nanoparticles, *Mater. Today Proc.*, 2023, **80**, 1556–1561, DOI: 10.1016/J.MATPR.2023.01.389.

74 T. A. Saleh, S. Majeed, A. Nayak and B. Bhushan, Principles and Advantages of Microwave-Assisted Methods for the Synthesis of Nanomaterials for Water Purification, *Advanced nanomaterials for water engineering, treatment, and hydraulics*, pp. 40–57, DOI: 10.4018/978-1-5225-2136-5.CH003.

75 A. M. Schwenke, S. Hoeppener and U. S. Schubert, Synthesis and Modification of Carbon Nanomaterials utilizing Microwave Heating, *Adv. Mater.*, 2015, **27**, 4113–4141, DOI: 10.1002/ADMA.201500472.

76 K. J. Rao, B. Vaidhyanathan, M. Ganguli and P. A. Ramakrishnan, Synthesis of inorganic solids using microwaves, *Chem. Mater.*, 1999, **11**, 882–895, DOI: 10.1021/CM9803859/ASSET/IMAGES/MEDIUM/CM9803859N00001.GIF.

77 D. S. Sofronov, E. M. Sofronova, V. V. Starikov, V. N. Baumer, P. V. Matejchenko, S. N. Galkin, A. I. Lalajants, A. G. Mamalis and S. N. Lavrynenko, Microwave synthesis of ZnSe, *J. Mater. Eng. Perform.*, 2013, **22**, 1637–1641, DOI: 10.1007/S11665-012-0454-2/FIGURES/8.

78 M. Shakir, S. K. Kushwaha, K. K. Maurya, G. Bhagavannarayana and M. A. Wahab, Characterization of ZnSe nanoparticles synthesized by microwave heating process, *Solid State Commun.*, 2009, **149**, 2047–2049, DOI: 10.1016/J.SSC.2009.08.021.

79 L. Huang and H. Han, One-step synthesis of water-soluble ZnSe quantum dots via microwave irradiation, *Mater. Lett.*, 2010, **64**, 1099–1101, DOI: 10.1016/J.MATLET.2010.02.026.

80 R. S. Chaurasiya and H. U. Hebbar, Reverse Micelles for Nanoparticle Synthesis and Biomolecule Separation, *Nanoscience in Food and Agriculture*, vol. 4, 2017, pp. 181–211, DOI: 10.1007/978-3-319-53112-0_5.

81 R. Savić, L. Luo, A. Eisenberg and D. Maysinger, Micellar nanocontainers distribute to defined cytoplasmic organelles, *Science*, 2003, **300**, 615–618, DOI: 10.1126/SCIENCE.1078192/SUPPL_FILE/SAVIC.PDF.

82 Y. Kakizawa and K. Kataoka, Block copolymer micelles for delivery of gene and related compounds, *Adv. Drug Deliv. Rev.*, 2002, **54**, 203–222, DOI: 10.1016/S0169-409X(02)00017-0.

83 A. G. Volkov, *Interfacial Catalysis*, 2002, DOI: 10.1201/9780203910429.

84 K. Holmberg, B. Jönsson, B. Kronberg and B. Lindman, *Polymers in Aqueous Solution*, Wiley-Blackwell, 2002.

85 Z. Lei, X. Wei, S. Bi and R. He, Reverse micelle synthesis and characterization of ZnSe nanoparticles, *Mater. Lett.*, 2008, **62**, 3694–3696, DOI: 10.1016/J.MATLET.2008.04.043.

86 D. Walsh, J. D. Hopwood and S. Mann, Crystal Tectonics: Construction of Reticulated Calcium Phosphate Frameworks in Bicontinuous Reverse Microemulsions, *Science*, 1994, **264**, 1576–1578, DOI: 10.1126/SCIENCE.264.5165.1576.

87 N. Zheng, Q. Wu, Y. Ding and Y. Li, Synthesis of BaCO3 Nanowires and Nanorods in the Presence of Different Nonionic W/O Microemulsions, *Chem. Lett.*, 2000, **29**, 638–639, DOI: 10.1246/CL.2000.638.

88 H. Shi, L. Qi, J. Ma, H. Cheng and B. Zhu, Synthesis of Hierarchical Superstructures Consisting of BaCrO4 Nanobelts in Catanionic Reverse Micelles, *Adv. Mater.*, 2003, **15**, 1647–1651, DOI: 10.1002/ADMA.200305625.

89 M. L. Arsene, I. Răut, M. Călin, M. L. Jecu, M. Doni and A. M. Gurban, Versatility of Reverse Micelles: From Biomimetic Models to Nano (Bio)Sensor Design, *Process*, 2021, **9**, 345, DOI: 10.3390/PR9020345.

90 F. Gu, Z. Wang, D. Han, G. Guo and H. Guo, Crystallization of rare earth carbonate nanostructures in the reverse micelle system, *Cryst. Growth Des.*, 2007, **7**, 1452–1458, DOI: 10.1021/CG060904H/ASSET/IMAGES/MEDIUM/CG060904HN00001.GIF.

91 P. Setua, A. Chakraborty, D. Seth, M. U. Bhatta, P. V. Satyam and N. Sarkar, Synthesis, optical properties, and surface enhanced Raman scattering of silver nanoparticles in nonaqueous methanol reverse micelles, *J. Phys. Chem. C*, 2007, **111**, 3901–3907, DOI: 10.1021/JP067475I/SUPPL_FILE/JP067475ISI20070107_054338.PDF.

92 J. Li, L. Shi, Y. An, Y. Li, X. Chen and H. Dong, Reverse micelles of star-block copolymer as nanoreactors for preparation of gold nanoparticles, *Polymer*, 2006, **47**, 8480–8487, DOI: 10.1016/J.POLYMER.2006.09.071.

93 F. T. Quinlan, J. Kuther, W. Tremel, W. Knoll, S. Risbud and P. Stroeve, Reverse micelle synthesis and characterization of ZnSe nanoparticles, *Langmuir*, 2000, **16**, 4049–4051, DOI: 10.1021/LA9909291/ASSET/LA9909291.FP.PNG_V03.

94 G. N. Karanikolos, P. Alexandridis, G. Itskos, A. Petrou and T. J. Mountziaris, Synthesis and Size Control of Luminescent ZnSe Nanocrystals by a Microemulsion- Gas Contacting Technique, *Langmuir*, 2004, **20**, 550–553.

95 H. Wang and F. Du, Hydrothermal synthesis of ZnSe hollow microspheres, *Cryst. Res. Technol.*, 2006, **41**, 323–327, DOI: 10.1002/CRAT.200510581.

96 A. Sobhani and M. Salavati-Niasari, Optimized synthesis of ZnSe nanocrystals by hydrothermal method, *J. Mater. Sci. Mater. Electron.*, 2016, **27**, 293–303, DOI: 10.1007/S10854-015-3753-1/FIGURES/9.

97 F. Mollaamin, S. Gharibe and M. Monajjemi, Synthesis of various nano and micro ZnSe morphologies by using hydrothermal method, *Int. J. Phys. Sci.*, 2011, **6**, 1496–1500.

98 H. Gong, H. Huang, M. Wang and K. Liu, Characterization and growth mechanism of ZnSe microspheres prepared by hydrothermal synthesis, *Ceram. Int.*, 2007, **33**, 1381–1384, DOI: 10.1016/J.CERAMINT.2006.03.033.

99 Q. Zeng, S. Xue, S. Wu, K. Gan, L. Xu, J. Han, W. Zhou and R. Zou, Synthesis and characterization of ZnSe rose-like nanoflowers and microspheres by the hydrothermal method, *Ceram. Int.*, 2014, **40**, 2847–2852, DOI: 10.1016/J.CERAMINT.2013.10.029.

100 L. Peng, Y. Wang, Q. Dong, Z. Wang and P. Znse, Passivated ZnSe nanocrystals prepared by hydrothermal methods and their optical properties, *Nano-Micro Lett.*, 2010, **23**(2), 190–196, DOI: 10.1007/BF03353640.

101 Z. Gao, S. Xue, Q. Yu, P. Xie, Y. Wang, H. Feng and L. Li, Synthesis, field emission of various ZnSe nanostructures by hydrothermal methods, *Micro & Nano Lett.*, 2017, **12**, 382–385, DOI: 10.1049/MNL.2016.0808.

102 J. P. Borah, J. Barman and K. C. Sarma, Structural and Optical Properties of ZnSe Nanoparticles, *Chalcogenide Lett.*, 2008, **5**, 201–208, DOI: 10.1166/JNN.2021.19114.

103 P. Gupta, P. Patel, K. M. Sujata and R. G. Solanki, Synthesis and characterization of ZnSe nanorods by coprecipitation method, *Mater. Today Proc.*, 2022, **66**, 1865–1869, DOI: 10.1016/J.MATPR.2022.05.411.

104 J. Che, X. Yao, H. Jian and M. Wang, Application and preparation of ZnSe nanometer powder by reduction process, *Ceram. Int.*, 2004, **30**, 1935–1938, DOI: 10.1016/J.CERAMINT.2003.12.190.

105 P. Gupta, R. G. Solanki, P. Patel and K. M. Sujata, Conversion of ZnSe nanorods to ZnSe/ZnO nanoparticles via air annealing, *MRS Adv.*, 2024, 1–10, DOI: 10.1557/S43580-024-00927-9/METRICS.

106 P. Gupta, R. G. Solanki, P. Patel, K. M. Sujata, R. Kumar and A. Pandit, Enhanced Antibacterial and Photoluminescence Activities of ZnSe Nanostructures, *ACS Omega*, 2023, **8**, 13670–13679, DOI: 10.1021/ACSOMEGA.2C07654/ASSET/IMAGES/LARGE/AO2C07654_0013.JPEG.

107 S. Sharma, M. A. Malik, T. Chandel, V. Thakur and P. Rajaram, Growth and characterization of ZnSe nanoparticles, *AIP Conf. Proc.*, 2014, **1591**, 474–476, DOI: 10.1063/1.4872644.

108 V. Beena, S. Ajitha, S. L. Rayar, C. Parvathiraja, K. Kannan and G. Palani, Enhanced Photocatalytic and Antibacterial Activities of ZnSe Nanoparticles, *J. Inorg. Organomet. Polym. Mater.*, 2021, **31**, 4390–4401, DOI: 10.1007/S10904-021-02053-7/FIGURES/11.

109 X. Li, X. Li, J. Wang, H. Zhai and X. Chen, Synthesis of ZnSe microdisks and nanobelts and their visible-light photocatalytic properties, *J. Mater. Sci.*, 2017, **52**, 3821–3830, DOI: 10.1007/S10853-016-0638-5/FIGURES/6.

110 S. L. Xue, S. X. Wu, Q. Z. Zeng, P. Xie, K. X. Gan, J. Wei, S. Y. Bu, X. N. Ye, L. Xie, R. J. Zou, C. M. Zhang and P. F. Zhu, Synthesis, field emission properties and optical properties of ZnSe nanoflowers, *Appl. Surf. Sci.*, 2016, **365**, 69–75, DOI: 10.1016/J.APSUSC.2016.01.022.

111 E. Mosquera, N. Carvajal, M. Morel and C. Marín, Fabrication of ZnSe nanoparticles: Structural, optical and Raman Studies, *J. Lumin.*, 2017, **192**, 814–817, DOI: 10.1016/J.JLUMIN.2017.08.017.

112 V. Adimule, S. Nandi, K. Sharma and R. Keri, Microstructure, zeta potential and enhanced photocatalytic dye degradation performances of mesoporous flower like Nb2O5@CeO2 bimetallic oxide nanomaterials decorated with reduced graphene oxide, *Inorg. Chem. Commun.*, 2024, **166**, 112592, DOI: 10.1016/J.INOCHE.2024.112592.

113 R. Muneer, M. R. Hashmet and P. Pourafshary, DLVO Modeling to Predict Critical Salt Concentration to Initiate Fines Migration Pre- and Post-Nanofluid Treatment in Sandstones, *SPE J.*, 2022, **27**, 1915–1929, DOI: 10.2118/209588-PA.

114 R. Muneer, M. R. Hashmet, P. Pourafshary and M. Shakeel, Unlocking the Power of Artificial Intelligence: Accurate Zeta Potential Prediction Using Machine Learning, *Nanomaterials*, 2023, **13**, 1209, DOI: 10.3390/NANO13071209/S1.

115 H. Setia, R. Gupta and R. K. Wanchoo, Stability of Nanofluids, *Mater. Sci. Forum*, 2013, **757**, 139–149, DOI: 10.4028/WWW.SCIENTIFIC.NET/MSF.757.139.

116 P. Sennett and J. P. Olivier, Colloidal dispersions, electrokinetic effects, and the concept of zeta potential, *Ind. Eng. Chem.*, 2002, **57**, 32–50, DOI: 10.1021/IE50668A007.

117 D. J. Pochapski, C. Carvalho Dos Santos, G. W. Leite, S. H. Pulcinelli and C. V. Santilli, Zeta Potential and Colloidal Stability Predictions for Inorganic Nanoparticle Dispersions: Effects of Experimental Conditions and Electrokinetic Models on the Interpretation of Results, *Langmuir*, 2021, **37**, 13379–13389, DOI: 10.1021/ACS.LANGMUIR.1C02056.

118 I. A. Mir, K. Rawat and H. B. Bohidar, Cadmium-free aqueous synthesis of ZnSe and ZnSe@ZnS core–shell quantum dots and their differential bioanalyte sensing potential, *Mater. Res. Express*, 2016, **3**, 105014, DOI: 10.1088/2053-1591/3/10/105014.

119 Z. Atef, F. Livani, F. Koohsar, R. Faridnia, G. Yadagiri and H. Kalani, Zinc selenide (ZnSe) nanoparticle coated with green seaweed (Ulva fasciata) hydroalcoholic extract as an anti-leishmanial compound on Leishmania major, *PLoS One*, 2025, **20**, e0321219, DOI: 10.1371/JOURNAL.PONE.0321219.

120 Y. Rajakarunanayake, R. H. Miles, G. Y. Wu and T. C. McGill, Band structure of ZnSe-ZnTe superlattices, *Phys. Rev. B: Condens. Matter Mater. Phys.*, 1988, **37**, 10212, DOI: 10.1103/PhysRevB.37.10212.

121 T. T. ThanhThuy, H. Feng and Q. Cai, Photocatalytic degradation of pentachlorophenol on ZnSe/TiO2 supported by photo-Fenton system, *Chem. Eng. J.*, 2013, **223**, 379–387, DOI: 10.1016/J.CEJ.2013.03.025.

122 M. F. Hasaneen, Z. A. Alrowaili and W. S. Mohamed, Structure and optical properties of polycrystalline ZnSe thin films: validity of Swanepol's approach for calculating the optical parameters, *Mater. Res. Express*, 2020, **7**, 016422, DOI: 10.1088/2053-1591/AB6779.

123 M. Wiegel, M. H. J. Emond, E. R. Stobbe and G. Blasse, Luminescence of alkali tantalates and niobates, *J. Phys. Chem. Solids*, 1994, **55**, 773–778, DOI: 10.1016/0022-3697(94)90030-2.

124 P. Chen, T. Y. Xiao, H. H. Li, J. J. Yang, Z. Wang, H. Bin Yao and S. H. Yu, Nitrogen-doped graphene/ZnSe nanocomposites: Hydrothermal synthesis and their enhanced electrochemical and photocatalytic activities, *ACS Nano*, 2012, **6**, 712–719, DOI: 10.1021/NN204191X/SUPPL_FILE/NN204191X_SI_001.PDF.

125 M. J. Kim, Y. I. Choi, S. W. Joo, M. Kang and Y. Sohn, Synthesis of Er and Yb-doped cubic and hexagonal phase ZnSe nano-assembled microspheres and their photocatalytic activities, *Ceram. Int.*, 2014, **40**, 16051–16059, DOI: 10.1016/J.CERAMINT.2014.07.141.

126 V. Beena, S. L. Rayar, S. Ajitha, A. Ahmad, F. J. Iftikhar, K. M. Abualnaja, T. S. Alomar, M. Ouladsmne and S. Ali, Photocatalytic Dye Degradation and Biological Activities of Cu-Doped ZnSe Nanoparticles and Their Insights, *Water*, 2021, **13**, 2561, DOI: 10.3390/W13182561.

127 J. Zhou and X. Wu, First-principles study on doping of tetragonal ZnSe monolayers, *Mater. Today Chem.*, 2017, **4**, 40–44, DOI: 10.1016/J.MTCHEM.2016.10.001.

128 C. J. Tong, H. Zhang, Y. N. Zhang, H. Liu and L. M. Liu, New manifold two-dimensional single-layer structures of zinc-blende compounds, *J. Mater. Chem. A*, 2014, **2**, 17971–17978, DOI: 10.1039/C4TA03944K.

129 A. R. Khataee, M. Hosseini, Y. Hanifehpour, M. Safarpour and S. W. Joo, Hydrothermal synthesis and characterization of Nd-doped ZnSe nanoparticles with enhanced visible light photocatalytic activity, *Res. Chem. Intermed.*, 2014, **40**, 495–508, DOI: 10.1007/S11164-012-0977-Z/TABLES/2.

130 L. Yang, J. Zhu and D. Xiao, Microemulsion-mediated hydrothermal synthesis of ZnSe and Fe-doped ZnSe quantum dots with different luminescence characteristics, *RSC Adv.*, 2012, **2**, 8179–8188, DOI: 10.1039/C2RA21401F.

131 F. Gong, L. Sun, H. Ruan and H. Cai, Hydrothermal synthesis and photoluminescence properties of Cu-doped ZnSe quantum dots using glutathione as stabilizer, *Mater. Express*, 2018, **8**, 173–181, DOI: 10.1166/MEX.2018.1418.

132 K. Yadav and N. Jaggi, Effect of Ag doping on structural and optical properties of ZnSe nanophosphors, *Mater. Sci. Semicond. Process.*, 2015, **30**, 376–380, DOI: 10.1016/J.MSSP.2014.09.044.

133 M. Chen, X. Cui, X. Xiao, Y. Xu, J. Cui, J. Guo, C. Liu and H. Guo, Mid-Infrared Emission of Transition Metal Co2+-Doped ZnSe Nanocrystals at Room Temperature via Hydrothermal Preparation, *ACS Appl. Nano Mater.*, 2019, **2**, 2844–2853, DOI: 10.1021/ACSANM.9B00307/ASSET/IMAGES/MEDIUM/AN-2019-00307E_0013.GIF.

134 M. Usama, M. Waqas, F. Ahmad, M. E. Mazhar, S. Atiq, R. Qaiser, M. Usman, M. Danish, N. Bano and R. Ahmad, Optimizing ZnSe nanorods with La doping for structural, electrical, and dielectric properties in device applications, *Surf. Interfaces*, 2024, **54**, 105275, DOI: 10.1016/J.SURFIN.2024.105275.

135 B. T. Huy, M. H. Seo, A. P. Kumar, H. Jeong and Y. I. Lee, Synthesis and photoluminescence of Cr-, Ni-, Co-, and Ti-doped ZnSe nanoparticles, *J. Alloys Compd.*, 2014, **588**, 127–132, DOI: 10.1016/J.JALLCOM.2013.11.015.

136 S. Yu and Y. Wu, Synthesis of Fe:ZnSe nanopowders via the co-precipitation method for processing transparent ceramics, *J. Am. Ceram. Soc.*, 2019, **102**, 7089–7097, DOI: 10.1111/JACE.16612.

137 V. Beena, S. L. Rayar, S. Ajitha, A. Ahmad, M. D. Albaqami, F. A. A. Alsabar and M. Sillanpää, Synthesis and Characterization of Sr-Doped ZnSe Nanoparticles for Catalytic and Biological Activities, *Water*, 2021, **13**, 2189, DOI: 10.3390/W13162189.

138 D. Subramanyam, B. Hymavathi and B. R. Kumar, Synthesis and Structural Characterization of Ni doped ZnSe Nanoparticles, *Int. J. Sci. Tech. Adv.*, 2019, **5**, 7–10.

139 S. J. Basha, V. Khidhirbrahmendra, J. Madhavi, U. S. U. Thampy, C. V. Reddy and R. V. S. S. N. Ravikumar, Structural, optical, magnetic and thermal investigations on Cr3+ ions doped ZnS nanocrystals by co-precipitation method, *J. Sci. Adv. Mater. Devices*, 2019, **4**, 260–266, DOI: 10.1016/J.JSAMD.2019.03.002.

140 K. Vinodgopal and P. V. Kamat, Enhanced Rates of Photocatalytic Degradation of an Azo Dye Using SnO2/TiO2 Coupled Semiconductor Thin Films, *Environ. Sci. Technol.*, 1995, **29**, 841–845, DOI: 10.1021/ES00003A037/ASSET/ES00003A037.FP.PNG_V03.

141 K. T. Ranjit and B. Viswanathan, Synthesis, characterization and photocatalytic properties of iron-doped TiO2 catalysts, *J. Photochem. Photobiol., A*, 1997, **108**, 79–84, DOI: 10.1016/S1010-6030(97)00005-1.

142 K. Prakruthi, M. P. Ujwal, S. R. Yashas, B. Mahesh, N. Kumara Swamy and H. P. Shivaraju, Recent advances in photocatalytic remediation of emerging organic pollutants using semiconducting metal oxides: an

overview, *Environ. Sci. Pollut. Res.*, 2021, **29**(4), 4930–4957, DOI: 10.1007/S11356-021-17361-1.

143 R. K. Paul and M. Ahmaruzzaman, Advanced photocatalytic degradation of POPs and other contaminants: a comprehensive review on nanocomposites and heterojunctions, *RSC Adv.*, 2025, **15**, 31313–31359, DOI: 10.1039/D5RA04336K.

144 H. Zhou, Y. Qu, T. Zeid and X. Duan, Towards highly efficient photocatalysts using semiconductor nanoarchitectures, *Energy Environ. Sci.*, 2012, **5**, 6732–6743, DOI: 10.1039/C2EE03447F.

145 J. Low, J. Yu, M. Jaroniec, S. Wageh and A. A. Al-Ghamdi, Heterojunction Photocatalysts, *Adv. Mater.*, 2017, **29**, 1601694, DOI: 10.1002/ADMA.201601694.

146 R. Marschall, Semiconductor Composites: Strategies for Enhancing Charge Carrier Separation to Improve Photocatalytic Activity, *Adv. Funct. Mater.*, 2014, **24**, 2421–2440, DOI: 10.1002/ADFM.201303214.

147 S. J. A. Moniz, S. A. Shevlin, D. J. Martin, Z. X. Guo and J. Tang, Visible-light driven heterojunction photocatalysts for water splitting – a critical review, *Energy Environ. Sci.*, 2015, **8**, 731–759, DOI: 10.1039/C4EE03271C.

148 J. K. Hyun, S. Zhang and L. J. Lauhon, Nanowire heterostructures, *Annu. Rev. Mater. Res.*, 2013, **43**, 451–479, DOI: 10.1146/ANNUREV-MATSCI-071312-121659/CITE/REFWORKS.

149 W. Shi and N. Chopra, Nanoscale heterostructures for photoelectrochemical water splitting and photodegradation of pollutants, *Nanomater. Energy*, 2013, **2**, 158–178, DOI: 10.1680/NME.13.00009.

150 S. Cho, J. W. Jang, J. Kim, J. S. Lee, W. Choi and K. H. Lee, Three-dimensional type II ZnO/ZnSe heterostructures and their visible light photocatalytic activities, *Langmuir*, 2011, **27**, 10243–10250, DOI: 10.1021/LA201755W/SUPPL_FILE/LA201755W_SI_001.PDF.

151 E. Sitara, H. Nasir, A. Mumtaz, M. F. Ehsan, M. Sohail, S. Iram, S. A. B. Bukhari, S. Ullah, T. Akhtar and A. Iqbal, Enhanced photoelectrochemical water splitting using zinc selenide/graphitic carbon nitride type-II heterojunction interface, *Int. J. Hydrogen Energy*, 2021, **46**, 25424–25435, DOI: 10.1016/J.IJHYDENE.2021.05.054.

152 R. Kumar, A. Sudhaik, A. A. P. Khan, P. Raizada, A. M. Asiri, S. Mohapatra, S. Thakur, V. K. Thakur and P. Singh, Current status on designing of dual Z-scheme photocatalysts for energy and environmental applications, *J. Ind. Eng. Chem.*, 2022, **106**, 340–355, DOI: 10.1016/J.JIEC.2021.11.008.

153 A. J. Bard, Photoelectrochemistry and heterogeneous photo-catalysis at semiconductors, *J. Photochem.*, 1979, **10**, 59–75, DOI: 10.1016/0047-2670(79)80037-4.

154 B. Zhu, P. Xia, Y. Li, W. Ho and J. Yu, Fabrication and photocatalytic activity enhanced mechanism of direct Z-scheme g-C3N4/Ag2WO4 photocatalyst, *Appl. Surf. Sci.*, 2017, **391**, 175–183, DOI: 10.1016/J.APSUSC.2016.07.104.

155 K. Maeda, Z-scheme water splitting using two different semiconductor photocatalysts, *ACS Catal.*, 2013, **3**, 1486–1503, DOI: 10.1021/CS4002089/ASSET/IMAGES/MEDIUM/CS-2013-002089_0029.GIF.

156 H. Tada, T. Mitsui, T. Kiyonaga, T. Akita and K. Tanaka, All-solid-state Z-scheme in CdS–Au–TiO2 three-component nanojunction system, *Nat. Mater.*, 2006, **5**(10), 782–786, DOI: 10.1038/nmat1734.

157 W. Zhang, A. R. Mohamed and W. J. Ong, Z-Scheme Photocatalytic Systems for Carbon Dioxide Reduction: Where Are We Now?, *Angew. Chem., Int. Ed.*, 2020, **59**, 22894–22915, DOI: 10.1002/ANIE.201914925.

158 L. Xie, T. Du, J. Wang, Y. Ma, Y. Ni, Z. Liu, L. Zhang, C. Yang and J. Wang, Recent advances on heterojunction-based photocatalysts for the degradation of persistent organic pollutants, *Chem. Eng. J.*, 2021, **426**, 130617, DOI: 10.1016/J.CEJ.2021.130617.

159 J. Yu, S. Wang, J. Low and W. Xiao, Enhanced photocatalytic performance of direct Z-scheme g-C 3 N 4 –TiO 2 photocatalysts for the decomposition of formaldehyde in air, *Phys. Chem. Chem. Phys.*, 2013, **15**, 16883–16890, DOI: 10.1039/C3CP53131G.

160 P. Zhou, J. Yu and M. Jaroniec, All-Solid-State Z-Scheme Photocatalytic Systems, *Adv. Mater.*, 2014, **26**, 4920–4935, DOI: 10.1002/ADMA.201400288.

161 H. Li, W. Tu, Y. Zhou and Z. Zou, Z-Scheme Photocatalytic Systems for Promoting Photocatalytic Performance: Recent Progress and Future Challenges, *Adv. Sci.*, 2016, **3**, 1500389, DOI: 10.1002/ADVS.201500389.

162 J. Low, C. Jiang, B. Cheng, S. Wageh, A. A. Al-Ghamdi and J. Yu, A Review of Direct Z-Scheme Photocatalysts, *Small Methods*, 2017, **1**, 1700080, DOI: 10.1002/SMTD.201700080.

163 J. Liu, B. Cheng and J. Yu, A new understanding of the photocatalytic mechanism of the direct Z-scheme g-C 3 N 4/TiO 2 heterostructure, *Phys. Chem. Chem. Phys.*, 2016, **18**, 31175–31183, DOI: 10.1039/C6CP06147H.

164 X. Li, H. Sun, Y. Xie, Y. Liang, X. Gong, P. Qin, L. Jiang, J. Guo, C. Liu and Z. Wu, Principles, synthesis and applications of dual Z-scheme photocatalysts, *Coord. Chem. Rev.*, 2022, **467**, 214596, DOI: 10.1016/J.CCR.2022.214596.

165 T. Liang, J. Wei, S. Zhang, J. Yang, J. Sun, Z. Li, Z. Li, Z. Yu, S. Wang and Y. Hou, Electron-buffer-mediated dual Z-scheme ZnSe/Ag2Se/AgBr heterojunction for efficient CO2 photocatalytic reduction, *J. Environ. Chem. Eng.*, 2023, **11**, 109686, DOI: 10.1016/J.JECE.2023.109686.

166 K. H. Kim and S. K. Ihm, Heterogeneous catalytic wet air oxidation of refractory organic pollutants in industrial wastewaters: A review, *J. Hazard. Mater.*, 2011, **186**, 16–34, DOI: 10.1016/J.JHAZMAT.2010.11.011.

167 E. Boelee, G. Geerling, B. van der Zaan, A. Blauw and A. D. Vethaak, Water and health: From environmental pressures to integrated responses, *Acta Trop.*, 2019, **193**, 217–226, DOI: 10.1016/J.ACTATROPICA.2019.03.011.

168 P. Borah, M. Kumar and P. Devi, Types of inorganic pollutants: metals/metalloids, acids, and organic forms, *Inorganic Pollutants in Water*, 2020, pp. 17–31, DOI: 10.1016/B978-0-12-818965-8.00002-0.

169 S. Gita, A. Hussan and T. G. Choudhury, Impact of textile dyes waste on aquatic environments and its treatment, *Environ. Ecol.*, 2017, **35**, 2349–2353.

170 W. Li, T. Li, G. Li, L. An, F. Li and Z. Zhang, Electrospun H4SiW12O40/cellulose acetate composite nanofibrous membrane for photocatalytic degradation of tetracycline and methyl orange with different mechanism, *Carbohydr. Polym.*, 2017, **168**, 153–162, DOI: 10.1016/J.CARBPOL.2017.03.079.

171 S. Zhang, B. Li, X. Wang, G. Zhao, B. Hu, Z. Lu, T. Wen, J. Chen and X. Wang, Recent developments of two-dimensional graphene-based composites in visible-light photocatalysis for eliminating persistent organic pollutants from wastewater, *Chem. Eng. J.*, 2020, **390**, 124642, DOI: 10.1016/J.CEJ.2020.124642.

172 R. Ma, S. Zhang, T. Wen, P. Gu, L. Li, G. Zhao, F. Niu, Q. Huang, Z. Tang and X. Wang, A critical review on visible-light-response CeO2-based photocatalysts with enhanced photooxidation of organic pollutants, *Catal. Today*, 2019, **335**, 20–30, DOI: 10.1016/J.CATTOD.2018.11.016.

173 D. Beydoun, R. Amal, G. Low and S. McEvoy, Role of nanoparticles in photocatalysis, *J. Nanoparticle Res.*, 1999, **1**, 439–458, DOI: 10.1023/A:1010044830871/METRICS.

174 M. Han, S. Zhu, S. Lu, Y. Song, T. Feng, S. Tao, J. Liu and B. Yang, Recent progress on the photocatalysis of carbon dots: Classification, mechanism and applications, *Nano Today*, 2018, **19**, 201–218, DOI: 10.1016/J.NANTOD.2018.02.008.

175 J. M. Poyatos, M. M. Muñio, M. C. Almecija, J. C. Torres, E. Hontoria and F. Osorio, Advanced oxidation processes for wastewater treatment: State of the art, *Water, Air, Soil Pollut.*, 2010, **205**, 187–204, DOI: 10.1007/S11270-009-0065-1/TABLES/1.

176 S. M. Rodríguez, Waste water treatment by advanced oxidation processes (solar photocatalysis in degradation of industrial contaminants), *Photoreactors Introduction Biodegradable Substances: Non-viable Air Stripping Bio-Treatment Ozone*, 2007.

177 J. M. Herrmann, Heterogeneous photocatalysis: fundamentals and applications to the removal of various types of aqueous pollutants, *Catal. Today*, 1999, **53**, 115–129, DOI: 10.1016/S0920-5861(99)00107-8.

178 S. H. Khan and B. Pathak, Zinc oxide based photocatalytic degradation of persistent pesticides: A comprehensive review, *Environ. Nanotechnol., Monit. Manage.*, 2020, **13**, 100290, DOI: 10.1016/J.ENMM.2020.100290.

179 C. S. Turchi and D. F. Ollis, Photocatalytic degradation of organic water contaminants: Mechanisms involving hydroxyl radical attack, *J. Catal.*, 1990, **122**, 178–192, DOI: 10.1016/0021-9517(90)90269-P.

180 C. J. Vörösmarty, P. B. McIntyre, M. O. Gessner, D. Dudgeon, A. Prusevich, P. Green, S. Glidden, S. E. Bunn, C. A. Sullivan, C. R. Liermann and P. M. Davies, Global threats to human water security and river biodiversity, *Nature*, 2010, **467**(7315), 555–561, DOI: 10.1038/nature09440.

181 H. Zeghioud, N. Khellaf, A. Amrane, H. Djelal, M. Bouhelassa, A. A. Assadi and S. Rtimi, Combining photocatalytic process and biological treatment for Reactive Green 12 degradation: optimization, mineralization, and phytotoxicity with seed germination, *Environ. Sci. Pollut. Res.*, 2021, **28**, 12490–12499, DOI: 10.1007/S11356-020-11282-1/FIGURES/10.

182 Z. Shen, Y. Zhou, Y. Guo, J. Zhao, J. Song, Y. Xie, Y. Ling and W. Zhang, Tuning the concentration of surface/bulk oxygen vacancies in CeO2 nanorods to promote highly efficient photodegradation of organic dyes, *Chin. Chem. Lett.*, 2021, **32**, 2524–2528, DOI: 10.1016/J.CCLET.2021.01.044.

183 S. Sakthivel, B. Neppolian, M. V. Shankar, B. Arabindoo, M. Palanichamy and V. Murugesan, Solar photocatalytic degradation of azo dye: comparison of photocatalytic efficiency of ZnO and TiO2, *Sol. Energy Mater. Sol. Cells*, 2003, **77**, 65–82, DOI: 10.1016/S0927-0248(02)00255-6.

184 H. Hidaka, J. Zhao, E. Pelizzetti and N. Serpone, Photodegradation of surfactants. 8. Comparison of photocatalytic processes between anionic sodium dodecylbenzenesulfonate and cationic benzyldodecyldimethylammonium chloride on the TiO2 surface, *J. Phys. Chem.*, 1992, **96**, 2226–2230.

185 I. M. Arabatzis, T. Stergiopoulos, M. C. Bernard, D. Labou, S. G. Neophytides and P. Falaras, Silver-modified titanium dioxide thin films for efficient photodegradation of methyl orange, *Appl. Catal., B*, 2003, **42**, 187–201, DOI: 10.1016/S0926-3373(02)00233-3.

186 A. N. Ökte and Ö. Yilmaz, Characteristics of lanthanum loaded TiO2-ZSM-5 photocatalysts: Decolorization and degradation processes of methyl orange, *Appl. Catal., A*, 2009, **354**, 132–142, DOI: 10.1016/J.APCATA.2008.11.022.

187 W. Zhang, Z. Yang, X. Wang, Y. Zhang, X. Wen and S. Yang, Large-scale synthesis of β-MnO2 nanorods and their rapid and efficient catalytic oxidation of methylene blue dye, *Catal. Commun.*, 2006, **7**, 408–412, DOI: 10.1016/J.CATCOM.2005.12.008.

188 S. H. Hsieh, W. J. Chen and T. H. Yeh, Effect of various amounts of graphene oxide on the degradation characteristics of the ZnSe/graphene nanocomposites, *Appl. Surf. Sci.*, 2015, **358**, 63–69, DOI: 10.1016/J.APSUSC.2015.08.220.

189 B. A. Bhat, L. Dubey, M. Sharma and N. Jadon, Facile hydrothermally synthesized ZnSe/FeSe2 metal chalcogenide heterostructure composite for rapid photocatalytic degradation of organic textile dyes, *Res. Chem. Intermed.*, 2024, **51**, 135–155, DOI: 10.1007/S11164-024-05439-7/FIGURES/2.

190 K. Yadav, M. Giri and N. Jaggi, Synthesis, characterization and photocatalytic studies of ZnSe and Ag:ZnSe nanoparticles, *Res. Chem. Intermed.*, 2015, **41**, 9967–9978, DOI: 10.1007/S11164-015-2002-9/FIGURES/10.

191 W. Shi, J. Shi, S. Yu and P. Liu, Ion-exchange synthesis and enhanced visible-light photocatalytic activities of CuSe-ZnSe flower-like nanocomposites, *Appl. Catal., B*, 2013, **138–139**, 184–190, DOI: 10.1016/J.APCATB.2013.02.031.

192 J. Xu, W. Wang, X. Zhang, X. Chang, Z. Shi and G. M. Haarberg, Electrodeposition of ZnSe thin film and its photocatalytic properties, *J. Alloys Compd.*, 2015, **632**, 778–782, DOI: 10.1016/J.JALLCOM.2015.01.013.

193 L. Zhu, M.-M. Peng, K. Y. Cho, S. Ye, S. Sarkar, K. Ullah, Z.-D. Meng and W.-C. Oh, Hydrothermal Synthesis, Characterization and Improved Activity of a Visible-Light-Driven ZnSe-Sensitized TiO 2 Composite Photocatalyst, *J. Korean Ceram. Soc.*, 2013, **50**, 504–509.

194 Y. Zhang, C. Hu, B. Feng, X. Wang and B. Wan, Synthesis and photocatalytic property of ZnSe flowerlike hierarchical structure, *Appl. Surf. Sci.*, 2011, **257**, 10679–10685, DOI: 10.1016/J.APSUSC.2011.07.078.

195 T. Gupta and R. P. Chauhan, Enhanced photocatalytic degradation of cationic dye using Cu-doped ZnSe, *Opt. Mater.*, 2023, **135**, 113295, DOI: 10.1016/J.OPTMAT.2022.113295.

196 M. F. Ehsan, S. Qudoos, Z. Ahmad, S. Hamid, M. Arfan, A. Zia, K. Umbreen, M. N. Ashiq and D. Tyagi, ZnTe/ZnSe heterostructures: In-situ synthesis, characterization and photocatalytic activity for Congo Red degradation, *SN Appl. Sci.*, 2019, **1**, 1–9, DOI: 10.1007/S42452-019-0220-2/FIGURES/7.

197 M. Zahra, G. Yasmeen, F. Aftab, H. R. Athar, A. Saleem, S. Ambreen and M. A. Malana, ZnSe-rGO nanocomposites as photocatalysts for purification of textile dye contaminated water: A green approach to use wastewater for maize cultivation, *Heliyon*, 2023, **9**, e22687, DOI: 10.1016/J.HELIYON.2023.E22687/ASSET/DA5C6384-AE8B-4288-8E0B-AEA9DA10A13C/MAIN.ASSETS/GR11.JPG.

198 S. Zhang, Saeeda, A. Khan, N. Ali, S. Malik, H. Khan, N. Ali, H. M. N. Iqbal and M. Bilal, Designing, characterization, and evaluation of chitosan-zinc selenide nanoparticles for visible-light-induced degradation of tartrazine and sunset yellow dyes, *Environ. Res.*, 2022, **213**, 113722, DOI: 10.1016/J.ENVRES.2022.113722.

199 M. Abdullah, S. I. Abbas Shah, S. Manzoor, N. Bano, S. Houda, M. Y. Ur Rehman, R. A. Alshgari, M. F. Ehsan and M. N. Ashiq, Synthesis of CoNi2O4/ZnSe nanocomposite for environmental cleaning under visible light irradiation, *Ceram. Int.*, 2024, **50**, 14397–14405, DOI: 10.1016/J.CERAMINT.2024.01.351.

200 F. Farahmandzadeh, E. Molahosseini, K. Kermanshian, A. Alimohammadi and M. Molaei, Treatment of water and effluents from methylene blue dye by using high-performance Fe3O4/rGO/ZnSe/TiO2 magnetic nanocomposite, *J. Mater. Sci. Mater. Electron.*, 2024, **35**, 1–11, DOI: 10.1007/S10854-024-13516-1/FIGURES/9.

201 Q. Yang, J. shi, J. Wei, S. Li and Y. He, Fabrication of Z-scheme ZnIn2S4/ZnSe heterostructed microspheres toward antibiotic degradation from real pharmaceutical wastewater, *Opt. Mater.*, 2024, **155**, 115905, DOI: 10.1016/J.OPTMAT.2024.115905.

202 S. Ghosh, S. Kar, T. Pal and S. Ghosh, Sunlight-driven photocatalytic degradation of Norfloxacin antibiotic in wastewater by ZnSe microsphere functionalized RGO composite, *Sustain. Chem. Environ.*, 2023, **4**, 100038, DOI: 10.1016/J.SCENV.2023.100038.

203 Y. Zhao, X. Liang, H. Shi, Y. Wang, Y. Ren, E. Liu, X. Zhang, J. Fan and X. Hu, Photocatalytic activity enhanced by synergistic effects of nano-silver and ZnSe quantum dots co-loaded with bulk g-C3N4 for Ceftriaxone sodium degradation in aquatic environment, *Chem. Eng. J.*, 2018, **353**, 56–68, DOI: 10.1016/J.CEJ.2018.07.109.

204 M. Liu, X. Hu, C. Zhang, M. Shafi, L. Ma, B. Lv, A. Rahim, M. Saleem and L. Zhao, Localized surface plasmon resonance enhanced charge transfer effect in MoO2/ZnSe nanocomposites enabling efficient SERS detection and visible light photocatalytic degradation, *Sens. Actuators, B*, 2024, **398**, 134688, DOI: 10.1016/J.SNB.2023.134688.

205 E. Sitara, M. F. Ehsan, H. Nasir, S. Iram and S. A. B. Bukhari, Synthesis, Characterization and Photocatalytic Activity of MoS2/ZnSe Heterostructures for the Degradation of Levofloxacin, *Catal*, 2020, **10**, 1380, DOI: 10.3390/CATAL10121380.

206 Z. Zheng, X. Li, L. Li and Y. Tang, Photoelectrocatalytic degradation of amoxicillin over quaternary ZnO/ZnSe/CdSe/MoS2 hierarchical nanorods, *Int. J. Hydrogen Energy*, 2019, **44**, 20826–20838, DOI: 10.1016/J.IJHYDENE.2018.06.150.

207 A. Fleming, The discovery of penicillin, *Br. Med. Bull.*, 1944, **2**, 4–5, DOI: 10.1093/OXFORDJOURNALS.BMB.A071032.

208 M. B. Ahmed, J. L. Zhou, H. H. Ngo and W. Guo, Adsorptive removal of antibiotics from water and wastewater: Progress and challenges, *Sci. Total Environ.*, 2015, **532**, 112–126, DOI: 10.1016/J.SCITOTENV.2015.05.130.

209 X. Liu, K. Lv, C. Deng, Z. Yu, J. Shi and A. C. Johnson, Persistence and migration of tetracycline, sulfonamide, fluoroquinolone, and macrolide antibiotics in streams using a simulated hydrodynamic system, *Environ. Pollut.*, 2019, **252**, 1532–1538, DOI: 10.1016/J.ENVPOL.2019.06.095.

210 S. Wu, Y. Lin and Y. H. Hu, Strategies of tuning catalysts for efficient photodegradation of antibiotics in water environments: a review, *J. Mater. Chem. A*, 2021, **9**, 2592–2611, DOI: 10.1039/D0TA09173A.

211 Y. Abhale, K. Patel, R. K. Paul, S. R. Mishra, S. Roy, M. Ahmaruzzaman, T. K. Ban, D. Kumar and S. Ghotekar, Novel bio-inspired fabrication of BiVO4 nanoparticles and their solar light-aided photocatalytic activity for metronidazole antibiotic degradation, *J. Sol-Gel Sci. Technol.*, 2025, **115**, 1580–1597, DOI: 10.1007/S10971-025-06872-9.

212 P. Das, A. Pan, K. Chakraborty, T. Pal and S. Ghosh, RGO-ZnSe Photocatalyst towards Solar-Light-Assisted Degradation of Tetracycline Antibiotic Water Pollutant, *ChemistrySelect*, 2018, **3**, 10214–10219, DOI: 10.1002/SLCT.201801657.

213 Y. Zhao, Y. Wang, H. Shi, E. Liu, J. Fan and X. Hu, Enhanced photocatalytic activity of ZnSe QDs/g-C3N4 composite for Ceftriaxone sodium degradation under visible light, *Mater. Lett.*, 2018, **231**, 150–153, DOI: 10.1016/J.MATLET.2018.08.034.

214 B. Liu, K. Cao, Z. Ma, X. Lu, J. Dang and Y. He, A novel 3D/3D S-scheme ZnSe/NiMoO4 heterostructure with significantly enhanced photocatalytic elimination efficiency for tetracycline from actual pharmaceutical wastewater, *J. Environ. Manage.*, 2025, **380**, 125024, DOI: 10.1016/J.JENVMAN.2025.125024.

215 E. Eriksson, A. Baun, P. S. Mikkelsen and A. Ledin, Risk assessment of xenobiotics in stormwater discharged to Harrestrup Å, Denmark, *Desalination*, 2007, **215**, 187–197, DOI: 10.1016/J.DESAL.2006.12.008.

216 S. Ahmed, M. G. Rasul, W. N. Martens, R. Brown and M. A. Hashib, Heterogeneous photocatalytic degradation of phenols in wastewater: A review on current status and developments, *Desalination*, 2010, **261**, 3–18, DOI: 10.1016/J.DESAL.2010.04.062.

217 I. Assadullah, J. H. Malik, A. Shafi and R. Tomar, Growth of crystalline WO3-ZnSe nanocomposites: an approach to optical, electrochemical, and catalytic properties, *Sci. Rep.*, 2022, **12**, 1–12, DOI: 10.1038/S41598-022-07951-5.

218 A. Kumar, M. Naushad, A. Rana, P. Inamuddin, G. Sharma, A. A. Ghfar, F. J. Stadler and M. R. Khan, ZnSe-WO3 nano-hetero-assembly stacked on Gum ghatti for photo-degradative removal of Bisphenol A: Symbiose of adsorption and photocatalysis, *Int. J. Biol. Macromol.*, 2017, **104**, 1172–1184, DOI: 10.1016/J.IJBIOMAC.2017.06.116.

219 K. Chakraborty, S. Chakrabarty, T. Pal and S. Ghosh, Synergistic effect of zinc selenide–reduced graphene oxide towards enhanced solar light-responsive photocurrent generation and photocatalytic 4-nitrophenol degradation, *New J. Chem.*, 2017, **41**, 4662–4671, DOI: 10.1039/C6NJ04022E.

220 J. Cao, J. He, J. Ye, K. Ge, Y. Zhang and Y. Yang, Urchin-Like Bi2S3/Ag Nanostructures for Photocatalytic Reduction of Cr(VI), *ACS Appl. Nano Mater.*, 2021, **4**, 1260–1269, DOI: 10.1021/ACSANM.0C02858/ASSET/IMAGES/LARGE/AN0C02858_0011.JPEG.

221 L. Qiu, Y. Wang, X. Zhang, F. Tian, C. Zhu, J. Sheng, W. Yang and Y. Yu, ZnS Nanospheres Coated with ZnSe/MoSe2 Shells as Dual Heterojunctions with Wide Spectral Responses for the Photoreduction of Cr(VI), *ACS Appl. Nano Mater.*, 2023, **6**, 523–532, DOI: 10.1021/ACSANM.2C04639/ASSET/IMAGES/LARGE/AN2C04639_0008.JPEG.

222 S. Z. Alsheheri, A. Shawky, W. T. Alsaggaf and Z. I. Zaki, Visible-light responsive ZnSe-anchored mesoporous TiO2 heterostructures for boosted photocatalytic reduction of Cr(VI), *Nanotechnology*, 2022, **33**, 305701, DOI: 10.1088/1361-6528/AC6816.

223 B. Feng, J. Cao, D. Han, H. Liang, S. Yang, X. Li and J. Yang, ZnSe nanoparticles of different sizes: Optical and photocatalytic properties, *Mater. Sci. Semicond. Process.*, 2014, **27**, 865–872, DOI: 10.1016/J.MSSP.2014.08.027.

224 J. Yin, C. Yang, X. Yang, S. Wang, H. Zhang, S. Zhou and G. Feng, Fabrication and Photocatalytic Properties of ZnSe Nanorod Films, *J. Nanomater.*, 2016, **2016**, 1738608, DOI: 10.1155/2016/1738608.

225 J. Zhang, P. Zhao, Y. Li, Y. Cao, T. Xie, Y. Lin and Z. Mu, Insight into enhanced visible-light-driven Cr(VI) reduction with ZnO/ZnSe hierarchical n-p heterojunction, *Chem. Phys. Lett.*, 2021, **762**, 138157, DOI: 10.1016/J.CPLETT.2020.138157.

226 Q. Yu, Y. Liu, Q. Zeng, Y. Yang, S. Ning, Y. Wei, X. Wang and D. Zeng, Efficient photocatalytic H2 production and Cr(VI) reduction using a Cu2-xSe/ZnSe heterojunction, *J. Alloys Compd.*, 2025, **1014**, 178810, DOI: 10.1016/J.JALLCOM.2025.178810.

227 Z. Ren, X. Liu, Z. Zhuge, Y. Gong and C. Q. Sun, MoSe2/ZnO/ZnSe hybrids for efficient Cr(VI) reduction under visible light irradiation, *Chin. J. Catal.*, 2020, **41**, 180–187, DOI: 10.1016/S1872-2067(19)63484-4.

228 C. Pasten and J. C. Santamarina, Energy and quality of life, *Energy Policy*, 2012, **49**, 468–476, DOI: 10.1016/J.ENPOL.2012.06.051.

229 Y. N. Li, R. Ma, L. N. He and Z. F. Diao, Homogeneous hydrogenation of carbon dioxide to methanol, *Catal. Sci. Technol.*, 2014, **4**, 1498–1512, DOI: 10.1039/C3CY00564J.

230 Q. Lu and F. Jiao, Electrochemical CO2 reduction: Electrocatalyst, reaction mechanism, and process engineering, *Nano Energy*, 2016, **29**, 439–456, DOI: 10.1016/J.NANOEN.2016.04.009.

231 T. Inoue, A. Fujishima, S. Konishi and K. Honda, Photoelectrocatalytic reduction of carbon dioxide in aqueous suspensions of semiconductor powders, *Nature*, 1979, **277**(5698), 637–638, DOI: 10.1038/277637a0.

232 P. Li and T. He, Recent advances in zinc chalcogenide-based nanocatalysts for photocatalytic reduction of CO 2, *J. Mater. Chem. A*, 2021, **9**, 23364–23381, DOI: 10.1039/D1TA05365E.

233 S. Zhang, X. Yin and Y. Zheng, Enhanced photocatalytic reduction of CO2 to methanol by ZnO nanoparticles deposited on ZnSe nanosheet, *Chem. Phys. Lett.*, 2018, **693**, 170–175, DOI: 10.1016/J.CPLETT.2018.01.018.

234 H. Charles, P. J. Chengula, H. Oh and C. S. Lee, Construction of highly porous Z-scheme CuSe2/ZnSe heterostructure to achieve efficient CO2 photoreduction activity, *Surf. Interfaces*, 2024, **52**, 104838, DOI: 10.1016/J.SURFIN.2024.104838.

235 O. C. Qomaruddin, H. S. Wasisto, A. Waag, J. D. Prades and C. Fàbrega, Visible-Light-Driven Room Temperature NO2 Gas Sensor Based on Localized Surface Plasmon Resonance: The Case of Gold Nanoparticle Decorated Zinc Oxide Nanorods (ZnO NRs), *Chemosens*, 2022, **10**, 28, DOI: 10.3390/CHEMOSENSORS10010028.

236 X. Ren, Z. Xu, D. Liu, Y. Li, Z. Zhang and Z. Tang, Conductometric NO2 gas sensors based on MOF-derived porous ZnO nanoparticles, *Sens. Actuators, B*, 2022, **357**, 131384, DOI: 10.1016/J.SNB.2022.131384.

237 S. Park, S. Kim, W. I. Lee, K. K. Kim and C. Lee, Room temperature, ppb-level NO2 gas sensing of multiple-networked ZnSe nanowire sensors under UV illumination, *Beilstein J. Nanotechnol.*, 2014, **5194**(5), 1836–1841, DOI: 10.3762/BJNANO.5.194.

238 W. Liu, D. Gu and X. Li, Detection of Ppb-level NO2 using mesoporous ZnSe/SnO2 core-shell microspheres based chemical sensors, *Sens. Actuators, B*, 2020, **320**, 128365, DOI: 10.1016/J.SNB.2020.128365.

239 R. Abimaheshwari, R. Abinaya, M. Navaneethan and S. Harish, Enhanced sensitivity and selectivity of ZnSe/PANI nanocomposite for Low-ppm NO2 detection at room temperature gas sensor application, *Surf. Interfaces*, 2024, **55**, 105295, DOI: 10.1016/J.SURFIN.2024.105295.

240 R. Gao, T. Zhang, X. Zhang, S. Gao, Y. Xu, X. Cheng, J. Gao, M. Zheng, X. Zhou and L. Huo, One-step controlled synthesis of ZnO-ZnSe hollow nanospheres with surface defects for selective detection of NO2, *Appl. Surf. Sci.*, 2023, **635**, 157628, DOI: 10.1016/J.APSUSC.2023.157628.

241 S. Singh, I. S. Saggu, S. Singh, N. Kumar, K. Chen, Z. Xuan, R. Gupta, M. T. Swihart and S. Sharma, Detection of DMF and NH3 at Room Temperature Using a Sensor Based on a MoS2/Single-Walled Carbon Nanotube Composite, *ACS Appl. Nano Mater.*, 2023, **6**, 10698–10712, DOI: 10.1021/ACSANM.3C01638/ASSET/IMAGES/LARGE/AN3C01638_0009.JPEG.

242 S. Singh, J. Deb, U. Sarkar and S. Sharma, MoSe2/multiwalled carbon nanotube composite for ammonia sensing in natural humid environment, *J. Hazard. Mater.*, 2022, **435**, 128821, DOI: 10.1016/J.JHAZMAT.2022.128821.

243 R. Thayil and S. R. Parne, Tuning ZnSe nanostructures for enhanced ammonia sensing at room temperature, *Mater. Lett.*, 2024, **371**, 136919, DOI: 10.1016/J.MATLET.2024.136919.

244 Z. Zhu, Z. Li, X. Xiong, X. Hu, X. Wang, N. Li, T. Jin and Y. Chen, ZnO/ZnSe heterojunction nanocomposites with oxygen vacancies for acetone sensing, *J. Alloys Compd.*, 2022, **906**, 164316, DOI: 10.1016/J.JALLCOM.2022.164316.

245 H. M. Saraoğlu and M. Koçan, Determination of Blood Glucose Level-Based Breath Analysis by a Quartz Crystal Microbalance Sensor Array, *IEEE Sens. J.*, 2010, **10**, 104–109, DOI: 10.1109/JSEN.2009.2035769.

246 M. Storer, J. Dummer, H. Lunt, J. Scotter, F. McCartin, J. Cook, M. Swanney, D. Kendall, F. Logan and M. Epton, Measurement of breath acetone concentrations by selected ion flow tube mass spectrometry in type 2 Diabetes, *J. Breath Res.*, 2011, **5**, 046011, DOI: 10.1088/1752-7155/5/4/046011.

247 R. Vasumathi, K. C. Lalithambika, D. Balamurugan, A. Thayumanavan, P. Neelamegam and S. Sriram, Adsorption effect of SO 2 and CO 2 gas molecules on ZnSe nanotube devices: first principles analysis, *J. Comput. Electron.*, 2018, **17**, 304–312, DOI: 10.1007/S10825-017-1091-7/FIGURES/7.

248 M. R. Allen, D. J. Frame, C. Huntingford, C. D. Jones, J. A. Lowe, M. Meinshausen and N. Meinshausen, Warming caused by cumulative carbon emissions towards the trillionth tonne, *Nature*, 2009, **458**, 1163–1166, DOI: 10.1038/NATURE08019;KWRD=SCIENCE.

249 E. Salih and A. I. Ayesh, Sensitive SO2 gas sensor utilizing Pt-doped graphene nanoribbon: First principles investigation, *Mater. Chem. Phys.*, 2021, **267**, 124695, DOI: 10.1016/J.MATCHEMPHYS.2021.124695.

250 V. Galstyan, J. M. Macak and T. Djenizian, Anodic TiO2 nanotubes: A promising material for energy conversion and storage, *Appl. Mater. Today*, 2022, **29**, 101613, DOI: 10.1016/J.APMT.2022.101613.

251 C. Kuru, D. Choi, A. Kargar, C. H. Liu, S. Yavuz, C. Choi, S. Jin and P. R. Bandaru, High-performance flexible hydrogen sensor made of WS2 nanosheet–Pd nanoparticle composite film, *Nanotechnology*, 2016, **27**, 195501, DOI: 10.1088/0957-4484/27/19/195501.

252 J. B. Goodenough and K. S. Park, The Li-ion rechargeable battery: A perspective, *J. Am. Chem. Soc.*, 2013, **135**, 1167–1176, DOI: 10.1021/JA3091438/ASSET/IMAGES/JA-2012-091438_M014.GIF.

253 W. Ni, X. Li, L. Y. Shi and J. Ma, Research progress on ZnSe and ZnTe anodes for rechargeable batteries, *Nanoscale*, 2022, **14**, 9609–9635, DOI: 10.1039/D2NR02366K.

254 A. R. Park, K. J. Jeon and C. M. Park, Electrochemical mechanism of Li insertion/extraction in ZnS and ZnS/C anodes for Li-ion batteries, *Electrochim. Acta*, 2018, **265**, 107–114, DOI: 10.1016/J.ELECTACTA.2018.01.158.

255 L. He, X. Z. Liao, K. Yang, Y. S. He, W. Wen and Z. F. Ma, Electrochemical characteristics and intercalation mechanism of ZnS/C composite as anode active material for lithium-ion batteries, *Electrochim. Acta*, 2011, **56**, 1213–1218, DOI: 10.1016/J.ELECTACTA.2010.11.014.

256 L. Wang, G. Zhang, Q. Liu and H. Duan, Recent progress in Zn-based anodes for advanced lithium ion batteries, *Mater. Chem. Front.*, 2018, **2**, 1414–1435, DOI: 10.1039/C8QM00125A.

257 Y. N. Zhou, W. J. Li and Z. W. Fu, Electrochemical reactivity of nanocomposite ZnO–Se for lithium-ion batteries, *Electrochim. Acta*, 2012, **59**, 435–440, DOI: 10.1016/J.ELECTACTA.2011.10.093.

258 H. T. Kwon and C. M. Park, Electrochemical characteristics of ZnSe and its nanostructured composite for rechargeable Li-ion batteries, *J. Power Sources*, 2014, **251**, 319–324, DOI: 10.1016/J.JPOWSOUR.2013.11.033.

259 X. Cao, A. Li, Y. Yang and J. Chen, ZnSe nanoparticles dispersed in reduced graphene oxides with enhanced electrochemical properties in lithium/sodium ion batteries, *RSC Adv.*, 2018, **8**, 25734–25744, DOI: 10.1039/C8RA03479F.

260 M. Z. Xue and Z. W. Fu, Fabrication and electrochemical characterization of zinc selenide thin film by pulsed laser deposition, *Electrochim. Acta*, 2006, **52**, 988–995, DOI: 10.1016/J.ELECTACTA.2006.06.036.

261 D. Chen, W. Chen, L. Ma, G. Ji, K. Chang and J. Y. Lee, Graphene-like layered metal dichalcogenide/graphene composites: synthesis and applications in energy storage and conversion, *Mater. Today*, 2014, **17**, 184–193, DOI: 10.1016/J.MATTOD.2014.04.001.

262 Z. Zhang, Y. Fu, X. Yang, Y. Qu and Q. Li, Nanostructured ZnSe Anchored on Graphene Nanosheets with Superior Electrochemical Properties for Lithium ion Batteries,

*Electrochim. Acta*, 2015, **168**, 285–291, DOI: 10.1016/J.ELECTACTA.2015.04.025.

263 X. Liu, Y. Liu, M. Feng and L. Z. Fan, MOF-derived and nitrogen-doped ZnSe polyhedra encapsulated by reduced graphene oxide as the anode for lithium and sodium storage, *J. Mater. Chem. A*, 2018, **6**, 23621–23627, DOI: 10.1039/C8TA09247H.

264 Q. Liu, J. Hou, Q. Hao, P. Huang, C. Xu, Q. Zhou, J. Zhou and H. Liu, Nitrogen-doped carbon encapsulated hollow ZnSe/CoSe 2 nanospheres as high performance anodes for lithium-ion batteries, *Nanoscale*, 2020, **12**, 22778–22786, DOI: 10.1039/D0NR05789D.

265 H. Zhang, J. Li, Y. Zhu, X. Zeng, C. Chen, H. Zhang and J. Liu, In-situ embedding silicon nanoparticles into three-dimensional ZnSe/CoSe composites with carbon shell enables high-performance lithium-ion battery anode, *J. Alloys Compd.*, 2025, **1013**, 178554, DOI: 10.1016/J.JALLCOM.2025.178554.

266 L. Zhu, Z. Wang, L. Wang, L. Xie, J. Li and X. Cao, ZnSe embedded in N-doped carbon nanocubes as anode materials for high-performance Li-ion batteries, *Chem. Eng. J.*, 2019, **364**, 503–513, DOI: 10.1016/J.CEJ.2019.01.191.

267 H. Liu, Z. Li, L. Zhang, H. Ruan and R. Hu, MOF-Derived ZnSe/N-Doped Carbon Composites for Lithium-Ion Batteries with Enhanced Capacity and Cycling Life, *Nanoscale Res. Lett.*, 2019, **14**, 1–10, DOI: 10.1186/S11671-019-3055-2/FIGURES/6.

268 Z. Chen, R. Wu, H. Wang, K. H. L. Zhang, Y. Song, F. Wu, F. Fang and D. Sun, Embedding ZnSe nanodots in nitrogen-doped hollow carbon architectures for superior lithium storage, *Nano Res.*, 2018, **11**, 966–978, DOI: 10.1007/S12274-017-1709-X/METRICS.

269 Z. Wang, X. Cao, P. Ge, L. Zhu, L. Xie, H. Hou, X. Qiu and X. Ji, Hollow-sphere ZnSe wrapped around carbon particles as a cycle-stable and high-rate anode material for reversible Li-ion batteries, *New J. Chem.*, 2017, **41**, 6693–6699, DOI: 10.1039/C7NJ01230F.

270 X. Hu, X. Liu, K. Chen, G. Wang and H. Wang, Core–shell MOF-derived N-doped yolk–shell carbon nanocages homogenously filled with ZnSe and CoSe 2 nanodots as excellent anode materials for lithium- and sodium-ion batteries, *J. Mater. Chem. A*, 2019, **7**, 11016–11037, DOI: 10.1039/C9TA01999E.

271 K. Wang, Y. Wang, Y. Zhang, F. Liu, J. Shi, S. Liu, X. Xie, G. Cao and A. Pan, Bimetallic organic framework derivation of three-dimensional and heterogeneous metal selenides/carbon composites as advanced anodes for lithium-ion batteries, *Nanoscale*, 2020, **12**, 12623–12631, DOI: 10.1039/D0NR01528H.

272 Y. Zhang, B. Han, S. Tan, Q. Gao, Z. Cai, C. Zhou, J. Li, R. Sun and K. Amine, Interfacial Engineering of Metal Chalcogenides-based Heterostructures for Advanced Sodium-Ion Batteries, *Adv. Energy Mater.*, 2025, **15**, 2404796, DOI: 10.1002/AENM.202404796.

273 Y. Li, F. Wu and S. Xiong, Embedding ZnSe nanoparticles in a porous nitrogen-doped carbon framework for efficient sodium storage, *Electrochim. Acta*, 2019, **296**, 582–589, DOI: 10.1016/J.ELECTACTA.2018.11.059.

274 S. Lu, T. Zhu, H. Wu, Y. Wang, J. Li, A. Abdelkader, K. Xi, W. Wang, Y. Li, S. Ding, G. Gao and R. V. Kumar, Construction of ultrafine ZnSe nanoparticles on/in amorphous carbon hollow nanospheres with high-power-density sodium storage, *Nano Energy*, 2019, **59**, 762–772, DOI: 10.1016/J.NANOEN.2019.03.008.

275 S. Men, H. Zheng, D. Ma, X. Huang and X. Kang, Unraveling the stabilization mechanism of solid electrolyte interface on ZnSe by rGO in sodium ion battery, *J. Energy Chem.*, 2021, **54**, 124–130, DOI: 10.1016/J.JECHEM.2020.05.046.

276 X. Xie, Z. Yin, Y. Li, R. Tu, Y. Liu, H. Tong, X. Ma, Z. Ding and L. Zhou, Zn–O–C bonds for efficient electron/ion bridging in ZnSe/C composites boosting the sodium-ion storage, *J. Mater. Chem. A*, 2022, **10**, 3732–3742, DOI: 10.1039/D1TA10108K.

277 S. Lu, T. Zhu, H. Wu, Y. Wang, J. Li, A. Abdelkader, K. Xi, W. Wang, Y. Li, S. Ding, G. Gao and R. V. Kumar, Construction of ultrafine ZnSe nanoparticles on/in amorphous carbon hollow nanospheres with high-power-density sodium storage, *Nano Energy*, 2019, **59**, 762–772, DOI: 10.1016/J.NANOEN.2019.03.008.

278 F. Huang, L. Wang, D. Qin, Z. Xu, M. Jin, Y. Chen, X. Zeng and Z. Dai, Constructing Heterostructured Bimetallic Selenides on an N-Doped Carbon Nanoframework as Anodes for Ultrastable Na-Ion Batteries, *ACS Appl. Mater. Interfaces*, 2022, **14**, 1222–1232, DOI: 10.1021/ACSAMI.1C21934/ASSET/IMAGES/MEDIUM/AM1C21934_M006.GIF.

279 Y. Wang, D. Cao, K. Zhang, W. Kang, X. Wang, P. Ma, Y. Wan, D. Cao and D. Sun, Cation-exchange construction of ZnSe/Sb 2 Se 3 hollow microspheres coated by nitrogen-doped carbon with enhanced sodium ion storage capability, *Nanoscale*, 2020, **12**, 17915–17924.

280 J. Yuan, W. Liu, X. Zhang, Y. Zhang, W. Yang, W. Lai, X. Li, J. Zhang and X. Li, MOF derived ZnSe–FeSe2/RGO Nanocomposites with enhanced sodium/potassium storage, *J. Power Sources*, 2020, **455**, 227937, DOI: 10.1016/J.JPOWSOUR.2020.227937.

281 C. Dong, L. Wu, Y. He, Y. Zhou, X. Sun, W. Du, X. Sun, L. Xu and F. Jiang, Willow-Leaf-Like ZnSe@N-Doped Carbon Nanoarchitecture as a Stable and High-Performance Anode Material for Sodium-Ion and Potassium-Ion Batteries, *Small*, 2020, **16**, 2004580, DOI: 10.1002/SMLL.202004580.

282 J. Ho Na, Y. Chan Kang and S. K. Park, Electrospun MOF-based ZnSe nanocrystals confined in N-doped mesoporous carbon fibers as anode materials for potassium ion batteries with long-term cycling stability, *Chem. Eng. J.*, 2021, **425**, 131651, DOI: 10.1016/J.CEJ.2021.131651.

283 P. Liu, J. Han, K. Zhu, Z. Dong and L. Jiao, Heterostructure SnSe2/ZnSe@PDA Nanobox for Stable and Highly Efficient Sodium-Ion Storage, *Adv. Energy Mater.*, 2020, **10**, 2000741, DOI: 10.1002/AENM.202000741.

284 J. Chu, W. Wang, Q. Yu, C. Y. Lao, L. Zhang, K. Xi, K. Han, L. Xing, L. Song, M. Wang and Y. Bao, Open ZnSe/C nanocages: multi-hierarchy stress-buffer for boosting cycling stability in potassium-ion batteries, *J. Mater. Chem. A*, 2020, **8**, 779–788, DOI: 10.1039/C9TA10088A.

285 X. Xu, B. Mai, Z. Liu, S. Ji, R. Hu, L. Ouyang, J. Liu and M. Zhu, Self-sacrificial template-directed ZnSe@C as high performance anode for potassium-ion batteries, *Chem. Eng. J.*, 2020, **387**, 124061, DOI: 10.1016/J.CEJ.2020.124061.

286 Y. Hu, T. Lu, Y. Zhang, Y. Sun, J. Liu, D. Wei, Z. Ju and Q. Zhuang, Highly Dispersed ZnSe Nanoparticles Embedded in N-Doped Porous Carbon Matrix as an Anode for Potassium Ion Batteries, *Part. Part. Syst. Charact.*, 2019, **36**, 1900199, DOI: 10.1002/PPSC.201900199.

287 X. Li, Z. Han, W. Yang, Q. Li, H. Li, J. Xu, H. Li, B. Liu, H. Zhao, S. Li, X. Wang and X. L. Wu, 3D Ordered Porous Hybrid of ZnSe/N-doped Carbon with Anomalously High Na+ Mobility and Ultrathin Solid Electrolyte Interphase for Sodium-Ion Batteries, *Adv. Funct. Mater.*, 2021, **31**, 2106194, DOI: 10.1002/ADFM.202106194.

288 X. Xu, T. Yang, F. Li, S. Ji, J. Zhao, Y. Huo and J. Liu, Recent advances in zinc-based chalcogenides for potassium ion batteries, *Resour. Chem. Mater.*, 2024, **3**, 279–293, DOI: 10.1016/J.RECM.2023.08.002.

289 A. Lee, G. D. Park and Y. C. Kang, Double-shell and yolk-shell structured ZnSe-carbon nanospheres as anode materials for high-performance potassium-ion batteries, *Int. J. Energy Res.*, 2022, **46**, 3539–3553, DOI: 10.1002/ER.7404.

290 L. Gao, G. Chen, L. Zhang and X. Yang, Dual carbon regulated yolk-shell ZnSe microsphere anode materials towards high performance potassium ion batteries, *Electrochim. Acta*, 2022, **425**, 140717, DOI: 10.1016/J.ELECTACTA.2022.140717.

291 L. Wang, A. Zhang, N. Li, A. C. Y. Yuen, C. Deng, Q. Dong, L. Zhang, G. H. Yeoh and W. Yang, Lamellar network structure constructed by ZnSe/C nanorods for high-performance potassium storage, *Electrochim. Acta*, 2022, **419**, 140405, DOI: 10.1016/J.ELECTACTA.2022.140405.

292 D. Huang, D. Wu, J. Zhu, J. Xie, J. Wu and J. Liang, One-dimensional ZnSe@N-doped carbon nanofibers with simple electrospinning route for superior Na/K-ion storage, *Chin. Chem. Lett.*, 2023, **34**, 107416, DOI: 10.1016/J.CCLET.2022.04.014.

293 Y. He, L. Wang, C. Dong, C. Li, X. Ding, Y. Qian and L. Xu, In-situ rooting ZnSe/N-doped hollow carbon architectures as high-rate and long-life anode materials for half/full sodium-ion and potassium-ion batteries, *Energy Storage Mater.*, 2019, **23**, 35–45, DOI: 10.1016/J.ENSM.2019.05.039.

294 A. Sirelkhatim, S. Mahmud, A. Seeni, N. H. M. Kaus, L. C. Ann, S. K. M. Bakhori, H. Hasan and D. Mohamad, Review on zinc oxide nanoparticles: Antibacterial activity and toxicity mechanism, *Nano-Micro Lett.*, 2015, **7**, 219–242, DOI: 10.1007/S40820-015-0040-X/TABLES/2.

295 P. Gupta, R. G. Solanki, P. Patel, K. M. Sujata, R. Kumar and A. Pandit, Enhanced Antibacterial and Photoluminescence Activities of ZnSe Nanostructures, *ACS Omega*, 2023, **8**, 13670–13679, DOI: 10.1021/ACSOMEGA.2C07654/ASSET/IMAGES/LARGE/AO2C07654_0013.JPEG.

296 S. S. Shinde, Antimicrobial activity of ZnO nanoparticles against pathogenic bacteria and fungi, *Sci. Med. Cent.*, 2015, **3**, 1033.

297 A. Singh, P. K. Gautam, A. Verma, V. Singh, P. M. Shivapriya, S. Shivalkar, A. K. Sahoo and S. K. Samanta, Green synthesis of metallic nanoparticles as effective alternatives to treat antibiotics resistant bacterial infections: A review, *Biotechnol. Rep.*, 2020, **25**, e00427, DOI: 10.1016/J.BTRE.2020.E00427.

298 I. A. Mir, H. Alam, E. Priyadarshini, R. Meena, K. Rawat, P. Rajamani, M. S. Rizvi and H. B. Bohidar, Antimicrobial and biocompatibility of highly fluorescent ZnSe core and ZnSe@ZnS core-shell quantum dots, *J. Nanoparticle Res.*, 2018, **20**(7), 174, DOI: 10.1007/S11051-018-4281-8.

299 V. G. Reshma, K. S. Rajeev, K. Manoj and P. V. Mohanan, Water dispersible ZnSe/ZnS quantum dots: Assessment of cellular integration, toxicity and bio-distribution, *J. Photochem. Photobiol., B*, 2020, **212**, 112019, DOI: 10.1016/J.JPHOTOBIOL.2020.112019.

300 R. de Oliveira, S. Balabanov and K. Krambrock, Establishment of the conditions to improve the luminescence properties of ZnSe for application as scintillating bolometer in the search for neutrinoless double beta decay, *J. Lumin.*, 2021, **233**, 117930, DOI: 10.1016/J.JLUMIN.2021.117930.

301 Y. Luo, M. Yin, L. Chen, B. Kang and S. Yu, Hot-pressed Fe2+:ZnSe transparent ceramics with different doping concentrations, *Ceram. Int.*, 2022, **48**, 3473–3480, DOI: 10.1016/J.CERAMINT.2021.10.125.

302 C. Emir, A. Tataroglu, U. Gökmen and S. B. Ocak, Analysis of the structural and optical characteristics of ZnSe thin films as interface layer, *J. Mater. Sci. Mater. Electron.*, 2025, **36**, 1–12, DOI: 10.1007/S10854-025-14221-3/FIGURES/9.

303 D. Li, N. Wei, J. Yang, C. Zhao, J. Zhou, J. Li and X. Liu, Effects of hot isostatic pressing on the performance of CVD ZnSe, *Opt. Mater.*, 2022, **132**, 112868, DOI: 10.1016/J.OPTMAT.2022.112868.